

Structure and Activity of Copper/Zinc Oxide Catalysts studied using X-ray Diffraction and Absorption Spectroscopy

vorgelegt von
Diplom-Chemiker
Marco Maria Günter
aus Hildesheim

von der Fakultät II – Mathematik und Naturwissenschaften-
der Technischen Universität Berlin
zur Erlangung des akademischen Grades
Doktor der Naturwissenschaften
- Dr. rer. nat -
genehmigte Dissertation

Promotionsausschuß:

Vorsitzender: Prof. Dr. C. van Wüllen

Berichter: Prof. Dr. M. Lerch

Berichter: Prof. Dr. R. Schlögl

Tag der wissenschaftlichen Aussprache: 13. Juli 2001

Berlin 2001

D 83

ABSTRACT

This thesis reports on bulk structure-activity relationships of Cu/ZnO catalysts for methanol synthesis and methanol steam reforming using X-ray diffraction (XRD) and X-ray absorption spectroscopy (XAS). XRD line profile analysis was applied to series of activated binary Cu/ZnO catalysts with varying molar ratios to determine the microstructure of Cu and ZnO. The procedure affords for both phases a considerable microstructural imperfection due to nanocrystallinity and microstrain as a function of the Cu/Zn ratio. Bulk defects are considered to be the origin of the observed structural disorder of Cu and ZnO which can originate from dissolution of Zn in Cu, incomplete reduction and epitaxial bonding of metal Cu clusters to the ZnO lattice. Additional EXAFS measurements at the Cu K and the Zn K edge show that about 5 % ZnO are dissolved in the CuO matrix of the calcined precursors.

A sample set of binary Cu/ZnO catalysts with varying molar ratios (90/10 through 10/90) is studied under methanol synthesis conditions at 493 K and at atmospheric pressure. A positive correlation of the turn-over frequency for methanol production with the observed microstrain of copper in the Cu/ZnO system is found. In addition, the bulk structure of various binary Cu/ZnO catalysts for methanol steam reforming is studied by *in situ* XRD and XAS under activation and working conditions. The evolution of bulk phases from CuO/ZnO precursors during activation with hydrogen is studied using temperature programmed reduction (TPR). Using time-resolved *in situ* XANES measurements at the Cu K edge during TPR experiments the degree of reduction was monitored. It is shown that Cu₂O forms prior to Cu. The extent of reduction to Cu exhibited a typical nucleation and growth behavior with an enhanced reaction rate for samples with a lower copper content. Reduction of CuO/ZnO in the presence of water vapor resulted in Cu crystallites with a higher selectivity in methanol steam reforming (optimum composition 60-70 mol-% Cu). Adding oxygen (20 vol-%) to the feed gas leads to the formation a mixture of Cu(II) and Cu(I) oxide accompanied by a complete loss of activity. After switching back to steam reforming conditions the activity is regained and the catalyst shows an increased Cu crystallite size (up to 40%). EXAFS measurements at the Cu K and the Zn K edge indicate a structural disorder of the Cu particles in the medium range order and the dissolution of Zn atoms (up to ~ 4 mol-%) in the copper matrix. Upon oxidation/reduction cycles the disorder in the copper particles increases while Zn segregates out of the copper bulk. A structural model is proposed which ascribes the enhanced activity to structurally disordered (strained) copper particles due to an improved interface interaction with ZnO.

KURZZUSAMMENFASSUNG

Diese Arbeit berichtet über Volumenstruktur-Aktivitätsbeziehungen von binären Cu/ZnO Katalysatoren unterschiedlicher Zusammensetzung für die Methanolsynthese und Methanoldampfreformierung die aufgrund von Untersuchungen mittels Röntgenbeugung und Röntgenabsorptionsspektroskopie aufgestellt werden. Eine Röntgenlinienprofilanalyse wurde auf verschiedene Probenserien von aktivierten Cu/ZnO Katalysatoren angewendet, um die Mikrostruktur von Kupfer und Zinkoxid zu bestimmen. Die Analyse ergibt für beide Phasen deutliche mikrostrukturelle Fehler aufgrund der Nanokristallinität und Mikroverzerrungen die eine Funktion des Cu/Zn Verhältnisses sind. Als Ursache für die beobachtete strukturelle Unordnung von Cu und ZnO werden Volumendefekte angenommen, die aufgrund einer Lösung von Zn in der Kupfermatrix, unvollständiger Reduktion und epitaktischer Beziehung der Kupfermetallcluster zum ZnO-Gitter entstehen können. Zusätzliche EXAFS Messungen an der Cu K und der Zn K Kante zeigen, daß ungefähr 5% ZnO in der CuO-Matrix des kalzinierten Präkursor gelöst sind. Eine Probenreihe von Cu/ZnO Katalysatoren mit unterschiedlichen molaren Verhältnis (90/10 bis 10/90) wird unter Methanolsynthesebedingungen bei 493 K und unter Normaldruck untersucht. Eine positive Korrelation der Turnoverfrequenz für die Methanolproduktion mit der beobachteten Mikroverzerrung des Kupfers im Cu/ZnO System kann aufgestellt werden.

Zusätzlich wird die Volumenstruktur von verschiedenen Cu/ZnO Katalysatoren für die Methanoldampfreformierung mittels *in situ* XRD und XAS unter Aktivierungs- und Betriebsbedingungen untersucht. Die Entwicklung der Volumenphasen von CuO/ZnO-Präkursoren während der Aktivierung mit Wasserstoff wird unter temperatur-programmierten Reduktionsbedingungen (TPR) beobachtet. Mit Hilfe einer zeitaufgelösten *in situ* Röntgenabsorptions-Nahkantenstruktur-Spektroskopie (XANES) an der Kupfer K Kante während des TPR Experiments ist es möglich, den Reduktionsgrad zu verfolgen. Es kann gezeigt werden, daß während der Reduktion des CuO sich zwischenzeitlich Kupfer(I)oxid ausbildet. Der Verlauf der Reduktion zum metallischen Kupfer folgt einem typischen Keimbildungs- und wachstumsverlauf, mit einer erhöhten Reaktionsrate für Proben mit einem geringen Kupfergehalt. Die Reduktion von CuO/ZnO in der Gegenwart von Wasserdampf führt zu Kupferkristalliten mit einer höheren Aktivität bei der Methanol-Dampfreformierungsreaktion (optimale Zusammensetzung 60 – 70 mol-% Cu). Die Zugabe von Sauerstoff (20 vol-%) zum Eduktgasstrom resultiert in der Bildung einer Mischung von Kupfer(I)- und Kupfer(II)-oxid, was mit einem vollständigen Verlust der Aktivität einhergeht. Nachdem die Ausgangsbedingungen der Dampfreformierungsreaktion wieder eingestellt sind, wird eine

Zunahme der Aktivität beobachtet; zudem zeigt der Katalysator eine Zunahme der Kupferkristallitgröße (bis zu 40%). EXAFS Messungen an der Kupfer K und der Zn K Kante deuten eine strukturelle Unordnung der Kupferpartikel auf einer mittlereichweitigen ($\sim 6 \text{ \AA}$) Längenskala an und zeigen zudem die Ausbildung von gelöstem Zn in der Kupfermatrix. Nach Oxidations/Reduktionszyklen nimmt die strukturelle Unordnung in den Kupferpartikeln zu, während gelöstes Zn aus dem Volumen der Cu Kristallite segregiert. Ein strukturelles Model wurde entwickelt, daß die erhöhte Aktivität den strukturell ungeordneten (verzernten) Kupferpartikeln zuschreibt, was aus einer verbesserten Wechselwirkung des Kupfers an der Grenzfläche zum ZnO resultiert.

ZUSAMMENFASSUNG

Günter, Marco Maria:

Studies on the Structure and Activity of Copper/Zinc Oxide catalysts using X-ray Diffraction and Absorption Spectroscopy.

In der vorliegenden Arbeit wurden Untersuchungen zur Struktur und Reaktivität von reduzierten Kupfer/Zinkoxid-Katalysatoren in der Methanolsynthese und der Methanoldampfreformierung durchgeführt. Dabei wurden Röntgenbeugung und Röntgenabsorptionsspektroskopie zur Strukturbestimmung sowohl unter *ex situ* als auch unter *in situ* Bedingungen verwendet, um die Mikrostruktur der katalytisch aktiven Kupferphase für die unterschiedlichen Reaktionen zu bestimmen. Die beiden experimentellen Techniken sind insofern komplementär zueinander, als daß sowohl die kurzreichweitige als auch die langreichweitige Ordnung der Volumenstruktur des Katalysatorsystems untersucht werden kann. Einen thematischen Schwerpunkt der Arbeit stellt die Frage dar, inwieweit die Defektstruktur des Festkörpers für die Aktivität von heterogen-katalysierten Reaktionen von Bedeutung ist. Die vorgestellten Messungen werden für zwei bei unterschiedlichem *pH*-Wert präparierte Probenserien mit variierendem Cu/Zn Verhältnis durchgeführt, um den Einfluß der naß-chemischen Präparationsbedingungen der Hydroxykarbonatpräkusoren und der Zusammensetzung auf die katalytisch aktive Phase zurückzuverfolgen.

Die Arbeit gliedert sich in sechs Hauptkapitel, wobei das Einleitungskapitel (Kapitel 1) auf die Aufgabenstellung hinweist und den bisherigen Erkenntnisstand der Literatur darlegt. Die verwendeten experimentellen Methode und deren Anwendungspotential für die Untersuchung der Volumenstruktur von Katalysatoren werden in Kapitel 2 dargestellt. Die experimentellen Ergebnisse werden in den Kapiteln 3-5 vorgestellt und diskutiert. Eine Zusammenfassung und ein Ausblick wird in Kapitel 6 gegeben. Im folgenden werden die wesentlichen experimentellen Ergebnisse wiedergegeben und zusammengefaßt:

In Kapitel 3 wird die Methode der Linienprofilanalyse von Röntgenreflexen von nanokristallinen Cu/ZnO-Kristallen mit unterschiedlichen Cu/Zn-Verhältnis angewendet, um die Mikrostruktur von Cu und ZnO zu bestimmen. Die aktivierten Katalysatoren wurden durch Reduktion von CuO/ZnO Präkusoren mit Wasserstoff bei 523 K und 673 K erhalten, die unter verschiedenen Fällungsbedingungen (konstanter *pH* (*pH* = 7) und abfallender *pH*-Wert) präpariert wurden. Die Anwendung der Röntgenprofilanalyse auf Basis der integralen Breite der

Reflexe beruht auf einer analytischen Beschreibung der Linienprofile mit Hilfe der Voigtfunktion und erlaubt eine detaillierte Mikrostrukturanalyse in Bezug auf Kristallitgrößen- und Verzerrungseffekte. Die Bestimmung der Kristallitgröße und der Gitterverzerrung nach der sogenannten Einzel-Linienmethode-Methode wird vorgestellt und angewendet auf ausgewählte Beugungsreflexe von Cu und ZnO. Für beide Phasen wird eine strukturelle Unordnung aufgrund von Kristallitgrößeneffekte und Mikroverzerrungen nachgewiesen, welche eine Funktion des Cu/Zn-Verhältnisses sind. Die Ergebnisse deuten auf eine gegenseitige strukturelle Wechselwirkung der beiden Komponenten (Kupfer und Zinkoxid) hin, in der Form, daß verzerrte Kupferpartikel stabilisiert werden durch unverzerrte Zinkoxid Mikrokristallite. Die beobachtete strukturelle Unordnung von ZnO für Proben mit hohem Kupfergehalt kann seinen Ursprung haben in: (a) einer epitaktischen Bindung des ZnO-gitters zum Kupfermetall, (b) einer unvollständigen Reduktion oder (c) in einem Carbonatrestgehalt aufgrund unvollständiger thermischen Zersetzung des Hydroxycarbonatpräkursors. Zusätzliche EXAFS Messungen an der Cu K und Zn K Kante zeigen, daß ungefähr 5% ZnO in der CuO-Matrix des kalzinierten Präkursors gelöst sind. Weiterhin wurde gezeigt, daß die mikrostrukturellen Veränderungen (z.B. Kristallitgrößen und Gitterverzerrungen) des Kupfers auf die Phasenzusammensetzung des dazugehörigen Hydroxykarbonatpräkursors zurückgeführt werden können.

In Kapitel 4 werden binäre Cu/ZnO Katalysatoren mit unterschiedlichen molaren Cu/Zn Verhältnissen (Proben präpariert bei konstantem pH- Wert und im Cu/Zn-Verhältnis von 90/10 bis 10/90) unter Methanolsynthesebedingungen bei 493 K unter Atmosphärendruck untersucht. Die Methanolsyntheseaktivität der Katalysatoren wird korreliert mit ihrer spezifischen Cu-Oberfläche (N₂O Frontalchromatographie, N₂O RFC) nach Reduktion in 2 vol-% H₂ bei 513 K. Die Aktivitätsdaten werden erweitert mit den Ergebnissen der detaillierten Analyse der Kupfermikrostruktur mittels Röntgenbeugungs-Linienprofilanalyse aus Kapitel 3. Die unter Annahme einer Kugelform der Kupferkristallite abgeschätzte Cu-Oberfläche ist in guter Übereinstimmung mit den mittels N₂O RFC bestimmten Daten. Eine positive Korrelation der *Turnover*-Frequenz für die Methanolproduktion mit der beobachteten Mikroverzerrung des Kupfers in Cu/ZnO kann aufgestellt werden.

In Kapitel 5 wird die Volumenstruktur des Kupfers für unterschiedlich zusammengesetzte Cu/ZnO Katalysatoren für die Methanoldampfreformierungsreaktion unter Aktivierungs- und Betriebsbedingungen mittels *in situ* Röntgenbeugung (XRD) und Röntgenabsorptions-Spektroskopie (XAS) untersucht. Unter temperatur-programmierten Bedingungen im Temperaturbereich von 448 – 523 K wird die zeitliche Entwicklung der Volumenkupferphase

ausgehend von CuO/ZnO Präkursoren während der Aktivierung mit Wasserstoff untersucht. Somit konnte sowohl der Beginn der Reduktion als auch die Kristallitgröße des sich bildenden metallischen Kupfers beobachtet werden. Die Reduktionen werden unter zwei verschiedenen Atmosphären sowohl mit als auch ohne Wasserdampf durchgeführt. Es zeigt sich, daß mit abnehmendem Kupfergehalt das Einsetzen der Reduktion sich von 473 K (reines CuO) nach 443 K (40 mol-% Cu) verschiebt. Diese Beobachtung geht einher mit einer Abnahme der Kupferkristallitgröße (von 210 Å bis 40 Å). Auf der Basis von zeitaufgelösten Röntgenabsorptions-Nahkantenstruktur- (XANES)-Messungen an der Kupfer K Kante während des TPR Experiments ist es möglich, den Reduktionsgrad zu verfolgen. Es konnte gezeigt werden, daß während der Reduktion des CuO sich zwischenzeitlich Kupfer(I)oxid ausbildet. Der Verlauf der Reduktion zum metallischen Kupfer folgt einem typischen Keimbildungs- und wachstumsverlauf, mit einer erhöhten Reaktionsrate für Proben mit einem geringen Kupfergehalt. Die Reduktion von CuO/ZnO in der Gegenwart von Wasserdampf führt zu Kupferkristalliten mit einer höheren Aktivität bei der Methanol-Dampfreformierungsreaktion (optimale Zusammensetzung 60 – 70 mol-% Cu). Die Zugabe von Sauerstoff (20 vol-%) zum Eduktgasstrom resultiert in der Bildung einer Mischung von Kupfer(I)- und Kupfer(II)-oxid Phasen, was mit einem vollständigen Verlust der Aktivität einhergeht. Nachdem die Ausgangsbedingungen der Dampfreformierungsreaktion wieder eingestellt sind, wird eine Zunahme der Aktivität beobachtet; zudem zeigt der Katalysator eine Zunahme der Kupferkristallitgröße (bis zu 40%). EXAFS Messungen an der Kupfer K und der Zn K Kante deuten eine strukturelle Unordnung der Kupferpartikel auf einer mittlereichweitigen (~ 6 Å) Längenskala an und zeigen zudem die Ausbildung von gelöstem Zn in der Kupfermatrix. Nach Oxidations/Reduktionszyklen nimmt die strukturelle Unordnung in den Kupferpartikeln zu, während gelöstes Zn aus dem Volumen der Cu Kristallite segregiert. Ein strukturelles Model wurde entwickelt, daß die erhöhte Aktivität den strukturell ungeordneten (verzerrten) Kupferpartikeln zuschreibt, was aus einer verbesserten Wechselwirkung des Kupfers an der Grenzfläche zum ZnO resultiert.

Zusammenfassend zeigt ein Vergleich der aufgestellten Struktur-Aktivitätsbeziehungen für die Methanolsynthese und die Methanoldampfreformierung, daß für beide katalytischen Prozesse eine strukturelle Unordnung und Verzerrung des Kupfers in einem realen Cu/ZnO Katalysator nachgewiesen werden konnte, die mit einer erhöhten spezifischen Aktivität korreliert werden kann. Die beobachteten Aktivitätssteigerungen für verzerrte und defektreiche Kupfercluster können daher eine Folge der daraus resultierenden Veränderungen der Oberflächeneigenschaften aufgrund einer Struktursensitivität der Reaktion sein. Die Untersuchungen belegen, daß dabei Festkörperumwandlungen und die Wechselwirkung der

Kupfer und der Zinkoxidphase für die Entstehung der Defekte zu berücksichtigen sind. Somit konnte erstmalig für das Kupfer/Zinkoxid Katalysatorsystem ein experimenteller Beleg erbracht werden, daß auch Volumeneigenschaften neben der Kupferoberfläche die Reaktivität eines Heterogenkatalysators beeinflussen können. Weiterhin eröffnet sich aufgrund der experimentellen Befunde zur Abhängigkeit der Aktivität von den Herstellungsbedingungen des Katalysators die Möglichkeit durch geeignete Wahl der Präparationsbedingungen des Katalysators die Volumenstruktur des Katalysator derart zu verändern, daß ein aktivere Kupferoberfläche resultiert.

Acknowledgment/Danksagung

Die vorliegende Dissertation wurde in der Zeit von April 1997 bis Dezember 2000 in der Abteilung Anorganische Chemie des Fritz-Haber-Instituts der Max-Planck-Gesellschaft in Berlin angefertigt.

Ich möchte Herrn Prof. Schlögl herzlich für die interessante Themenstellung und die Möglichkeit danken, ein Thema der Festkörperchemie am FHI zu bearbeiten. Weiterhin danke ich Prof. Lerch für die Übernahme des Korreferats.

Herrn Dr. Thorsten Ressler gilt mein besonderer Dank, der durch sein stetes Interesse, die hervorragende Unterstützung und die Förderung in fachlicher („WinXAS rules“) und menschlicher Hinsicht diese Arbeit überhaupt erst ermöglichte. Zudem hat er mich als Mentor in die Geheimnisse der Röntgenabsorptionsspektroskopie eingeführt. Auch für die gemeinsamen Stunden beim „*heißen Draht*“ sei an dieser Stelle gedankt.

Dr. Rolf E. Jentoft danke ich für seinen unermüdlichen Einsatz als ‚mother tongue‘ für das linguistische und semantische Erscheinungsbild dieser Arbeit. Bettina Bems danke ich für die unzähligen Probenpräparationen. Vielen (ehemaligen) Doktoranden des FHI sei für die gemeinsamen Fluchten in die Parallelwelt gedankt: Dr. Martin Dieterle, Dr. Prakash Dube, Dr. Armin Fischer, Emilio Sanchez-Cortezon, Mario Melzer, Christian Sachs, Dr. Richard Schumacher, Dr. Heiko Selber, Dr. Stephan Völkening und Dr. Ralph Wichtendahl.

Weiterhin möchte ich mich bei Prof. M. Muhler für die Überlassung der katalytischen Daten zur Methanolsynthese danken. Darüber hinaus gilt mein Dank allen Mitarbeitern des HASYLABS (Hamburg), der Werkstätten, des Rechenzentrums und von PP&B.

Meinen Eltern und meinen Brüdern Simon und Tobias bin ich für die geistige und moralische Unterstützung sehr dankbar. Ines danke ich für ihre langwährende Geduld und das, obwohl sie mir schon von der Wahl des Chemie-LKs abgeraten hatte.

“The path of the righteous man is beset on all sides with the iniquities of the selfish and the tyranny of evil men. Blessed is he who in the name of charity and good will shepherd the weak through the valley of darkness, for he is truly his brother's keeper and the finder of lost children. And I will strike down upon those with great vengeance and with furious anger those who attempt to poison and destroy my brothers. And you will know that my name is the Lord when I lay my vengeance upon thee.”

(according to Ezekiel 25:17 in "Pulp Fiction" directed by Q. Tarantino)

Table of Contents

ACKNOWLEDGMENT/DANKSAGUNG	9
TABLE OF CONTENTS	11
INDEX OF FIGURES	14
INDEX OF TABLES	18
1 INTRODUCTION	19
1.1 Motivation and Strategy	19
1.2 Cu/ZnO catalysts in methanol synthesis and methanol steam reforming	20
1.3 Outline of work.....	24
2 THEORETICAL AND EXPERIMENTAL DETAILS	27
2.1 Introduction	27
2.2 X-ray Diffraction and Line Profile Analysis	27
2.2.1 X-ray diffraction line broadening of small and ‘real’ particles.....	27
2.2.2 XRD measurements in catalysis	30
2.2.3 XRD peak profile refinement procedure using the Voigt function	32
2.2.4 <i>Ex-situ</i> XRD measurements and line profile analysis.....	35
2.2.5 <i>In situ</i> XRD set-up and instrumentation	36
2.3 X-ray absorption spectroscopy (EXAFS and XANES)	37
2.3.1 Theory of EXAFS and XANES.....	37
2.3.2 XAS experiments and instrumentation	41
2.3.3 <i>In situ</i> XANES and EXAFS Data Analysis	43
2.4 Preparation and characterization of CuO/ZnO precursor.....	44
2.5 Catalyst screening for methanol synthesis activity.....	45
2.6 <i>In situ</i> catalytic tests for methanol steam reforming activity	48
2.6.1 TPR measurements of catalyst precursor.....	48
2.6.2 Methanol steam reforming activity screening.....	48

2.7 Transmission electron microscopy (TEM) characterization	49
2.7.1 Application of TEM on catalysts	49
2.7.2 Experimental details	50
 3 EX SITU STUDIES ON COPPER OXIDE /ZINC OXIDE	51
 3.1 Copper Oxide/Zinc Oxide Precursor	51
3.1.1 Introduction.....	51
3.1.2 XRD characterization of CuO/ZnO	52
3.1.3 EXAFS measurement of CuO/ZnO	55
3.1.4 Transmission electron microscopy of CuO/ZnO	58
3.1.5 Discussion.....	59
 3.2 Microstructural characteristics of reduced Cu/ZnO catalysts	61
3.2.1 Introduction.....	61
3.2.2 X-ray diffraction Data.....	61
3.2.3 Microstructural characterization of Cu	63
3.2.4 Microstructural characterization of ZnO.....	66
3.2.5 Transmission electron microscopy of Cu/ZnO	72
3.2.6 Discussion.....	75
 3.3 Conclusion.....	78
 4 IMPLICATION OF CU MIRCOSTRUCTURE FOR METHANOL SYNTHESIS ACTIVITY	81
 4.1 Introduction	81
 4.2 Microstructural characteristics revealed by X-ray diffraction line profile analysis	81
4.2.1 Copper surface area measurements.....	83
4.2.2 Catalytic activity screening.....	85
4.2.3 Impact of Cu microstrain on Turn-over-frequency	87
 4.3 Summary.....	90
 5 IN SITU STUDIES ON CU/ZNO USING X-RAY DIFFRACTION AND ABSORPTION.....	91
 5.1 Introduction	91
 5.2 In situ XRD	91
5.2.1 Reduction of the CuO/ZnO precursor.....	91
5.2.2 Steam Reforming of Methanol.....	96

5.2.3 Oxygen addition cycle	104
5.3 In situ XAFS	107
5.3.1 Reduction of CuO/ZnO precursor.....	107
5.3.2 Redox cycles during steam reforming of methanol	113
5.4 Discussion.....	122
5.4.1 In situ XRD.....	122
5.4.2 In situ XAFS.....	126
5.4.3 Mechanistic considerations.....	127
5.4.4 Implication of microstructural changes of Cu and ZnO on the catalytic activity.....	129
5.4.5 Model of microstructural changes of Cu and ZnO.....	131
5.5 Conclusion.....	132
6 SUMMARY AND PERSPECTIVES.....	135
7 LITERATURE.....	141
8 APPENDIX	149
8.1 List of abbreviation and symbols	149
8.2 Publication Index.....	151
8.3 Curriculum Vitae	152

Index of Figures

Figure 2.1: Bragg' law for the case of a rectangular grid, i.e. $AB = BC = d_{hkl} \sin \theta$	28
Figure 2.2: Schematic representation of the influence of no strain (a), uniform (b) and non-uniform (c) microstrain on the XRD profile (taken from [Jenkins96]).....	29
Figure 2.3: Schematic representation of strain caused by dislocation in a crystal (taken from [Gillmann62]).	30
Figure 2.4: Intrinsic and instrumental line profiles after deconvolution of an experimental XRD peak normalized to a zero position using the Stokes deconvolution method.	32
Figure 2.5: Schematic setup of the in situ XRD-cell in Bragg Brentano geometry.	37
Figure 2.6: X-ray absorption spectra of Cu K edge of a Cu/ZnO catalyst with 70 mol-% Cu.	38
Figure 2.7: Schematic illustration of constructive (in phase, (a)) and destructive (out of phase, (b)) interference between out going and backscattered photoelectron wave from neighboring atoms.....	39
Figure 2.8: Schematic representation of experimental set-up for a transmission XAS experiment.....	42
Figure 2.9: Schematic setup of the in situ XAS-cell operated in transmission geometry.	42
Figure 3.1: XRD patterns of a systematic series of calcined CuO/ZnO samples prepared at constant pH (a) and decreasing pH (b). Characteristic (hkl) lines for CuO (002), (111) and ZnO (100) and (101) are indicated.....	53
Figure 3.2: Crystallite size of CuO and ZnO after calcination at 600 K based on the (111) or (100) reflection for CuO and ZnO respectively together with the corresponding BET data. (a) constant pH preparation, (b) decreasing pH preparation.	54
Figure 3.3: Fourier transformed experimental Cu K edge $\chi(k)$ of systematic series of calcined samples prepared at constant pH (a) and at decreasing pH (b) and corresponding Fourier transformed experimental Zn K edge $\chi(k)$ of the constant (a) and decreasing (b) pH sample set. Dashed lines represent spectra that deviate from a linear trend in structure with composition.	56
Figure 3.4: Experimental Fourier transformed Zn K edge $\chi(k)$ (magnitude and imaginary part) of ZnO, and calcined samples with Cu/Zn of 90/10 and 80/20 (a), and experimental FT($\chi(k)$) of Cu K edge of CuO and calcined samples with Cu/Zn of 90/10 and 80/20 (b).	57
Figure 3.5: Transmission electron micrograph of calcined samples C60/40 (a), C70/30 (b), D60/40 (c), and D60/40. The magnified inset of a catalyst particle of sample C60/40 shows lattice fringes.	58
Figure 3.6: XRD patterns of systematic series of reduced Cu/ZnO catalysts. Samples have been prepared according to the (a) constant pH, and (b) decreasing pH preparation method after reduction with hydrogen at 523 K, and (c) decreasing pH preparation after reduction with hydrogen at 673 K, reflections due to an internal standard Si are marked. Characteristic (hkl) lines for Cu (111) and ZnO (002), (100), (101) and (110) are indicated.....	63
Figure 3.7: Experimental data and refined profile of a Cu (111) reflection using a Voigt function. The difference pot, measured minus refined profile, is shown in the lower part of the graph (sample with 60 mol-%, decreasing pH reduced at 523 K).	63
Figure 3.8: Copper crystallite size (a) and microstrain (b) determined according to the Voigt deconvolution procedure as a function of the nominal Zn-content of samples reduced in 5 vol-% H ₂ at 523 K (decreasing and constant pH) and 673 K (decreasing pH). The data is based on the analysis of the copper (111) peak.....	65
Figure 3.9: Experimental data and refined profile of ZnO (100), (002), (110) and (110) ((a) –(c)) reflection using the Voigt function. The difference plot, measured minus refined profile, is shown in the lower part of the graph (sample with 60 mol-%, decreasing pH reduced at 523 K).	67

Figure 3.10: Zinc oxide crystallite size (a) and microstrain (b) determined according to the Voigt deconvolution procedure as a function of the nominal Zn-content for samples reduced in 5 vol-% H ₂ at 523 K (decreasing and constant pH) and 673 K (decreasing pH). The data is based on the analysis of the zinc oxide (100) peak.	69
Figure 3.11: ZnO crystallite sizes (a) and microstrain (b) after reduction at 523 K as a function of the Zn-content (constant pH). The values are determined for different crystallographic directions based on the (100), (002) and (110) reflection.	70
Figure 3.12: ZnO crystallite sizes (a) and microstrain (b) after reduction at 673 K as a function of the Zn-content (decreasing pH). The values are determined for different crystallographic directions based on the (100), (002) and (110) reflection.	72
Figure 3.13: Transmission electron micrograph and convergent beam electron diffraction (inset) of a commercial catalyst reduced at 523 K.	72
Figure 3.14: Selected area electron diffraction pattern from a reduced catalyst reduced in 5 vol-% H ₂ at 523 K (a); corresponding bright field image and dark field of image of the ZnO phase using the (100) and (010) diffraction spot ((b) 1,2); dark field image of the Cu phase using the Cu (111) reflection ((b) 3).	74
Figure 3.15: Schematic representation of crystallographic orientation at the Cu/ZnO interface of a reduced catalyst showing.	75
Figure 4.1: Variation of crystallite size and microstrain of copper (a) and zinc oxide (b) as a function of the nominal composition after reduction at 523 K in 5 vol-% H ₂ in He. The data are based on the analysis of the copper (111) peak and the ZnO (100) peak. Composition of interest for industrial application is shown in the shaded area. ...	82
Figure 4.2: Variation of the Cu lattice parameter a with Zn content after reduction in 2 vol.-% hydrogen at 523 K (measured at RT). Composition of interest for industrial application is shown in shaded area.	83
Figure 4.3: Copper surface area as a function of the nominal composition. Values are determined either by N ₂ O RFC (S _{Cu(N₂O)}) or estimated using the crystallite size determined by XRD (S _{Cu(XRD)}). Composition of interest for industrial application is shown in the shaded area.	84
Figure 4.4: Ratio of copper surface atoms determined by N ₂ O RFC to bulk atoms from XRD crystallite size assuming a spherical shape as a function of the Zn content. Composition of interest for industrial application is shown in the shaded area.	84
Figure 4.5: Normalized production rate of methanol with increasing Zn concentration. The reaction was carried out at 493 K under atmospheric pressure with a feed gas composition of 10% CO, 4% CO ₂ , 72% H ₂ in He.	85
Figure 4.6: Normalized methanol production rate as a function of copper metal surface area. Composition of interest for industrial application is shown in the shaded area.	86
Figure 4.7: Normalized turn-over frequency (TOF) for methanol production as a function of Zn content. Composition of interest for industrial application is shown in the shaded area.	86
Figure 4.8: Normalized turn-over frequency (TOF) for methanol production as a function of the Cu microstrain derived for the Cu (111) peak.	87
Figure 4.9: Normalized turn-over frequency (TOF) for methanol production as a function of (a) the copper atom dispersion (expressed as the ratio of Cu surface atoms determined by N ₂ O RFC to the number of the bulk atoms based on XRD crystallite size determination), (b) the copper lattice parameter a.	89
Figure 5.1: (a) Evolution of the Cu (111) peak during reduction of a CuO/ZnO sample (D70/30) in 2 vol-% hydrogen measured by in situ XRD. Measuring time 7 min/scan and an effective heating ramp of 0.5 K/min. (b) Corresponding normalized mass spectrometer signals of H ₂ O and H ₂ during TPR and evolution of integrated intensity of the Cu (111) peak.	94

Figure 5.2: Evolution of Cu crystallite size during TPR for samples with different Cu/Zn ratio measured both in 3 vol-% H ₂ ('dry') and 2.5 vol-% H ₂ + 3 vol-% H ₂ O ('wet') in 100 ml/min for both sets of sample preparations: (a) constant pH preparation, (b) decreasing pH preparation. The temperature was raised with an effective heating ramp of 0.5 K/min.....	95
Figure 5.3: (a) Time on stream behavior for sample D60/40 ('dry' reduced) measured in XRD in situ cell. (b) deactivation behavior of a pure Cu sample (D100/0, 'wet' reduced). Experimental conditions: MeOH/H ₂ O ~ 4/1 in 120 ml/min He and temperature ramp from 433 K to 523 K at 0.5 K/min.....	98
Figure 5.4: Selectivity to CO ₂ as a function of the conversion of MeOH at 523 K with a flow of MeOH/H ₂ O (ratio of ≈ 4/1) in 120 ml/min He; samples were obtained by 'dry' and 'wet' reduction, (a) samples prepared by the constant pH method, (b) samples prepared by the decreasing pH method.	99
Figure 5.5: Initial hydrogen production rate as a function of the Cu metal surface area for catalysts prepared at constant pH method and at decreasing pH method. Both sample series were activated under 'wet' and 'dry' reduction conditions. The Cu surface area is estimated by XRD. Reaction conditions where the same as in Figure 5.3.....	100
Figure 5.6: Initial turn-over-frequency (TOF) for hydrogen production as a function of ZnO-content for catalysts prepared according to the decreasing and the constant pH method (both under 'dry' and 'wet' reduction conditions). Reaction conditions where the same as in Figure 5.3.	101
Figure 5.7: Evolution of Cu crystallite size under steam reforming conditions at 523 K for different catalyst with compositions and different reduction pretreatment as indicated over course of 7 h: (a) constant pH preparation, (b) decreasing pH preparation. Reaction conditions: same as in Figure 5.3.	102
Figure 5.8: Evolution of copper crystallite size during time on stream at 523 K together with the effluent concentration of H ₂ in the in situ XRD cell; (a) sample D 100/0 ('wet' reduced), (b) sample D 60/40 ('dry' reduced). Dashed line is guide to the eye.	103
Figure 5.9: X-ray diffraction patterns of a sample with a composition of 60 at-% Cu and 40 at-% Zn (C60/40) during different stages of treatment. Upon reduction the calcined CuO (a) is transformed into Cu metal which is preserved under methanol steam reforming conditions at 523 K (b). Oxygen treatment resulted in a mixture of Cu(I) oxide and Cu(II) oxide (c). The oxidic copper phases are re-reduced in the feed to metallic Cu with a decreased line width (d). Characteristic (hkl) diffraction lines of CuO, Cu ₂ O, and Cu metal are indicated.....	104
Figure 5.10: Evolution of gas phase concentration of H ₂ , MeOH, CO ₂ , and H ₂ O in XRD cell under methanol steam reforming conditions during addition of oxygen (15 vol-% O ₂) to the feed for two intervals of ~ 100 min. Sample C60/40 'dry' was used.	105
Figure 5.11: Relative change of ZnO lattice parameters a and c (a) and Cu lattice parameter a (b) with respect to the values of the fresh reduced samples C70/30, C60/40, and C40/60 under methanol steam reforming, and after two successive oxygen addition cycles.....	106
Figure 5.12: a) Evolution of Cu K edge XANES spectra of a CuO/ZnO sample (C70/30) during TPR in 8 vol-% H ₂ with 5 s/frame and a heating rate of 5 K/min. (b) Change in phase composition together with the MS signal of H ₂ O (dotted) and H (solid) during TPR. The quantitative phase analysis is based on a least squares fit using suitable reference spectra of Cu, Cu(I) oxide, and CuO as described in the text.	108
Figure 5.13: Linear combination XANES fit to a CuO _{1-x} spectrum during reduction using Cu, Cu(I) oxide, and CuO reference XANES spectra.....	109
Figure 5.14: Evolution of extent of reduction, α, of CuO/ZnO precursor for (a) three decreasing pH samples (D70/30, D60/40, D40/60) measured by in situ XAFS (8 vol-% H ₂) at 5 K/min from 433 K to 523 K; (b) three	

constant pH samples (C70/30, C60/40, C40/60) reduced with (2 vol-% H ₂) at 5 K/min from 433 K to 523 K. The extent of reduction α was taken as the amount of Cu phase as determined by the linear combination XANES fits. The zero time is defined as the onset of reduction.....	110
Figure 5.15: Fourier transformed Cu K edge $\chi(k)$ of (a) the oxidized (calcined and re-oxidized (Re-Ox.)) and reduced state (Reduced, Re-Red.) at 523 K together with $\chi(k)$ of CuO, Cu ₂ O (both at room temperature). (b) Zn K edge FT[$\chi(k)$] of the oxidized and reduced state of the same catalyst sample together with $\chi(k)$ of pure ZnO. Repeated reduction (2 vol-% H ₂) and oxidation (15 vol-% O ₂) cycles at 523 K of a sample C60/40.	112
Figure 5.16: Evolution of Cu K-edge XANES of CuO/ZnO at 523 K during oxygen addition to a methanol steam reforming feed (c(MeOH) ~ 6 vol-%, c(H ₂ O) ~ 1.5 vol-% in 25 ml/min He). Different Cu phases are indicated.	113
Figure 5.17: (a) Evolution of gas phase composition (H ₂ , MeOH, CO ₂ , and H ₂ O) during oxygen addition to a methanol steam reforming feed in the in situ XAFS cell. Concentration of CO and HCOOCH ₃ is shown in the bottom part of the graph. (b) Changes in selectivity, conversion, and production rate during oxidation and re-reduction (sample C60/40).	114
Figure 5.18: Evolution of Cu phase composition during oxygen addition cycles into steam reforming feed at 523 K. Phase analysis was obtained from least-squares fit of reference spectra to the corresponding XANES spectra shown in Figure 5.16. The two lower sections of the graph depict the evolution of the gas phase in percent and ppm, respectively. Three transitions in bulk and gas phase composition are marked: I.) copper metal during steam reforming, II.) oxidation to CuO _{1-x} , III.) re-reduction of CuO _{1-x} phases.	115
Figure 5.19: Refinement of a sum of theoretical EXAFS function (dashed line) of Cu to an experimental FT($\chi(k)$) of sample C70/30 at 523 K after reduction in 2 vol-% H ₂ . Only the four strongest single scattering EXAFS functions are indicated (thin dark lines). Fitted parameters are found in Table 5.5.....	116
Figure 5.20: Cu Debye-Waller (DW) Factors, σ^2 , for the first, second, third, and fifth Cu-Cu distance obtained from a refinement of a theoretical EXAFS function to experimental data for reduced samples C70/30, C60/40, C40/60, C30/70 and Cu foil obtained at 303 K and 523 K under methanol steam reforming conditions.	117
Figure 5.21: Fourier transformed experimental Cu K edge $\chi(k)$ of sample C70/30 under working conditions for methanol steam reforming at 523 K (feed composition: c(MeOH) ~ 6 vol-%, c(H ₂ O) ~ 1.5 vol-% in 25 ml/min He) after initial reduction (fresh reduced) and after two subsequent oxidation and reduction (denoted as first and second oxidation step).	118
Figure 5.22: Cu Debye-Waller (DW) Factors, σ^2 , for the first, second, third, and fifth Cu-Cu distance obtained from a refinement of a theoretical EXAFS function to experimental data for sample C70/30 (a) and C60/40 (b) obtained at 523 K during methanol steam reforming conditions after different pretreatment (fresh reduced) and after two subsequent oxidation and reduction steps (denoted as 1 st O ₂ , SR and 2 nd O ₂ , SR step).	119
Figure 5.23: Experimental Fourier transformed Zn K edge $\chi(k)$ (magnitude and imaginary part) of ZnO for sample C70/30 obtained at 523 K during methanol steam reforming reaction after different pretreatment (fresh reduced) and after two subsequent oxidation and reduction steps (denoted as 1 st O ₂ , SR and 2 nd O ₂ , SR step).	120
Figure 5.24: Refinement of a theoretical EXAFS function (dotted line) of ZnO to an experimental FT($\chi(k)$) for the sample C70/30 after reduction in 2 vol-% H ₂ at 523 K (a) pure ZnO and (b) assuming additional Zn-Cu shells by doping Zn into the Cu cluster.	121
Figure 5.25: Proposed schematic model for copper particles on a ZnO support after initial reduction (a) and after repeated oxygen addition cycles under methanol steam reforming conditions (b).	131

Index of Tables

Tab. 2.1: Chemical composition and characterization of calcined CuO/ZnO precursors. Calcination conditions: 695 K for 3 h in stagnant air.	47
Table 3.1: Integral breadth parameters and microstructural properties of Cu based on XRD line profile analysis for various samples prepared at constant pH after treatment with H ₂ at 523 K.	64
Table 3.2: Integral breadth parameters and microstructural properties of ZnO based on XRD line profile analysis for various (hkl) reflections prepared at constant pH after treatment with H ₂ at 523 K.	68
Table 5.1: Onset of reduction during TPR and the corresponding copper crystallite sizes after reduction measured by in situ XRD. The reduction was performed under ‘dry’ and ‘wet’ reducing conditions.	92
Table 5.2: Initial methanol steam reforming catalytic activity data (conversion of methanol, selectivity to CO ₂ , hydrogen production rate) for differently reduced Cu/ZnO catalysts at 523 K.	97
Table 5.3: Change of catalytic activity data (conversion of methanol, selectivity to CO ₂ , hydrogen production rate) obtained in XRD and XAS cells after repeated oxidation and reduction steps. All samples were prepared according to the constant pH method and reduced at ‘dry’ conditions. The data was obtained at 523 K with a flow of MeOH/H ₂ O (ratio ~ 4/1) in 120 ml/min (XRD cell) or 25 ml/min (XAS cell). Conversion and selectivity are given as initial values.	107
Table 5.5: Fitting parameters obtained from least-squares refinements using the Avrami-Erofeev equation, $\alpha = 1 - \exp(-kt)^n$, with α representing the extent of reduction (ranging from 1 to 0), k the rate constant, t the reduction time, and n the exponential factor for the evolution of the Cu metal phase measured during temperature programmed reduction in the XAS cell (‘dry’ reduction conditions: 2 vol-% H ₂ for C-series samples and 8 vol-% H ₂ for D-series samples, heat ramp from 433 K to 523 K at 5 K/min) experiments for samples C70/30, C60/40, C40/60, D70/30, D60/40 and D40/60.	111
Table 5.6: Structural parameters of Cu/ZnO (C70/30) at 523 K under methanol steam reforming conditions (Figure 5.28) obtained from a refinement of theoretical EXAFS functions calculated for Cu metal cluster ($k = 2.0$ to 13.0 \AA^{-1} , $R = 1.5$ to 6.0 \AA , $N_{\text{ind}} = 32$, $N_{\text{free}} = 12$, 5 single scattering paths and 14 multiple scattering paths). Parameters refined are $E_0(\text{Cu}) = 3.83 \text{ eV}$. The fit residual amounted to 2.8. Based on shells # 1, 2, 3, 5 an average lattice constant of $a_0 = 3.6410 \text{ \AA}$ (Cu, Fm3m) was obtained.	117

1 Introduction

1.1 Motivation and Strategy

Current research in heterogeneous catalysis is devoted to establish structure-activity relationships of real catalysts. Those insights are required in order to arrive at a rational approach in catalysis which eventually enables a rational catalyst design for more efficient processes. *In situ* methods are regarded as indispensable tools to establish correlations of the structure of a catalyst in a working state and the changes in activity/selectivity. The aim of performing *in situ* experiments on well-known catalyst systems under practical operating conditions is to rationalize working principles of a catalyst [Schlögl93].

Today's understanding in catalysis research has greatly benefited from studies in surface science [Somorjai94]. However, the wealth of working concepts obtained by surface science investigation could not be directly transferred to real catalysts systems owing to the inherent complexity that is referred to as the 'pressure gap' and 'materials gap'. Both terms are coined to summarize the differences in materials properties that exist between commercial heterogeneous catalysts and well-defined single-crystal model systems. Moreover, 'real' catalysts are usually polyphasic mixtures of various compounds (*e.g.* mixed metal oxides) which undergo different chemical transformations (*e.g.* phase transformation under reducing conditions) before the actual catalytic active state is formed [Christmann91]. Therefore, the composition of a commercial catalyst is up to now optimized empirically in screening methods. However, major efforts are dedicated to unravel the influence of preparation parameters of precursors on the catalytic activity. This could open up the opportunity for a rational strategy for developing more efficient heterogeneous catalysts. Controlled and reproducible preparation parameters are key components for this approach.

A straightforward approach to obtain a fundamental knowledge of the actual catalytic material is provided by the investigation of suitable model system using in-situ analytical techniques probing the geometric and electronic structure of a working catalyst. For bulk structural investigation under *in situ* conditions X-ray diffraction (XRD) and X-ray absorption spectroscopy (XAS) are particularly useful methods as they allow to perform the catalytic reaction under realistic conditions (*i.e.* high temperatures and pressures). The complementary character of both bulk methods affords structural information on the long and short range order scale. In addition, those techniques enable to follow solid state transformations occurring during activation of the precursor and catalysis. This methodology is a necessary prerequisite for catalysis studies that aim

at elucidating the correlation of bulk features with changes in product composition (*i.e.* catalytic activity or selectivity) [Schlögl93].

Although reactions in heterogeneous catalysis proceed on the surface of an active catalyst, the properties of the surface can be influenced or determined by the underlying bulk of the catalyst. It has been shown that the bulk of a copper metal catalyst can serve as a reservoir for reactive species (*e.g.* subsurface oxygen dissolved in the bulk [Bao94]). In addition, certain defects in the bulk can modify absorption properties of reactants on the catalyst surface thereby influencing the catalytic activity [Mavrikakis98]. Extended bulk defects can terminate at the surface and modify the surface properties (*e.g.* monoatomic steps at outlets of dislocation) which induces a change in the coordination of the surface atoms. Furthermore, the size and the morphology of catalyst particles are important parameters to consider as the surface area and the number of exposed active atoms is determined by the shape and size of the particles.

The objective of this work is a microstructural analysis of binary Copper/Zinc oxide catalysts using X-ray diffraction and X-ray absorption spectroscopy to establish a correlation between bulk structural parameters with catalytic performance. Binary Cu/ZnO catalysts are regarded as realistic model systems in which the complexity of an industrial “real catalyst” is reduced to a certain extent (no Al₂O₃ support, promoters and additives); yet they do provide information on the bulk chemical reactions (*e.g.* microstructure, possible phases and intermediates) contributing to the performance of the catalyst. The Cu/ZnO system is investigated for their bulk-structure-activity relationships both in methanol synthesis and methanol steam reforming.

1.2 Cu/ZnO catalysts in methanol synthesis and methanol steam reforming

Heterogeneous catalysts containing copper metal and zinc oxide constitute a technical important system for hydrogenation and dehydrogenation reactions. Cu/ZnO catalysts supported on alumina are common catalysts for the hydrogenation of carbon monoxide and carbon dioxide. These systems have found industrial use for low pressure methanol synthesis and for the low temperature water gas shift reaction. Methanol is produced from syngas (CO/CO₂/H₂).

The conversion of synthesis gas to methanol can be described by the following equation:



Furthermore, the reverse water-gas shift reaction needs to be considered:



Today desulfurized feedstock (pure CO/H₂ or CO₂-containing mixtures) allow low temperature (220 – 280 °C) and low pressure (70 – 100 bar) methanol synthesis and water-gas shift reaction. Methanol serves as an important bulk chemical whose world-wide demand amounted to 27 million tons in 1994. It is mostly used to produce formaldehyde (about 40 – 50 %) which is then used to make various types of plastic. Other new uses are in the manufacturing of methyl tert-butyl ether (MTBE) which is used as an octane enhancer in gasoline [Chinchen86].

It is the proposed synergistic effect in the binary copper/zinc oxide that makes this system interesting for investigations of the effects of structural and chemical promotion [[Klier82]. The maximum activity is observed in an intermediate compositional range of the catalyst (~ 70 mol-% Cu), whereas Cu and ZnO alone exhibit only negligible activity [Rasmussen87]. The nature and the location of the active site of this type of catalyst has been the subject of a vast number of publications in both surface science and solid state chemistry. Up to now four major theories concerning the nature of interaction between Cu and ZnO in the system can be found in the literature. Klier [[Klier82] proposed copper to be incorporated on interstitial and substitutional sites in the zinc oxide phase assuming three possible valence states Cu⁰, Cu⁺ and Cu²⁺. Klier's proposals were made within the framework of bulk defect equilibria based on scanning transmission electron microscopy (STM), X-ray data and optical spectra [Klier84]. Hence, the defect structure and, therefore, the bulk of the catalyst determines the catalytic activity. In a recent publication, Fujitani *et al.* on the basis of an XRD study corroborated the model of Klier *et al.* where they interpreted the effect of ZnO on the catalytic activity in terms of a formation of a Cu-Zn surface alloy [Nakamura96].

In contrast, Waugh *et al.* suggested that it is merely metallic Cu that carries the catalytic activity and that ZnO is only stabilizing a specific higher Cu surface area [Chinchen86]. Hence, in their opinion ZnO acts only as an inert support. Waugh's conclusion is based on the observed linear relationship between catalytic activity and copper surface area.

It is assumed that ZnO exerts a strong support influence on the copper crystallites acting as a dispersant, thus keeping a high surface area. The role of ZnO in creating active sites appears to be rather controversial and different views are presented in the summarizing literature [Spencer99], [Fujitani00]. Burch *et al.* and Spencer claim that ZnO is more than just an inert support [Burch90] [Spencer99]. Within the sequence of elementary reaction steps in methanol synthesis it is assumed

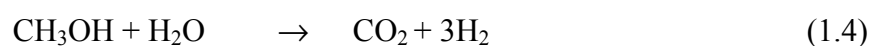
that the hydrogenation of formate adsorbed on metallic copper is enhanced by spillover of hydrogen from ZnO which acts as a reservoir of adsorbed hydrogen.

N.-Y. Topsøe and H. Topsøe have presented *in situ* IR measurements of 1 and 5 % Cu on ZnO catalysts during methanol synthesis [Topsøe99]. From the observed CO band shift the authors deduced the formation of a surface Cu-Zn alloy upon migration of ZnO moieties onto reduced Cu microcrystallites [Nakamura96].

In summary, previous investigations of the interaction (*synergy*) of Cu and ZnO have rationalized the real structure of Cu/ZnO catalysts either with morphological changes (dynamic wetting / non-wetting phenomenon) of copper dependent on the oxidation potential [Ovesen97], [Clausen94] or as a formation of additional phases (*e. g.* surface alloy) which leads to an electronic modification [Nakamura96], [Topsøe99]. The influence of temperature and pH on the preparation of hydroxycarbonate precursors and on the resulting active catalyst has been pointed out by Hadden *et al.* [Hadden95] and Li *et al.* [Li96]. In the past several authors described X-ray absorption studies on Cu-based catalysts that were carried out ex-situ on reduced samples after transfer. [Vlaic85], [Sankar86], [Kau89], [Arnukavalli93]. Analysis of the X-ray absorption spectra near the Cu K-edge (XANES) showed ambiguous results concerning the oxidation state of the reduced catalysts. Depending on the activation conditions (hydrogen reduction or treatment with reactant gases) and the Cu-concentration in the sample all three possible oxidation states of copper with various relative amounts were detected. An *in situ* structural investigation of the activation of a hydroxycarbonate precursor by combined X-ray absorption and diffraction is reported by Couves *et al.* [Couves91].

In addition to their use in methanol synthesis Cu/ZnO catalysts can be used to produce hydrogen by steam reforming of methanol with high selectivity and activity [Takahashi82], [Amphlett85]. Catalytic hydrogen production by methanol steam reforming is regarded as one of the most promising ways to produce hydrogen for operating solid polymer fuel cells. Nowadays, much attention is attracted by fuel cells as a clean and efficient energy source which is an environmentally sustainable process to cover the increasing demand in energy of electrical power for both automotive and stationary applications [Wild00]. Thus, methanol is considered as an alternative “automotive” fuel and could serve as a potential hydrogen source for mobile fuel cell applications [Peters00]. Current efforts are dedicated to the minimization of CO concentration which acts as a poison in fuel cell applications [Amphlett94].

The steam reforming reaction can be regarded as the reversed methanol synthesis reaction.



However, a detailed reaction mechanism is still under debate [Peppley99], [Breen99b], [Peppley99], [Jian93]. In a kinetic model by Peppley *et al.* it is assumed that different active phases are present for the methanol decomposition, methanol-steam reforming, and the water-gas shift reaction [Peppley99].

The Cu/ZnO system has been studied extensively after reduction and under working conditions for methanol synthesis [Clausen98b], [Clausen91], [Skryzypek94] and cited references therein). However, the active Cu phase for methanol steam reforming is not fully elucidated yet.

Previously, differences in the reduction kinetics of CuO/ZnO were mainly studied by conventional TPR methods [Fierro94], [Breen99a]. However, these methods cannot provide a structural evolution during reduction (*e.g.* evolution of different bulk phases). Fierro *et al.* studied the reduction of CuO/ZnO with different Cu/Zn ratios and found a promoting effect of ZnO on the reducibility of CuO [Fierro96]. The reduction kinetics of copper oxide was determined by thermogravimetric methods [Ruggeri82], [Plewa89] which afforded sigmoidal curves indicating a nucleation growth mechanism. Himelfarb *et al.* [Himelfarb83] and Porta *et al.* [Porta89] reported on an intermediary Cu₂O under reduction conditions, whereas this phase was not observed by Vong *et al.* [Vong90]. However, the detection of copper(I) oxide is based on ex situ investigations which may not represent the “real” state of the Cu phase under reduction conditions. Als-Nielsen *et al.* reported on an in situ detection of Cu₂O by time-resolved QEXAFS without further analyzing the growth kinetics [Als-Nielsen95]. Reitz *et al.* [Reitz01] observed Cu⁺ as a transient species in the reduction of CuO/ZnO catalysts by time-resolved XANES. Fernández-García *et al.* reported on the basis of a statistical analysis of TPR data of Cu/Al₂O₃ that the reduction process of copper aluminate proceeds via a two step mechanism [Fernández98]. Recently, Grunwaldt *et al.* observed dynamical changes of the Cu coordination number upon changes in the reduction potential by in situ EXAFS during methanol synthesis [Grunwaldt00].

Regarding the active state of Cu/ZnO catalysts, different authors claim that the ratio of Cu/Cu⁺ governs the methanol conversion [Idem96]. This interpretation is closely related to the model of the active Cu/ZnO phase in methanol synthesis developed by Klier [[Klier82]. The effects of preparation condition of precursors for Cu/ZnO catalysts upon precursors phases, surface structure and catalytic activity for steam reforming of methanol has been investigated by Shen *et al.* [Shen97]. Peppley *et al.* on the basis of a surface mechanism for methanol steam reforming proposed in a recent publication that the nature of the active sites differs according to their function [Peppley99]. The basic assumption was made that there are two distinct types of active sites on the surface of the catalyst whereas one site is created by the partial decomposition of a

hydroxy-carbonate phase that supports the hydroxylation of the intermediate surface formates. The second type of site which is formed by elemental copper was assumed to primarily support the decomposition reaction. However, no structural details of the bulk phases are provided which underlines the necessity to perform structural investigations concerning the relationship between the crystal phase structure of the catalyst and its activity and selectivity.

1.3 Outline of work

In this thesis XRD and XAS techniques are employed both *ex situ* and *in situ* because they conveniently complement each other for investigations of the bulk structure of Cu/ZnO catalyst after different preparation stages (*i.e.* after calcination and reduction) of Cu/ZnO catalysts precursors.

The activation of the CuO/ZnO precursor requires reduction with hydrogen in order to obtain the active copper phase. The reduction of CuO is a complex chemical process at the gas-solid interface which is considered as a crucial step that determines the microstructure of the catalyst, and, hence the activity. Upon reduction of the CuO/ZnO precursors small metallic copper particles supported on ZnO are obtained. Those copper particles are believed to be the carrier of the catalytic active phase. Therefore, the phase evolution and the copper crystallite growth is investigated *in situ* in more detail under different reduction atmospheres.

In a broader sense the Cu/ZnO system belongs to the important class of supported metal clusters as classified by Boudart [Boudart85]. The copper metal particles are typically larger than 50 Å. An X-ray diffraction line profile analysis is therefore an ideally suitable method to investigate microstructural parameters (*e.g.* crystallite size and microstrain). Based on the Cu crystallite size determined by XRD a Cu surface area can be estimated. This is shown in more detail in chapter 4.2. In order to rationalize structural influences apart from the Cu metal surface on the catalytic activity the concept of turn-over-frequency is applied (*e.g.* structure-sensitivity of the reaction [Boudart85]). This concept serves to explain why certain classes of reaction exhibit rates that depend strongly on particle size/surface structure and on catalyst composition. The idea that surface reactions may require a metal atom ensemble of specific size or structure has provided a foundation for establishing structure-property relationships in catalysis by metals.

There are indications that the structure and the composition of hydroxycarbonate precursor phase, which depends largely on the preparation conditions, may determine the performance of the active catalyst [Li96], [Hadden95], [Shen97]. It is assumed that microstructural properties of

the active Cu/ZnO catalyst depend to a large extent on the preparation conditions of the precursor. This work is in close cooperation with another PhD thesis [Bems01] in order to link preparation parameters (e.g. pH during precipitation and elemental composition) of Cu, Zn hydroxycarbonate precursors with structural characteristics obtained at different preparation steps (e.g. calcination, reduction, working catalyst). In that work, the influence of various preparation parameters of the wet-chemical coprecipitation of Cu, Zn hydroxycarbonates on the phase composition and thermal decomposition behavior for a large set of samples is addressed. A reactor set up is used which permits defined adjusting of important preparation parameters, e.g. temperature and pH value. The experimental design for the preparation of the samples investigated included two factors, i.e. variation of the Cu/Zn ratio (systematic series with varying Cu/Zn ratio) and variation of the pH during precipitation (constant pH of 7.0 and a decreasing pH). The CuO/ZnO precursors are obtained from thermal decomposition of coprecipitated copper, zinc hydroxycarbonates.

In chapter 3 the structure of the CuO/ZnO precursor is investigated *ex situ* by XRD and XAS. In addition, on the basis of X-ray absorption spectroscopy of CuO/ZnO precursors it is investigated how the phase composition of the multiphase Cu,Zn-hydroxycarbonate precursor affects the microstructure of the resulting Cu phase and if there is a structural dependence of the oxidic precursor on the phase composition of the hydroxycarbonate precursor. After reduction a detailed analysis of the microstructure of copper and zinc oxides crystallites is carried out by X-ray diffraction line profile analysis to detect the influence of the composition (i.e. Cu/Zn ratio) and the pH during preparation on the Cu and ZnO crystallite size and microstrain. In addition, a sample series (*decreasing pH*) is reduced at a higher temperature (673 K) to monitor the influence of the reduction temperature on the bulk structure. Furthermore, it is attempted to clarify the promotional role of ZnO in creating active sites in catalysis. It is assumed that this approach provides new insights into microstructural properties of this important catalytic system.

In chapter 4 correlation between the defective copper bulk structure and the methanol synthesis activity of Cu/ZnO catalysts are revealed. The results of the size and microstrain analysis provided in chapter 3 are utilized for this analysis. Catalysts with varying molar ratios (90/10 through 10/90) prepared according to the coprecipitation method at constant pH are correlated to microstructural characteristics of Cu and ZnO in order to obtain a possible dependence on bulk structural bulk parameters.

In situ X-ray diffraction and X-ray absorption spectroscopy (XAS) are employed as complementary bulk techniques in chapter 5 to elucidate bulk structural changes of Cu and ZnO during the activation and methanol steam reforming of Cu catalyst supported on ZnO. Those

investigations are performed on a large number of differently prepared CuO/ZnO catalyst and the aim of the experiments is to establish correlation of the bulk structure and activity. Binary CuO/ZnO catalyst with varying molar ratios prepared according to the coprecipitation method at constant pH ($pH = 7$) and decreasing pH are differently reduced in order to obtain catalyst with different structural properties but equal composition. First, the evolution of bulk phases during activation of the catalyst (*i.e.* reduction in hydrogen with ('wet') and without ('dry') additional water vapor) is investigated. Second, correlations between the bulk structure of Cu on ZnO and activity or selectivity in the steam reforming of methanol are presented. In addition, oxidation/re-reduction cycles are performed by adding oxygen to the feed in order to detect changes in the bulk phase and gas phase composition. EXAFS measurements are performed at the Cu K and the Zn K edge to analyze the changes in the local structure.

2 Theoretical and Experimental Details

2.1 Introduction

X-ray diffraction (XRD) and X-ray absorption spectroscopy (XAS) can be used to provide bulk structural information of heterogeneous catalyst systems. The combination of both experimental techniques offers the advantage of probing the bulk structure on two different length scales *i.e.* long-range (50 Å – 1000 Å) and short range-order (< 6 Å). In that respect both methods complement each other as XRD gives crystallographic information of the *d*-spacings and the unit cell parameters whereas XAS gives information of the coordination sphere of next nearest neighbor around an absorbing atom. While XRD requires crystalline solids to be conducted, XAS is also applicable for investigating amorphous materials that exhibit no crystallographic long-range order. In addition, the element specificity of XAS enables to selectively probe the local structure of different constituent elements in multicomponent catalyst (*e.g.* Cu/ZnO). Moreover, the capability of conducting both experimental techniques under *in situ* conditions make them very useful for investigating the active phase of a real catalyst under working conditions of a catalytic reaction. The successful combination of XRD and XAS for the structural elucidation of catalysts under operating conditions has been reported in previous studies [Couves91], [Sankar00], [Clausen98]. In the following the theoretical concepts of the data analysis of both methods are presented.

2.2 X-ray Diffraction and Line Profile Analysis

2.2.1 X-ray diffraction line broadening of small and ‘real’ particles

The periodic three dimensional array of atoms in a crystal solid scatters X-rays coherently leading to a constructive interference at specific angles (*i.e.* diffraction in analogy to optics). The first description of the diffraction of X-rays by a crystals was developed by Max von Laue [Laue13]. In 1913, W.H. Bragg and his son developed a simpler way of predicting diffraction phenomena in crystals assuming reflection of X-rays from crystallographic planes [Bragg13]. The scattered X-rays of each lattice planes interfere constructively with each other if the path difference Δl is an multiple integer of the wavelength. This is described by the Bragg equation:

$$\Delta l = 2 \cdot d \cdot \sin \theta = n \cdot \lambda \quad (2.1)$$

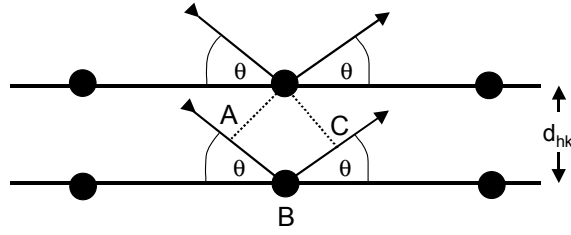


Figure 2.1: Bragg' law for the case of a rectangular grid, i.e. $AB = BC = d_{hkl} \sin \theta$

In Figure 2.1 a simple crystal is depicted with one atom at each lattice point. The path difference between the waves scattered by atoms from adjacent (hkl) lattice planes of spacings d_{hkl} is given by the sum of AB and BC.

If the incident and the scattered beam deviates $\delta\theta$ from the scattering angle θ a phase shift results. The phase difference between the first and the last phase dependent lattice plane (total number: n) amounts to:

$$\Phi = \frac{4\pi \cdot \delta\theta \cdot d \cdot \cos \theta}{\lambda} \quad (2.2)$$

The addition of the scattered phase-dependent waves resulting from all lattice planes of a crystallite yields the intensity I of the diffracted beam (assuming equal scattering amplitudes A):

$$I = n^2 \cdot A^2 \cdot \frac{\sin^2\left(\frac{\Phi}{2}\right)}{\left(\frac{\Phi}{2}\right)^2} \quad (2.3)$$

The line breadth of this function $\delta\theta$ depends on the number n of lattice planes. For small microcrystallites which are often present in catalyst samples the diffraction peaks are broadened because fewer lattice planes give rise to Bragg reflection. The most important formula for an estimation of the crystallite size is the *Scherrer* equation which relates the peak width of a broadened peak to the thickness of the crystal in a direction perpendicular to the diffracting planes. The size determined thereby refers to a coherently diffracting domain of crystallites giving a volume-weighted crystallite size averaged over all size distributions [Matyi87].

However, further imperfection due to residual stresses and strain contribute to the XRD line broadening and need to be considered. Strain in a crystalline material can result in two effects in diffraction pattern. If the stress is uniformly compressive or tensile (*macrostress*) the distances

within the unit cell will either become smaller or larger, respectively. This results in a shift of the peak position of the diffraction peak. (see Figure 2.2 b). If both, tensile and compressive forces act on a crystal, microstrain is produced and the resulting diffraction profile will be broadened about the original position. A number of sources can cause microstrain in crystallites: dislocation (most important source), vacancies, defects, shear planes *etc.* The effect of residual stress in a crystallite will cause a distribution of d -values about the normal, unstrained d_{hkl} -value. In Figure 2.2 c) the effect of *nonuniform* stress to a row of unit cells is depicted. While the average d -spacing remains constant, there is a distribution of d -values with an equivalent range of 2θ values resulting in a broadening of the diffraction line.

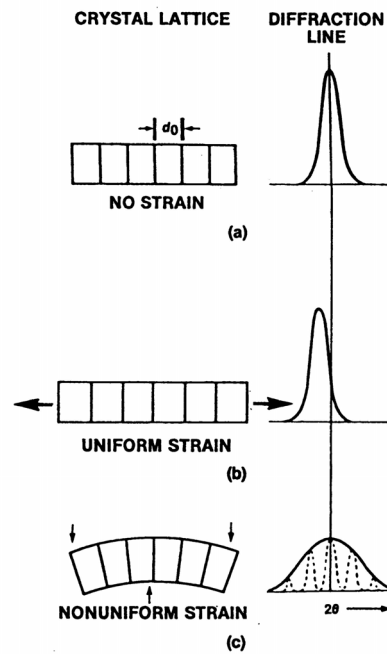


Figure 2.2: Schematic representation of the influence of no strain (a), uniform (b) and non-uniform (c) microstrain on the XRD profile (taken from [Jenkins96]).

A short-range distortion of lattice planes which indicates microstrain can be caused by various structural inhomogeneities (*e.g.* variation in composition due to non-stoichiometry, composition gradients or phase boundaries) [Delhez92]. In Figure 2.3 a strained unit cube of a crystal with height h and breadth L is shown to illustrate the effect of line (two dimensional) defects (*e.g.* edge dislocation) on the microstructure. The edge dislocation have moved various distances through the crystal. The total displacement of the top of the cube with respect to the bottom is Δ . Each dislocation contributes a small displacement δ_i . When a dislocation moves completely across the

crystal it causes a displacement b . In effect, the various deviations in the distance of the lattice planes might result in stain-broadening of the XRD line profile.

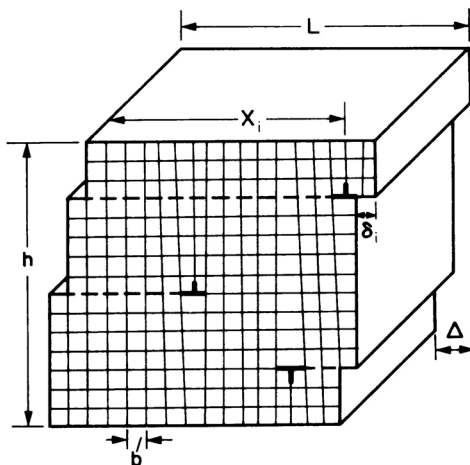


Figure 2.3: Schematic representation of strain caused by dislocation in a crystal (taken from [Gillmann62]).

2.2.2 XRD measurements in catalysis

In catalyst research XRD is applied on a routine basis to determine the number and amount of crystalline bulk phases present in the catalyst. In addition, the signal to background ratio compared to an internal standard of an X-ray pattern affords direct indication on the crystallinity of the sample [Ertl97]. Beside this valuable information further microstructural properties of the catalyst particles can be obtained by an analysis of the shape of a peak profile. Thereby, an indication of the defect structure of the material is gained. In a more detailed analysis of the peak profile the origin of the peak broadening can be determined.

The crystallite sizes is of principal importance for characterizing metal catalysts because the metal surface area and hence the number of exposed atoms (taken as the number of active sites) is determined by the shape and size of the metal particles. With a detailed particle size the resulting metal surface area can be estimated to apply the concept of turnover frequency. Although structural characterization of nanocrystalline materials can also be obtained from transmission electron microscopy (TEM) investigation, XRD offers additional benefits namely the easy applicability and averaging structural information over the whole bulk. The fundamental disadvantage of the Scherrer formula for the size determination is that other structural defects (*e.g.* microstrain and bulk defects) beside size effects are neglected. However, as it was shown in the previous section, both size and strain are main reasons for X-ray line broadening. It is assumed that both effects exhibit different dependencies on the scattering angle which would be one way to

separate both influences [Delhez92]. Microstrain in crystalline catalyst materials could be regarded as another important bulk parameter that could have an impact on the catalytic activity. Today, it is realized that defects in the bulk of a metal catalyst can modify the surface of a catalyst (*e.g.* adsorption properties) and thereby directly influencing the catalytic activity [Kampshoff94]. For example on the basis of self-consistent density functional calculations increased CO adsorption energies on strained metal surfaces have been predicted by [Mavrikakis98]. Therefore, it is desirable to determine the microstrain of the catalyst bulk experimentally as an additional important bulk feature.

The XRD profile shape can be mathematically described by analytical profile functions in order to determine numerical breadth parameters of a broadened diffraction peak. With the advent of Rietveld methods for structure analysis of crystalline powder materials, profile refining routines of the whole XRD patterns became available [Delhez92]. In addition, the profile functions implemented for the refinement allowed for modeling the shape of line profiles which are directly influenced by the imperfection and microstructural properties of the crystalline material. This method has greatly influenced the understanding of the profile of diffraction data.

A new technique for determining the microstructural properties of polycrystalline materials relies on pattern decomposition of diffraction peaks applying the Voigt function which was first introduced by Langford [Langford92]. This fitting procedure deconvolutes a single diffraction peak into the underlying Gaussian and Lorentzian profiles in real space. Thus, a separation of the origin of the X-ray line broadening influences by relating them to the respective profiles is feasible. This procedure is relatively straightforward applicable and affords information on the microstructure of polycrystalline materials in terms of mean crystallite size (coherently diffracting domain) and lattice distortions (microstrain).

Among other wide angle X-ray methods for determining microstructural properties the Voigt method stands out for its easy applicability in comparison to Fourier methods (Warren Averbach [Warren50] or the Williamson Hall method [Williamson53] both requiring higher orders of reflection. The basic concept for the application of the single line method was introduced by Keijser *et al.* [Keijser82]. According to that analysis selected reflection lines are analyzed separately to yield microstructural information and therefore this procedure can be used even if there are only a limited number of reflections available. XRD profile fitting methods are nowadays commonly employed in materials science and applied crystallography for characterizing nanocrystalline materials [Jian99], [Krill98], [Santra99] but have found only few application for catalytic relevant systems.

2.2.3 XRD peak profile refinement procedure using the Voigt function

The line profile of XRD peaks can mathematically be expressed as the result of a convolution of a variety of independent profile forms which can be symmetric or asymmetric [Wilson63], [Warren69]:

$$h_{2\theta} = g_{2\theta} * f_{2\theta} = \int_{-\infty}^{+\infty} g_{2\theta'} f_{2\theta-2\theta'} d(2\theta') \quad (2.4)$$

The experimental profile h is given by $h_{2\theta}$ whereas $g_{2\theta'}$ describes the broadened profile due to influences of the diffractometer. The function $f_{2\theta}$ represents the intensity distribution of a diffractogram under ideal experimental conditions. A solution of eq.(1) is not possible and therefore numerical deconvolution techniques (*e.g.* Stokes deconvolution [Stokes48]) are used for determining the intrinsic instrumental profile function f . In Figure 2.4 an experimental XRD profile is shown which has been deconvoluted according to Stokes using an instrumental function.

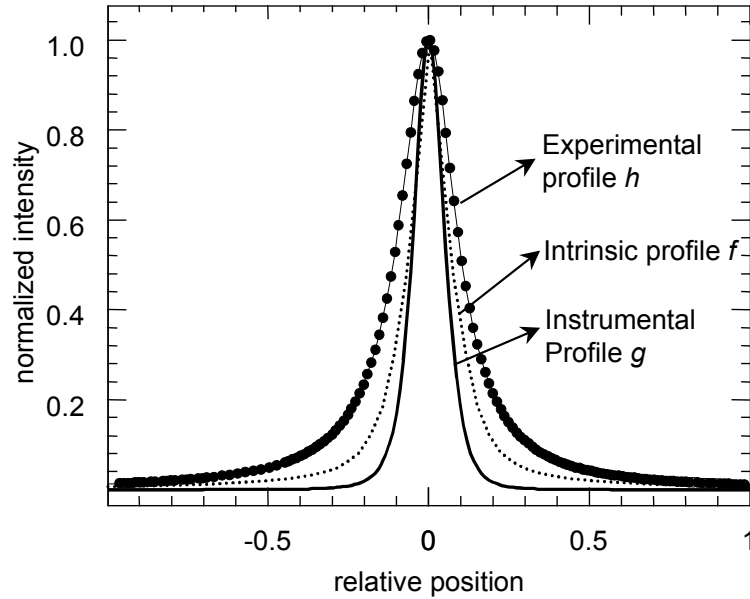


Figure 2.4: Intrinsic and instrumental line profiles after deconvolution of an experimental XRD peak normalized to a zero position using the Stokes deconvolution method.

The Voigt function, which is the convolution of a Lorentzian and a Gaussian function can be presented by:

$$I(x) = I_0 \frac{\beta}{\beta_L \beta_G} \int L(z) G(x - z) dz \quad (2.5)$$

where I_0 is the peak intensity, β is the integral breadth (= area/ I_0), β_L and β_G are the integral breadths of the Lorentzian and Gaussian components [Langford78].

The Lorentzian function is presented by:

$$L^V(x) = \left\{ 1 + \pi^2 x^2 / \beta_L \right\}^{-1} = \left\{ 1 + 4x^2 / (FWHM_L)^2 \right\}^{-1} \quad (2.6)$$

whereas the Gaussian function is given by the formula:

$$G^V(x) = \exp\left\{ -\pi^2 x^2 / \beta_G \right\}^{-1} = \exp\left\{ - (4 \ln 2) x^2 / (FWHM_G)^2 \right\}^{-1} \quad (2.7)$$

The Voigt function can be characterized by a shape factor ϕ , which is defined as the ratio of the full width at half peak maximum (FWHM) to the integral breadth,

$$\phi = FWHM/\beta \quad (2.8)$$

From the definition of the Voigt function, it follows that the convolution of two or more such functions represents also a Voigt function.

$$h(x) = f(x) * g(x) \quad (2.9)$$

The main reason for its introduction as a profile function to investigate the nature of diffraction line profiles is that the integral breadth of the Lorentzian and Gaussian function, β_L and β_G , can be related to microstructural defects causing to peak broadening. Those relations are only valid in a first approximation. The additive property of the integral breadths of Lorentzian functions and the squares of the integral breadths of Gaussian function for the measured and instrumental profile permits an easy “numerical” deconvolution to obtain the sample intrinsic peak broadening. The following equation illustrate how both intrinsic integral breadths β_{fL} and β_{fG} are obtained:

$$\beta_{fL} = \beta_{hL} - \beta_{gL} \quad (2.10)$$

$$\beta_{fG}^2 = \beta_{hG}^2 - \beta_{gG}^2 \quad (2.11)$$

An advantage of this deconvolution procedure is that more tedious corrections using Fourier methods like the Stokes correction [Stokes48] do not have to be performed prior to a profile refinement.

The Lorentzian and Gaussian functions are limiting cases for the application of the Voigt function. Therefore the shape parameter ϕ ranges in the interval of:

$$2/\pi \leq \phi \leq 2\sqrt{(\ln 2)/\pi} \quad (2.12)$$

The determination of the integral breadth of the Voigt function together with the integral breadth of the Lorentzian and the Gaussian function is carried out with the use of the software package WinXAS 2.0 [Ressler98] according to the principles of a single line method analysis [Keijser82].

Within the theory of the single line method it is generally assumed that the integral breadth of the Lorentzian contribution of the f-profile β_{fL} describes the extent of broadening due to size effects whereas the integral breadth of the complementary Gaussian breadth β_{fG} is caused exclusively by microstrain. The corresponding formulae for determining the respective values for crystallite size and strain are as follows:

$$\langle D \rangle_V = \lambda / \beta_{fL} \cos \theta \text{ [rad]} \quad (2.13)$$

giving the volume weighted average size $\langle D \rangle_V$.

$$\tilde{\epsilon} = \beta_{fG} / 4 \tan \theta \quad [2\theta] \quad (2.14)$$

affording the microstrain $\tilde{\epsilon}$ which describes two extreme values of the lattice spacing d :

$$\tilde{\epsilon} = \Delta d / d \quad (2.15)$$

The numerical analysis of the profile parameters presented above depends critically on the empirical assumption that a Gaussian distribution function is valid for microstrain and a Lorentzian distribution describes exclusively the distribution of crystallite sizes. However, it should be noted that other profile shapes for the size and strain broadening may exist and that the true distribution functions are not necessarily limited to the simple case assumed above.

2.2.3.1 Requirements and Procedure for using the Voigt function

Some conditions for the applicability of the deconvolutive X-ray line broadening analysis have to be met in order to use the Voigt profile for refinements. The peak profile has to be symmetric in shape and therefore the use of monochromatic K_α X-rays is of great importance. In addition, the shape factor ϕ of the experimental profile has to be inside the Voigtian range to yield meaningful fit results. Possible sources of error in line profile analysis are discussed in the following. Mainly insufficient counting statistics can cause errors in the quality of the data. However, in contrast to Fourier methods where truncation of lines is influencing the accuracy of the parameters, the results of a Voigt analysis are not equally affected because they are calculated from an analytical function

[Langford88]. The reliability of simplified integral-breadth methods when size and strain effects simultaneously broaden the profile has been investigated by Balzar and Popović [Balzar96]. Furthermore, the detailed analysis of only one reflection together with the assumptions implicitly made for the Voigt analysis (simultaneous occurrence of size and strain) introduce systematic errors. A quantification of this error is not readily possible and the absolute values of a single line analysis may therefore deviate from the values determined by of a multiple-line approach. Generally, the single-line analysis ignores order-dependent components of the integral breadths and, hence, both size and strain values decrease with increasing scattering angle [Langford88]. However, it has previously been shown that the single-line method gives reliable results with self-consistent relative values of size and strain underlining the applicability of this method. A more detailed description of experimental and analytical errors and an estimation of their order of magnitude can be found in ref. [Keijser82].

2.2.4 *Ex-situ* XRD measurements and line profile analysis

The *ex situ* XRD experiments were performed on a Stoe transmission diffractometer STADIP-P (Ge primary monochromator, Cu-K $_{\alpha 1}$ radiation), equipped with a linear position sensitive detector (PSD, internal resolution 0.01 °2 θ). The X-ray diffraction measurements were conducted in the Debye-Scherrer mode with a counting time of 4200 s/step. Copper and zinc oxide were used as internal standards for the line profile analysis to correct for instrumental line broadening. The copper used as an annealed standard for the line profile analysis was purchased from *Heraeus* (purity 99.98 %, sieve fraction 40 – 80 μm). A Williamson Hall analysis afforded a negligible strain contribution to the line broadening indication that this sample can be used as an “ideal” standard. The zinc oxide serving as an standard was purchased from *Johnson Matthey* (Karlsruhe) in a high purity (Puratronic, T. M. I. 10 ppm) and showed only size broadening effects. Both Cu and ZnO were taken as reference standards to individually take into account the different absorption coefficients of both crystalline phases. Thus different instrumental profile breath parameters were determined for Cu and ZnO used in the deconvolution procedure.

The deconvolutive line profile analysis according to the procedure described by Langford *et al.* [Langford78] was applied to single lines [Delhez82] to determine the underlying Gaussian and Lorentzian profile contributions as described in the previous section. The profile refinement was performed using the WinXAS v2.0 software package [Ressler98] on selected single (*hkl*) reflections of Cu (111) and ZnO (100), (110), (002) each for an interval $\Delta^{\circ}2\theta$ of 4 – 6 to ensure a

correct modeling of the tails of the peak and the linear background function. However, the ZnO (002) and the adjacent 101 reflection were refined together in one fit operation. The refinement afforded the integral breadths of the underlying Gaussian and Lorentzian function and the respective values of size and strain.

In order to estimate a specific copper surface area, $S_{\text{Cu(XRD)}}$, based on the XRD crystallite size a spherical shape of the copper crystallite was assumed with the crystallite size as a mean diameter. The surface areas ($S_{\text{Cu(XRD)}}$ and $S_{\text{ZnO(XRD)}}$) were calculated using a density ρ of $8.92 \text{ g}\cdot\text{cm}^{-3}$ for Cu and $5.673 \text{ g}\cdot\text{cm}^{-3}$ for ZnO [CRC99].

2.2.5 *In situ* XRD set-up and instrumentation

The *in situ* XRD experiments were conducted on a *STOE STADIP P* diffractometer in the *Bragg Brentano* scattering geometry equipped with a secondary monochromator and a scintillation counter operated in the stepping mode. Cu $K\alpha$ radiation was used at 50 kV and 30 mA. The *in situ* cell consisted of a *Bühler HDK S1* high temperature diffraction chamber mounted onto the goniometer. The cell was connected to a gas feed system for introducing different gases (He , O_2 and H_2) and, in addition, He saturated with liquids (H_2O or MeOH). Gas flows were controlled by *Bronkhorst* mass flow controllers ($\sim 100 \text{ ml/min}$ total flow). The cell volume is about 400 ml with a gas flow inlet underneath the sample holder, and gas flow outlet above the sample holder. The sample holder is a resistively heated stainless steel ribbon (12 mm wide). The sample temperature is measured with a stainless steel clad thermocouple (type K) connected to the heating band, and is regulated with a *Eurotherm* 818 PID controller. Temperature measurements were calibrated using different reference compounds whose characteristic temperatures of phase transition or decomposition are known (*e.g.* NH_4NO_3 , KClO_4). The experimentally determined thermal expansion coefficient of Si in the temperature range from RT to 700 K afforded a value of $\alpha = 2.2 \cdot 10^{-6} \text{ K}^{-1}$ (literature value: $\alpha = 2.2 \cdot 10^{-6} \text{ K}^{-1}$) which indicates that the sample holder did not move during heating. Typically, 12 mg of the catalyst sample were ground and then applied to the steel band in a slurry with acetone. Prior to any experiment the reactor was purged with He .

The gas phase over the sample was analyzed on-line with a *Balzers Prisma 200* quadrupole mass spectrometer (ionization source: tungsten filament, 300 V, 10 mA). Effluent gases were extracted with a heated capillary through a differentially pumped leak valve to the mass spectrometer. The measurements were performed in the multiple ion detection mode with a 1–2 second dwell time per mass using a faraday cup for detection. This multi component analysis

permits a quantitative analysis of the gas phase.

Hydrogen pulse experiments afforded a residence time distribution that is characteristic for a continuously stirred tank reactor. A residence time of 230 seconds for a flow of 100 ml/min indicates a good mixing of the gas phase. Furthermore, blank reactor tests ensured that under the reaction conditions employed no measurable activity was recorded.

The full width at half maximum (FWHM) and integrated intensity of XRD-lines were determined by fitting pseudo *Voigt* (fixed *Gauss* contribution) and *Lorentz* profile functions (more appropriate for strongly broadened profiles) to the Cu (111) peak. The *Scherrer* formula was used to estimate the crystallite size on the basis of the FWHM without taking other broadening effects and correction for instrumental broadening into account [Snyder93]. Calculation of theoretical X-ray powder patterns and lattice constant refinements were done using the software PowderCell v2.2 [Kraus99].

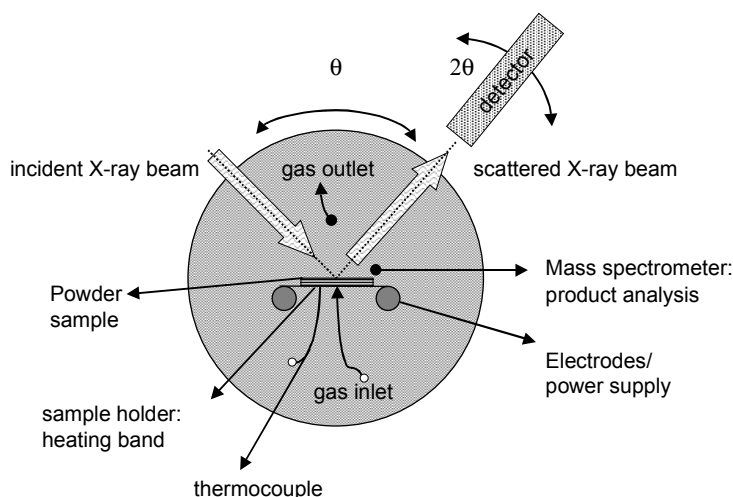


Figure 2.5: Schematic setup of the *in situ* XRD-cell in Bragg Brentano geometry.

2.3 X-ray absorption spectroscopy (EXAFS and XANES)

2.3.1 Theory of EXAFS and XANES

X-ray absorption spectroscopy (XAS) is a powerful technique that provides element specific structural information [Koningsberger00]. XAS probes the local order and, hence, can be applied to structurally disordered and ordered solids, and to dispersed species (*e.g.* small metal cluster). Similar to XRD X-ray absorption spectroscopy in the hard X-ray regime (5.0 keV to 30 keV) can

be performed *in situ* under working conditions ($p \geq 1$ bar, $T = 293 - 573$ K). Therefore, it offers a high potential for the structure determination in heterogeneous catalysis complementary to many standard methods such as X-ray diffraction or Raman spectroscopy.

X-ray absorption spectra exhibit a smooth decreasing intensity towards higher energy. When the X-ray photon energy is tuned to the binding energy of the core level of a constituent element, a sudden increase in the absorption coefficient $\mu(E)$, known as the absorption edge, occurs. For atoms, either in a molecule or embedded in a solid or liquid state, the absorption coefficient displays oscillatory variation as a function of photon energy. In Figure 2.6 a typical X-ray absorption spectrum of Cu is shown exhibiting the absorption edge (~ 9 keV) and the oscillatory part at higher energy ($E > 9.04$ keV). X-ray absorption spectra are commonly separated into several parts according to the spectral region. The so-called “X-ray absorption near edge structure” (XANES), refers to a region that begins before the absorption threshold E_0 and extends to about 40 eV ($E_0 - 100$ eV to $E_0 + 40$ eV). The “extended X-ray absorption fine structure” (EXAFS: $E_0 + 40$ to $E_0 + 1500$ eV) exhibits a modulation in total absorption with the energy of the incident photon which extends to several hundred eV above the absorption edge.

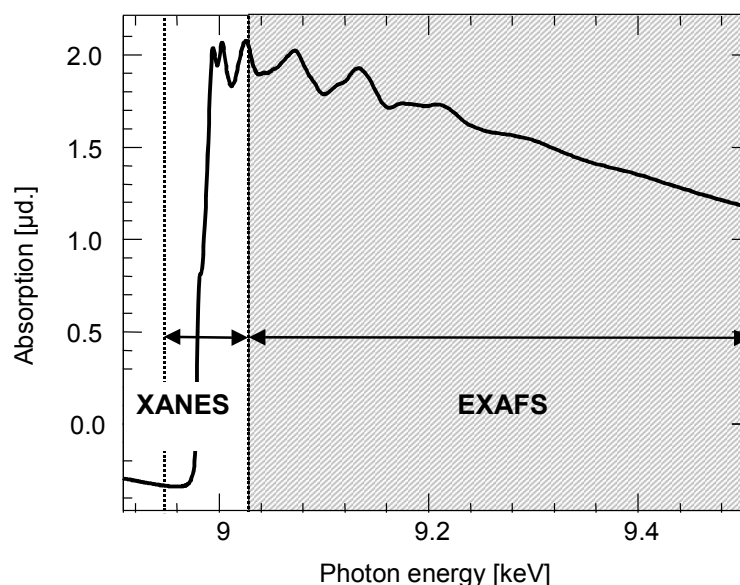


Figure 2.6: X-ray absorption spectra of Cu K edge of a Cu/ZnO catalyst with 70 mol-% Cu.

In the absorption of X-rays by matter the following basic model can be applied. When the energy of the incoming photons is high enough to excite an electron from a deeper core level to a vacant excited state or to the continuum a sharp increase in the absorption intensity is observed

(XANES). For higher kinetic energies of the ejected photoelectron scattering by neighboring atoms occurs (EXAFS-region). The outgoing wave is spherical (see Figure 2.7), and is scattered by all atoms surrounding the absorbing atom (the absorber). Both destructive and constructive interference processes occurs between the wave function of the outgoing electron and its scattered parts, leading to a modulation of the absorption coefficient. The position of maxima and minima in the resulting interference is energy dependent. As a consequence, there is a relation between the energy of the ejected electron and the distance between absorber and scatterer. The interference pattern varies between total construction or total destruction as determined by the path length of both waves which itself is a function of the distance of two neighboring atoms (see Figure 2.7). Therefore the oscillatory part of the EXAFS contains information about the local structure around the absorbing atom.

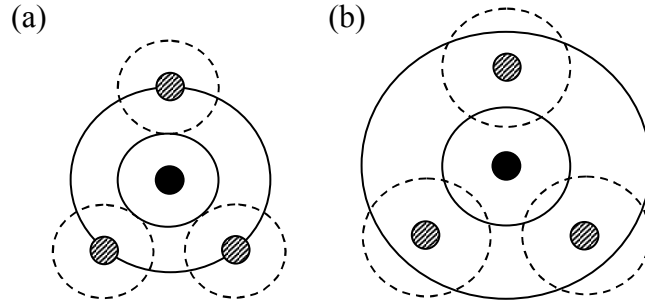


Figure 2.7: Schematic illustration of constructive (in phase, (a)) and destructive (out of phase, (b)) interference between out going and backscattered photoelectron wave from neighboring atoms.

The EXAFS function $\chi(k)$ is defined as the relative difference between the measured absorption $\mu(k)$ and the atomic absorption $\mu_o(k)$:

$$\chi(k) = \frac{\mu(k) - \mu_o(k)}{\mu_o(k)} \quad (2.16)$$

The relation between the modulated part $\chi(k)$ and the structural parameters contained in the absorption spectrum has been shown by Sayers, Stern, and Lytle [Stern70]. The EXAFS equation in the single scattering, plane wave approximation can be written as:

$$\chi(k) = \sum_j N_j / (kR_j^2) S_0^2 F_j(k) \exp(-2R_j / \lambda k) \exp(-2\sigma_j^2 k^2) \times \sin(2kR_j + \phi_j(k)) \quad (2.17)$$

with

N_j	number of atoms in the j_{th} shell
R_j	mean distance between absorber and the j_{th} shell
S_0^2	amplitude reduction factor
$F_j(k)$	the magnitude of the backscattering amplitude of the j_{th} neighbor
$\phi_j(k)$	phase shift due to the atomic potentials
λ	mean free path of the photoelectron
σ_j^2	relative mean square disorder between the absorber and an atom (Debye Waller factor)
k	the photoelectron wavenumber
E_0	threshold energy of the absorption process

A Fourier transform (FT) of the EXAFS with respect to the photoelectron wavenumber peaks at distances corresponding to the nearest-neighbor coordination shells of atoms. The conventional analysis of the EXAFS modulations contain several well-documented steps [Koningsberger88].

For disordered materials the Debye-Waller factor σ takes into account the fact that a spread in distance exists in the material due to thermal and structural disorder. The thermal disorder is induced due to the thermal lattice vibrations of the atoms at higher temperature. Static disorder of the solid is encountered if atoms of the same coordination shell have slightly different distances to the central atom. Static disorder is often present in catalyst system for instance in the case of highly dispersed small metal particles on a support. In the standard EXAFS formalism, originally derived by Sayers *et al.* [Sayers71], it is assumed that a gaussian pair distribution function, characterized by the Debye-Waller factor, σ , describes the structural disorder. For systems with pair distribution functions that deviate from a Gaussian shape, the cumulant expansion approach introduced by Bunker [Bunker83] can be used.

A major improvement of analyzing the X-ray absorption spectra has been achieved by *ab initio* calculations of multiple scattering processes. In recent publication it has been shown that the consideration of multiple scattering processes is essential beyond the first shell for the determination the local structure [Ressler99]. Using theoretical backscattering phases and amplitudes calculated with the *ab initio* code FEFF [Rehr94] the EXAFS analysis can be reliably carried out to distance out to 6 Å. Hence, EXAFS analysis is no longer restricted to the first shell and the use of reference compounds.

The XANES part of the spectrum is characterized by electron transitions and multiple-scattering events. The fine structure in the XANES is sensitive to changes in the local density of states and the spatial arrangement of scatterers around the absorber, hence, the edge region can provide information on the geometry of scatterers. A complete analysis of all multiple scattering paths that contribute to this fine structure yields the geometry of the scatterers around the absorber [Vaarkamp97]. In addition, the XANES analysis can provide information of the average valence of the catalyst system investigated due to the energy shift of the edge energy which proves useful in characterizing catalysts under reducing or oxidizing atmospheres. Furthermore, it is possible to simulate the near edge part of the absorption spectrum with a linear combination of the XANES of reference compounds. It is assumed that the absorbance in a set of spectra can be modeled as a linear sum of individual components. A principal component algorithm (PCA) can be used to determine the number and type of probable species yielding a quantification of phase mixtures. Moreover, the available time-resolution for XAS experiments in the quick-scanning EXAFS modes (QEXAFS) makes dynamical structural investigations (*e.g.* kinetic studies) of solid state processes feasible [Ressler01].

In summary X-ray absorption spectroscopy (XAS) is very well suited to study catalysts and probing the local structure around a particular element at temperature and pressure. The information on the short and medium order range obtained by XAS (*e.g.* type and number of neighbors, distance between atoms, and disorder) together with the long-range order (*e.g.* crystallite size and microstrain) determined by XRD enables a more detailed description of the bulk structure of a “real” catalyst system.

2.3.2 XAS experiments and instrumentation

X-ray absorption experiments can be carried out in different experimental set-up using synchrotron radiation. The XAS experiments described in this work were all performed in transmission geometry at *Hamburger Synchrotronstrahlungslabor*, HASYLAB. A schematic set-up of a typical beamline is depicted in Figure 2.8. Different optical elements are required to obtain a monochromatic and focused X-ray beam. In transmission experiments the intensity of the incident beam I_0 and the transmitted I_1 beam are measured by an ionization chamber. A reference sample (usually metal foils of the elements investigated), placed between the second and the third ionization chamber (I_3) is used as an internal standard for the energy calibration.

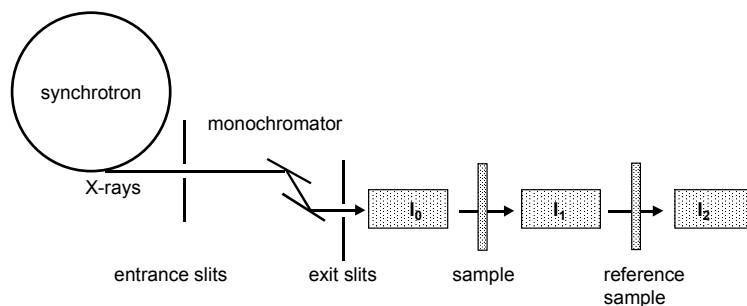


Figure 2.8: Schematic representation of experimental set-up for a transmission XAS experiment

The absorption is calculated from:

$$\mu_{\text{sample}} = \ln(I_0/I_1) \quad (2.15)$$

The *in situ* XAS experiments were carried out in the transmission mode in a flow-reactor at atmospheric pressures (designed by M. Hagelstein, T. Neisius *et al.* ESRF, in a collaborative effort with the Fritz-Haber-Institut, Berlin). In Figure 2.9 a schematic setup of the *in situ* reactor is depicted. The “pellet-type” reactor is suitable for reduction and re-oxidation experiments with hydrogen and oxygen without detectable mass transport limitations. The reaction temperature and reactant gas flows were controlled with an *Eurotherm* PID temperature controller and *Bronkhorst* mass flow controllers, respectively. A calibrated mass spectrometer (QMS200 *Pfeiffer*) operated in a multiple ion detection mode permitted a quantitative analysis of the gas phase during the experiments.

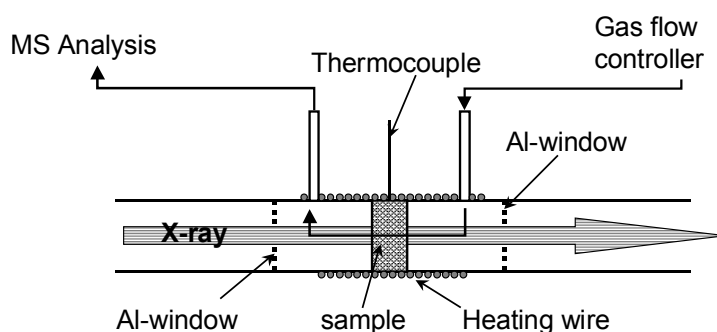


Figure 2.9: Schematic setup of the *in situ* XAS-cell operated in transmission geometry.

2.3.2.1 *Ex situ EXAFS measurements*

XAFS measurements of the calcined precursors (CuO/ZnO samples prepared at constant pH and at decreasing pH with Cu/Zn 100/0, 90/10, 80/20, ..., 10/90, 0/100) were performed at the Cu K edge ($E = 8.979$ keV) and the Zn K edge ($E = 9.659$ keV) at room temperature in transmission at beamline E4 (HASYLAB, Hamburg). The storage ring operated at 3.6 GeV with injection currents of 150 mA. For the absorption fine structure (EXAFS) analysis, a smooth atomic background, $\mu_0(k)$, was obtained using cubic splines. The radial distribution function $FT(\chi(k))$ was obtained by Fourier transforming the k^3 -weighted experimental $\chi(k)$ function, multiplied by a Bessel window, into the R space.

2.3.2.2 *In situ XAS measurements*

The *in situ* XAS experiments were performed at beam line X1 at the Hamburger Synchrotron Radiation Laboratory, HASYLAB, using a Si(111) double crystal monochromator. The storage ring was operated at 3.6 GeV with injection currents of 150 mA. CuO/ZnO-samples prepared according to both preparation methods were investigated (*constant pH* samples C70/30, C60/40, C40/60, C10/90 and *decreasing pH* samples D70/30, D60/40, D40/60). The samples were mixed with boron nitride (mass ratio CuO/ZnO: BN = 1:6) and 45 mg of the mixture was pressed with a force of one tone into a 5 mm in diameter self supporting pellet. The absorption jump at the Cu K edge was ~ 1.5 . XANES spectra were measured in the Quick-EXAFS mode with a time resolution of 15 s/spectra (8959-9100 eV). *In situ* EXAFS spectra were measured after oxidation and re-reduction to reveal structural changes of the Cu and Zn phases present.

2.3.3 *In situ XANES and EXAFS Data Analysis*

The software package WinXAS v2.0 [Ressler98] was used for a statistical analysis of time-resolved Cu K edge XANES data to reveal qualitative and quantitative information on the copper bulk phases under TPR and steam reforming conditions. Identification of the number of phases was achieved by principal component analysis (PCA) of the experimental XANES spectra. Reference spectra of these phases were then used in a least-square fitting procedure of the time-resolved spectra to determine the fraction of each phase present [Ressler00]. For the absorption fine structure (EXAFS) analysis, a smooth atomic background, $\mu_0(k)$, was obtained using cubic splines. The radial distribution function $FT(\chi(k))$ was obtained by Fourier transforming the k^3 -

weighted experimental $\chi(k)$ function, multiplied by a Bessel window, into R space. EXAFS data analysis was carried out using theoretical backscattering phases and amplitudes calculated with the ab initio multiple-scattering code FEFF 7 [Rehr94]. Single scattering and multiple scattering paths in the employed model structures were calculated up to 6 Å for Cu metal and up to 5 Å for ZnO with a lower limit of 2.0 % in amplitude with respect to the strongest backscattering path. In addition to the Zn-O and Zn-Zn distances additional Zn-Cu shells were employed assuming Zn on Cu sites in fcc Cu metal. EXAFS fitting and simulation were performed using the standard EXAFS formula (k range from 2.0 to 13 Å⁻¹, R range 1.5 to 6.0 Å) [Rehr92]. Structural parameters that are determined by a least-squares EXAFS fit to experimental spectra are (i) one E_0 shift for all scattering paths in the Cu bulk structure, (ii) Debye-Waller factors for single-scattering paths, (iii) single scattering shell distances, R_i , and (iv) a third cumulant [Bunker83] to account for slight deviations from a Gaussian pair distribution function. Coordination numbers (CN) were kept constant in the refinement. This restriction was necessary to reduce the number of free running parameter (N_{free}) to much less than the number of independent parameters (N_{ind}) in the experimental data used. EXAFS refinements reported here were carried out in R space to fit the magnitude and imaginary part of a Fourier transformed k^3 -weighted experimental $\chi(k)$. More details about the XAFS fitting procedure employed can be found in reference [Ressler99].

2.4 Preparation and characterization of CuO/ZnO precursor

In close collaboration with another thesis, the preparative part of the catalyst precursors was performed by B. Bems, Fritz-Haber-Institut. Binary hydroxycarbonate precursors of a systematic series with varying Cu/Zn molar ratios (100/0, 90/10, 80/20, 70/30, 60/40, 50/50, 40/60, 30/70, 20/80, 10/90, 0/100) were obtained and are denoted in the following according to their nominal Cu/Zn ratio. The CuO/ZnO samples investigated were prepared according to the coprecipitation method, both at a constant pH of 7.0 and with decreasing pH, from metal nitrate and sodium carbonate solutions. Calcination of the hydroxycarbonate precursors at 600 K for 3 h in a muffle furnace in air afforded mixed CuO/ZnO systems. More preparative details are given elsewhere [Bems01].

Throughout the XRD and XAS experiments described in this work two sample sets of systematic series with varying Cu/Zn ratio prepared at constant pH of 7.0 and with decreasing pH were investigated to trace back the influence of the pH-value and the Cu/Zn ratio during precipitation.

For the XRD characterization of the reduced catalyst 20 mg of the obtained mixed oxides (sample set prepared according to constant and decreasing pH) were placed in a quartz tube and reduced with 5 vol-% H₂ in He (120 ml/min) applying a heating ramp of 5 K/min to 523 K and a holding time at 523 K of 2 h. A second sample series of the decreasing pH batch was heated to 673 K with no subsequent heating time to prevent the formation of brass alloys. Afterwards, the samples were sealed into 0.3 mm Lindemann capillaries in a glove box (Ar atmosphere with O₂ ≤ 1 ppm, H₂O ≤ 1 ppm) to prevent oxidation of the highly dispersed copper phase.

Specific surface areas were calculated by applying the BET method to the nitrogen isotherms obtained at liquid nitrogen temperature on samples outgassed at 423 K using a Quantasorp jr. (Quantachrom) adsorption instrument.

The nomenclature of all the CuO/ZnO samples investigated including the pH of the preparation and characterization of the calcined precursor with respect to CuO and ZnO crystallite size and the BET surface area is given in Tab. 2.1.

2.5 Catalyst screening for methanol synthesis activity

The catalytic activity for methanol synthesis was determined using a microreactor set-up which is described in more detail in ref. [Hinrichsen00]. In a collaborative effort with M. Muhler *et al.* the catalytic activity measurements were conducted at Ruhr-Universität-Bochum. The set-up was equipped with a calibrated quadrupole mass spectrometer for quantitative product analysis (Balzers GAM 422). The activity measurements were conducted at 493 K under atmospheric pressure in a glass lined U-tube reactor using typically 100 mg of 250 – 355 µm sieve fraction of the catalyst. In the activity measurements the mass balance closed to within 5 – 10 % by the use of He as an internal standard and, hence, the experimental error is estimated to be of similar order of magnitude. Prior to the reaction the sample was reduced in 2 vol-% H₂ in He ramping the temperature at 1 K·min⁻¹ up to 448 K and holding this temperature over night. Finally, the temperature was increased up to 513 K with a linear heating rate of 1 K·min⁻¹. The flow was switched to 100 vol-% H₂ until the reduction was completed as verified by mass spectrometry (no further H₂O evolution). The reduction was followed by a Cu area determination performed by passing 1 vol-% N₂O in He over the catalyst at 300 K (reactive frontal chromatography [Chinchen86], [Chinchen87]). For calculation of the exposed Cu surface area a mean surface atom density of 1.47·10¹⁹ m⁻² [Anderson85] was used. The reproducibility of the surface area determination according to N₂O RFC was ± 1%. Methanol synthesis activity was measured at

493 K with a modified space velocity of $500 \text{ Nml (min} \cdot \text{g}_{\text{cat}})^{-1}$ to determine activities within the kinetically controlled regime. The composition of the feed gas was 10 vol-% CO, 4 vol-% CO₂, 72 vol-% H₂ in He. The activity of the Cu surface was expressed as a normalized turn-over frequency (TOF) defined as the number of product molecules of MeOH formed per surface atom Cu per second, which was normalized to the maximum TOF.

Tab. 2.1: Chemical composition and characterization of calcined CuO/ZnO precursors. Calcination conditions: 695 K for 3 h in stagnant air.

Sample name	nominal Cu/Zn ratio [at.%]	chemical composition ^a Cu/Zn [at.%]	pH during precipitation	CuO crystallite ^b size [Å]	ZnO crystallite ^b size [Å]	S _{BET} [m ² /g]
C100/0	100/0	100/0	<i>constant (7.0)</i>	137	-	33
C90/10	90/10	91/09	<i>constant (7.0)</i>	75	- ^c	70
C80/20	80/20	82/18	<i>constant (7.0)</i>	41	- ^c	76
C70/30	70/30	73/27	<i>constant (7.0)</i>	40	40	76
C60/40	60/40	63/37	<i>constant (7.0)</i>	43	46	82
C50/50	50/50	53/47	<i>constant (7.0)</i>	43	46	89
C40/60	40/60	45/55	<i>constant (7.0)</i>	46	45	96
C30/70	30/70	30/70	<i>constant (7.0)</i>	47	60	74
C20/80	20/80	22/78	<i>constant (7.0)</i>	- ^c	75	77
C10/90	10/90	11/89	<i>constant (7.0)</i>	- ^c	80	53
C0/100	0/100	0/100	<i>constant (7.0)</i>	-	110	41
D100/0	100/0	100/0	<i>decreasing</i>	125	-	26
D90/10	70/30	91/09	<i>decreasing</i>	109	92	43
D80/20	70/30	82/18	<i>decreasing</i>	88	89	44
D70/30	70/30	74/26	<i>decreasing</i>	100	71	43
D60/40	60/40	66/34	<i>decreasing</i>	78	66	52
D50/50	50/50	53/47	<i>decreasing</i>	58	64	65
D40/60	40/60	45/55	<i>decreasing</i>	62	77	49
D30/70	30/70	30/70	<i>decreasing</i>	48	65	68
D20/80	20/80	22/78	<i>decreasing</i>	60	73	69
D10/90	11/89	11/89	<i>decreasing</i>	- ^c	110	49
D0/100	0/100	0/100	<i>decreasing</i>	-	170	34

^a Cu/Zn ratio was determined by X-ray absorption experiment. ^b calculated using the Scherrer equation for CuO (111) and ZnO (100). ^c not determined because of poor crystallinity.

2.6 In situ catalytic tests for methanol steam reforming activity

2.6.1 TPR measurements of catalyst precursor

Reduction of the precursors was performed in the *in situ* XRD cell following a temperature program either with 2 vol-% H₂ (denoted in the following as ‘dry’ reduction) or with 2.5 vol-% H₂ and 3 vol-% H₂O (‘wet’ reduction) both in a He-flow of 100 ml/min. Between 433 K and 523 K an XRD pattern measurement was taken every 5 K at a constant temperature while applying a temperature ramp between every measurement resulting in an effective heating ramp of 0.5 K/min. Thus, the uncertainty in on-set temperatures of reduction is 5 K. For the temperature programmed reduction measurements a counting time of 2 s/step and a step width of 0.04 °2θ was chosen for an interval of 41 – 46 °2θ.

In the XAS-cell temperature programmed reduction (TPR) runs were performed with 2 vol-% H₂ (*constant pH* samples) and 8 vol-% H₂ (*decreasing pH* samples) from 448 – 523 K with a temperature ramp of 5 K/min.

2.6.2 Methanol steam reforming activity screening

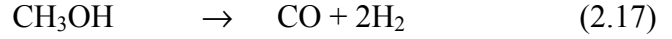
The catalytic activity of the Cu/ZnO samples for steam reforming of methanol was determined at atmospheric pressure at 523 K using saturators for methanol and water at room temperature. For a typical *in situ* experiment 12 mg of sample were employed in the *in situ* XRD set-up and ~ 6 mg were used in the XAS-cell. After temperature programmed reduction and cooling the sample to 298 K, the binary Cu/ZnO samples were exposed to a MeOH/H₂O vapor in a ratio of 4/1 (c(MeOH) ~ 6 vol-%, c(H₂O) ~ 1.5 vol-%) diluted in He; total flow in the XRD cell = 120 ml/min, XAS cell = 25 ml/min. Afterwards the temperature was increased from RT to 523 K at 20 K/min. Reactants and products (MeOH, H₂O, H₂, CO₂, and CO) were quantitatively monitored with a mass spectrometer (time resolution 12 s per scan). In order to monitor changes in the phase composition during oxidation and reduction cycles, oxygen (20 vol-%) was added to the feed at (523 K) for intervals of 100 min (*in situ* XRD) and 10 min (*in situ* XAS) while the reaction was progressing.

The following reactions of methanol are considered to arrive at a carbon balance:

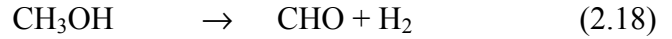
i) Steam Reforming Reaction:



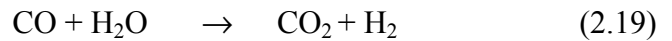
ii) Methanol Decomposition:



iii) Dehydrogenation of Methanol:



iv) Water-gas shift reaction:



The selectivity refers to CO_2 instead of H_2 because reactions other than the desired steam reforming (2.16) produce hydrogen as well. An error is introduced by not differentiating the CO_2 stemming from the water-gas shift reaction. However, this reaction occurs to a much smaller extent. The selectivity and conversion were determined according to the following formulae:

$$\text{Conversion } X_{\text{MeOH}} = \frac{c(\text{MeOH}_{in}) - c(\text{MeOH}_{out})}{c(\text{MeOH}_{in})}$$

$$\text{Selectivity } S_{\text{CO}_2} = \frac{c(\text{CO}_{2out})}{c(\text{MeOH}_{in}) - c(\text{MeOH}_{out})}$$

In order to express the hydrogen production activity in terms of a turn over frequency (*i.e.* number of product molecules of hydrogen formed per surface atom Cu per second) the number of exposed Cu surface atoms must be estimated. The number of surface atoms was calculated for the Cu surface area using a mean surface atom density of $1.47 \cdot 10^{19} \text{ m}^{-2}$ [Anderson85]. The copper surface area was determined using the XRD crystallite size and assuming a spherical copper crystallite shape. We have previously shown that the Cu surface area thus determined agrees well with the surface area based on chemical titration with N_2O [Günter01].

2.7 Transmission electron microscopy (TEM) characterization

2.7.1 Application of TEM on catalysts

In addition to the bulk structural methods presented above which yields structural information

averaged over the whole bulk, electron microscopy is used in selected cases to provide locally resolved images of the structure and detailed particle morphology of the calcined and reduced Cu/ZnO catalyst. The most widespread application of transmission electron microscopy in catalytic research are measurements of crystallite sizes and distribution of supported particles in order to determine the dispersion of the active phase. In addition, due to the high resolution the observation of the inner particle structure is possible. Usually supported catalyst particles are not single crystals but consist of several differently oriented crystallites separated by grain boundaries or twin planes [Delannay84].

In Transmission electron microscopy (TEM) a primary electron beam of high energy and high intensity passes through a sample while the attenuation of the beam depends on the density and the thickness of the sample investigated. The transmitted and diffracted electron are used to obtain structural information. The transmitted electrons form a two-dimensional projection of the sample, which is subsequently magnified by the electron optics to produce a so-called bright field image.

Another application of TEM is dark-field imaging which is useful in selectively studying samples containing a mixture of two different crystalline phases (*e.g.* Cu and ZnO). Dark-field images of supported particles are obtained from the diffracted electron beams. Therefore the incident electron beam is tilted so that the objective aperture excludes the unscattered electrons but accepts some of the electrons diffracted by a preferred oriented set of planes of the particle. Thereby the interaction between copper metal particle and the supporting ZnO can be investigated.

2.7.2 Experimental details

Transmission electron microscopy was conducted on some selected oxide precursors (samples of constant pH and decreasing pH preparation) on a Phillips CM 200 FEG TEM with an electron beam of 200 kV energy. For the microscopic study the catalysts samples were suspended in an ethanol slurry and the resulting solutions were dispersed on holey-carbon films supported on gold grids.

For the investigation of a reduced sample a commercial catalyst with a Cu/Zn ratio of 70/30 was reduced in 5 vol-% H₂ at 523 K and a sample for electron transmission was prepared in a glove box to prevent any contact to air. For deposition of the sample on the grid no solvents were used.

3 Ex situ Studies on Copper oxide /Zinc oxide

3.1 Copper Oxide/Zinc Oxide Precursor

3.1.1 Introduction

The preparation of an active Cu catalyst is usually carried out in three stages. First the wet-chemical preparation yields a multiphase hydroxycarbonate by coprecipitation with the components in highly dispersed form. The starting substances for the preparation of binary Cu, Zn hydroxycarbonate precursors are nitrate solutions of copper and zinc. The second step comprises the calcination of the precursor in air after several steps of post-preparation treatment of the hydroxycarbonates (*e.g.* aging and drying). During calcination of the precursor the hydroxycarbonates decompose with the evolution of CO₂ and H₂O yielding the oxidic phases. In the last step of preparation the calcined precursor is reduced to afford the active catalyst.

During sequence of preparation stages the structure of the active catalyst is assumed to be predetermined to some extent by the precursor phase composition. The phase composition of the coprecipitated Cu, Zn-hydroxycarbonate is considered to have a strong effect on the thermal decomposition behavior during calcination in air and, hence, is assumed to affect the CuO and ZnO microstructure (*e.g.* crystallite size) [Shen97].

In this section the results of the structural characterization of the CuO/ZnO precursor by XRD, EXAFS and in some selected cases by TEM will be presented. Although all of these techniques are applied *ex situ* it is thought that *ex situ* analysis method is adequate to afford a first insight into the structural interaction of the calcined and reduced catalysts. An *in situ* approach to the reduced system employing XRD and XAS is presented in chapter 5.

The CuO/ZnO precursors were obtained after calcination of the respective hydroxycarbonates precursors at 600 K. The sample sets of the *constant pH* and the *decreasing pH* preparation were investigated to detect dependencies of structural properties on the preparation conditions and the elemental composition. X-ray diffraction and profile fitting is employed to determine the crystallite size of copper and zinc oxide. X-ray absorption spectroscopy is useful to detect changes in the local structure around the Cu and Zn atoms, *i.e.* the next nearest neighbor. This is especially useful because the thermal decomposition affords a structural disordered mixed oxide at an intermediate compositional range with a lack of long-range order. In addition, electron microscopy is used to supplement the results of the bulk sensitive methods (XRD and EXAFS) with locally resolved images of the morphology and size of the particles.

3.1.2 XRD characterization of CuO/ZnO

Figure 3.1 shows experimental XRD patterns of systematic series of calcined CuO/ZnO samples of the constant pH (a) and the decreasing pH (b) series. Both series of XRD pattern exhibit a gradual increase in line width of the CuO (002) and (111) reflection at 35° and 39° 2θ with increasing Zn content. For the ZnO (100) and (101) reflection at 32° and 36° 2θ on the opposite are narrowing of the line width can be noticed. At an intermediary compositional range (from 70/30 to 30/70) the individual reflection lines of CuO and ZnO are broad and strongly overlapping. Upon comparison of the diffraction data of both sample sets the diffraction lines of samples obtained at decreasing pH are narrower in line width which points to a larger crystallite size. In order to further analyze the changes in crystallite size the Scherrer formula is applied to the CuO (111) and the ZnO (100) peak. In Figure 3.2 the crystallite sizes of CuO and ZnO based on those peaks are displayed together with the BET surface area. It can be seen that similar crystallite sizes for CuO and ZnO are determined for an intermediate compositional range (*e.g.* CuO and ZnO crystallite size of 45 Å for the sample C50/50). Furthermore, the results show that the maximum in BET surface area is reflected by a minimum in crystallite size of CuO and ZnO. For the sample set prepared at constant pH a minimum in CuO and ZnO crystallite size is obtained in the range from 30 – 60 mol-% Zn with only small differences in size between both phases. For the CuO and ZnO crystallite sizes of the decreasing pH sample batch a gradual decrease in crystallite size with increasing Zn concentration can be noted with the smallest crystallite size (CuO = 45 Å, ZnO = 60 Å) observed at a concentration of 70 mol-% Zn.

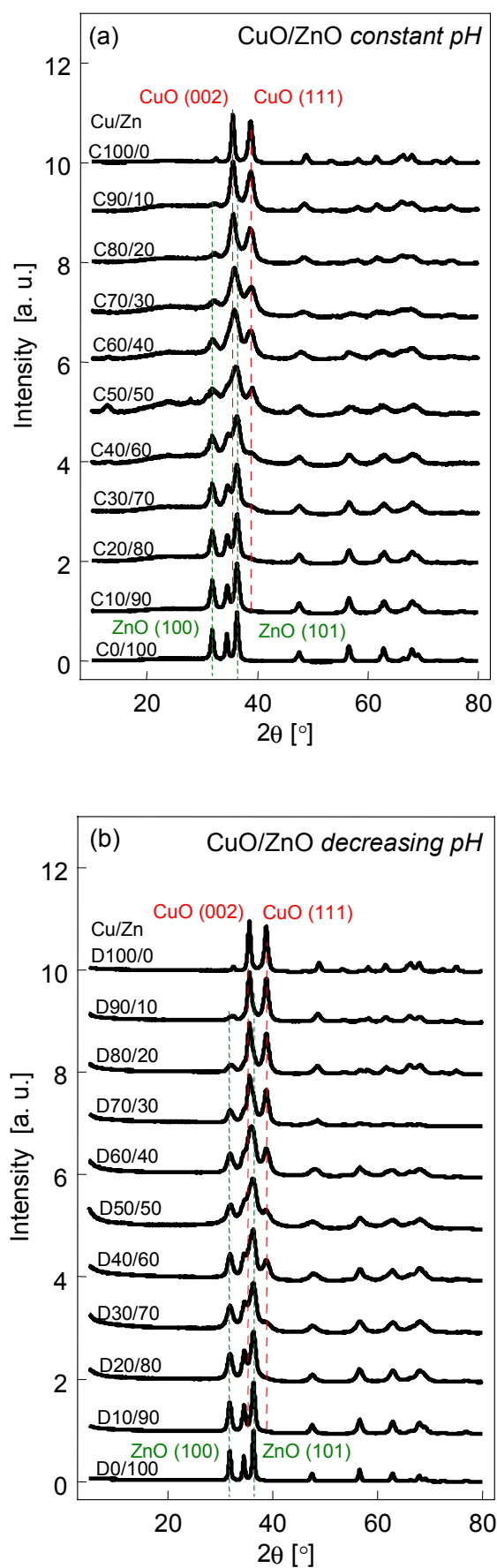


Figure 3.1: XRD patterns of a systematic series of calcined CuO/ZnO samples prepared at constant pH (a) and decreasing pH (b). Characteristic (hkl) lines for CuO (002), (111) and ZnO (100) and (101) are indicated.

A more detailed XRD line profile analysis of the CuO and ZnO peaks is not feasible due to the overlap of the most intense diffraction lines in the interval between $25 - 38^\circ 2\theta$ especially for the intermediate compositional range. Hence, no further conclusion can be drawn concerning possible additional broadening effects of the X-ray line. However, EXAFS can be employed in that case to afford information of the next nearest neighbors of Cu and ZnO.

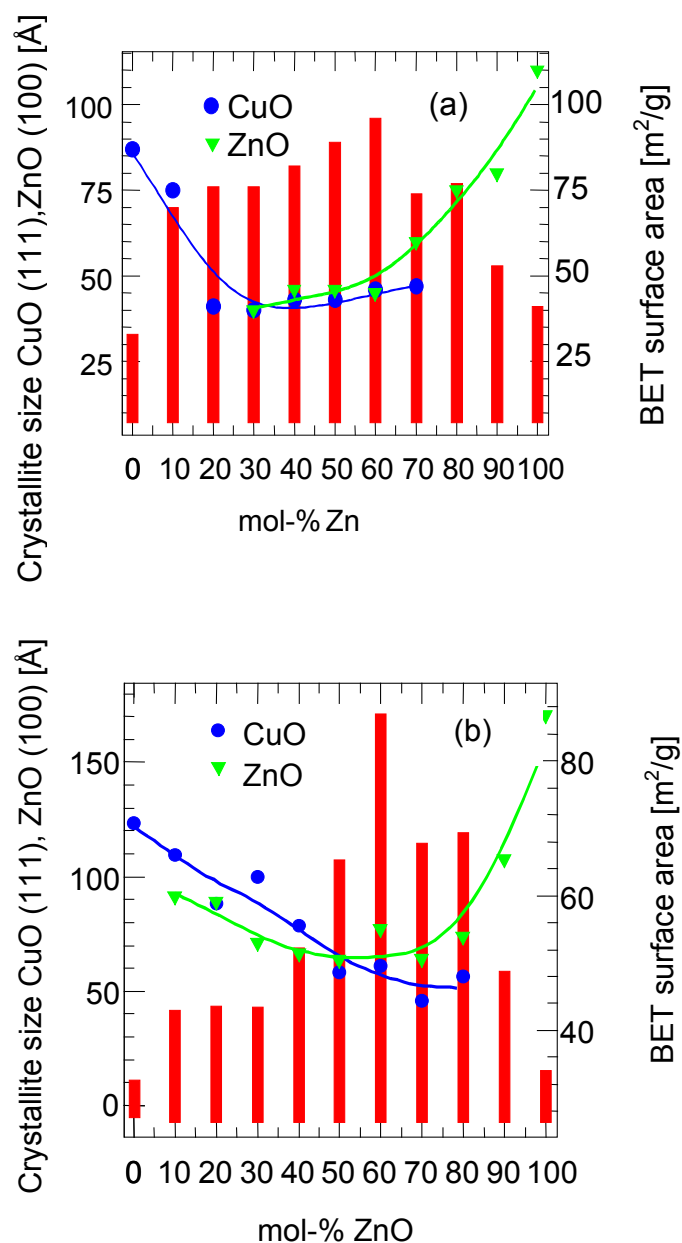


Figure 3.2: Crystallite size of CuO and ZnO after calcination at 600 K based on the (111) or (100) reflection for CuO and ZnO respectively together with the corresponding BET data. (a) constant pH preparation, (b) decreasing pH preparation.

3.1.3 EXAFS measurement of CuO/ZnO

In order to further analyze the local structure of the CuO/ZnO precursor which exhibit a high degree of disorder EXAFS was applied to both sample sets of calcined precursors. The EXAFS analysis in the section is restricted to a qualitative analysis of the Fourier transformed $\chi(k)$ to detect changes in the local structure with composition and preparation treatment.

In Figure 3.3 the Fourier transformed (FT) Cu K and Zn K edge spectra for the whole series of CuO/ZnO for the constant and the decreasing pH preparation sample batch is displayed. The peak distances of the plots are not phase corrected for the phase shift and hence are shifted to lower R values. The first peak in Figure 3.3 (a) at ~ 1.8 Å corresponds to the first oxygen shell around the Cu absorber. Beside the Cu-O peak a second distinct peak can be seen at ~ 2.4 Å which corresponds to a Cu – Cu distance. For the Zn K edge Fourier transformed $\chi(k)$ three distinct peaks can be observed at ~ 1.5 Å, ~ 2.4 Å and at 4 Å. The second peak corresponds to of a Zn – Zn distance. All series of the RDF exhibit distinct deviations in intensity from a supposed linear dependence of structural features on composition. For the Cu K edge the series of FT($\chi(k)$) spectra exhibit a considerable damping in amplitude for the first two coordination shells at a Zn concentration of 50 and 60 mol-% (Figure 3.3 (a), (b)). This is detectable for both preparation batches at the same concentration. Furthermore, the Zn K edge FT($\chi(k)$) reveals for the Zn – O and Zn – Zn nearest neighbor shells a reduction in amplitude at a Zn concentration of 30 and 50 mol-% Zn for the constant pH series and at 40 and 60 mol-% Zn for the decreasing pH samples.

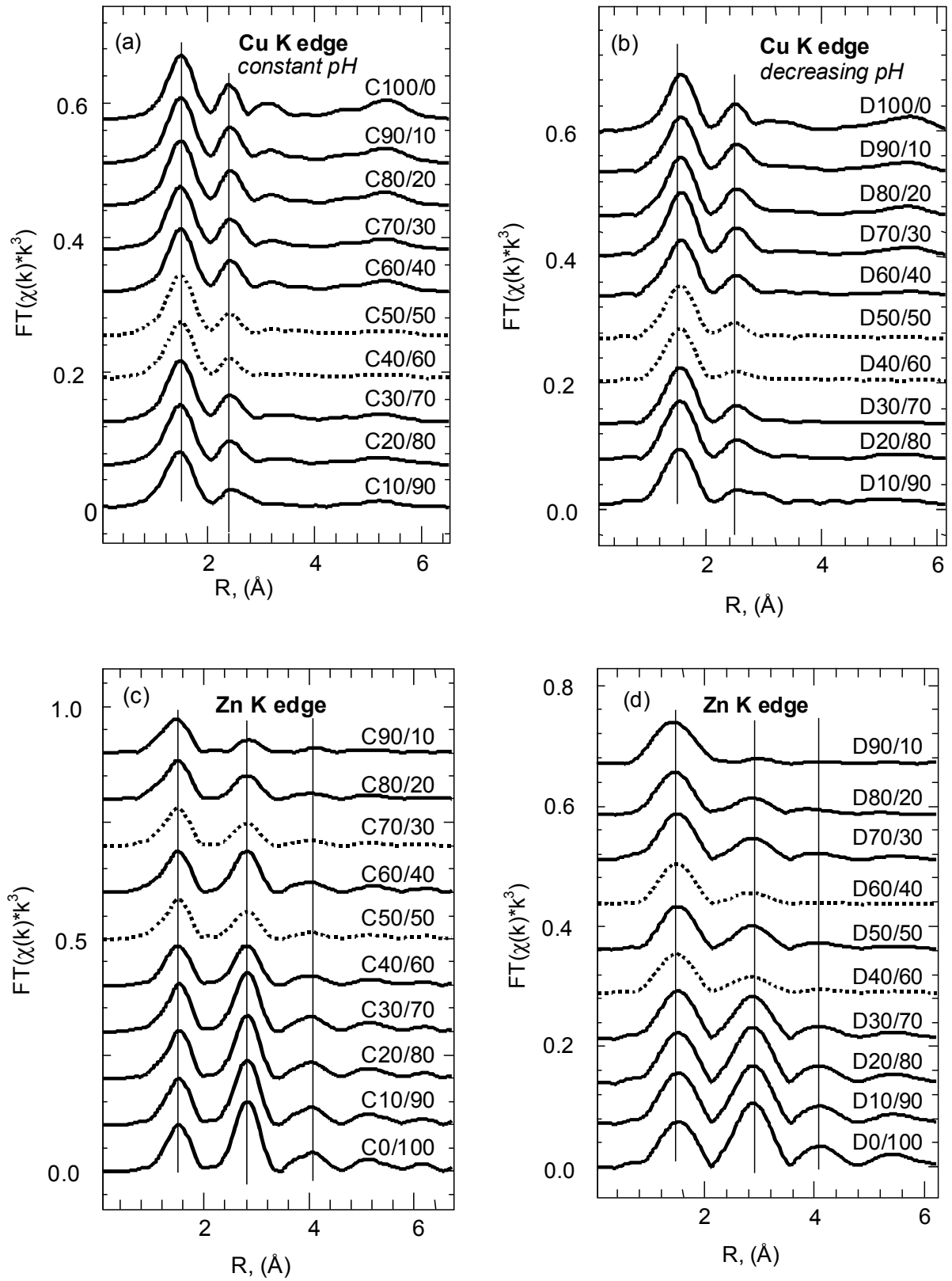


Figure 3.3: Fourier transformed experimental Cu K edge $\chi(k)$ of systematic series of calcined samples prepared at constant pH (a) and at decreasing pH (b) and corresponding Fourier transformed experimental Zn K edge $\chi(k)$ of the constant (a) and decreasing (b) pH sample set. Dashed lines represent spectra that deviate from a linear trend in structure with composition.

In a further step to analyze the changes in the local structure the imaginary part of the EXAFS part of the experimental Fourier transformed EXAFS $\chi(k)$ is investigated in more detail. In Figure 3.4 the FT $\chi(k)$ of pure ZnO, CuO obtained from decomposition of malachite and calcined binary samples prepared at constant pH with 10 and 20 mol-% Zn are depicted. A significant difference in the imaginary part of the FT($\chi(k)$) for the sample 10/90 at about 2.5 Å (indicated with an arrow) is observed compared to that of ZnO (Figure 3.4 (a)). This deviation is less pronounced for the imaginary part of the FT($\chi(k)$) of sample 80/20 which resembles more that of ZnO. The Cu K edge FT($\chi(k)$) spectra of the sample 90/10 and 80/20 exhibit a considerable reduction in amplitude at above 3 Å compared to the FT($\chi(k)$) fo CuO (lower part of Figure 3.4).

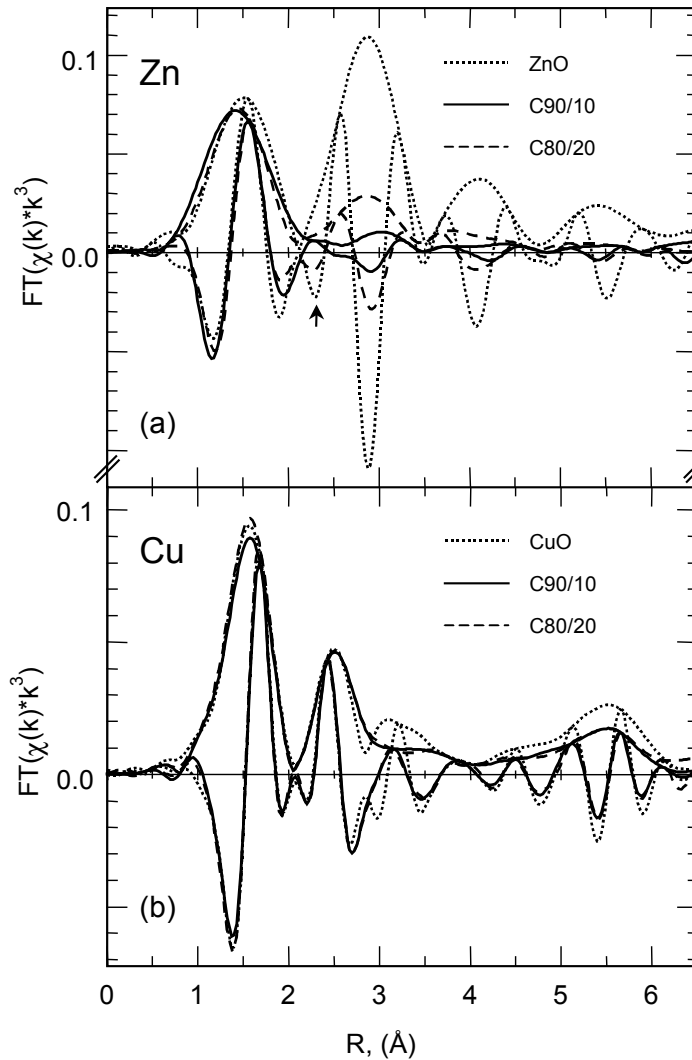


Figure 3.4: Experimental Fourier transformed Zn K edge $\chi(k)$ (magnitude and imaginary part) of ZnO, and calcined samples with Cu/Zn of 90/10 and 80/20 (a), and experimental FT($\chi(k)$) of Cu K edge of CuO and calcined samples with Cu/Zn of 90/10 and 80/20 (b).

3.1.4 Transmission electron microscopy of CuO/ZnO

Selected CuO/ZnO precursors were investigated by transmission electron microscopy to determine their crystallite size and morphology as a function of Cu/Zn ratio. The transmission electron micrographs of selected CuO/ZnO precursors with 60 and 70 mol-% Cu are given in Figure 3.5. It can be seen that the samples consist of a highly interdispersed network of single crystalline particles. Although at the magnification used lattice fringes can well be observed (see inset in Figure 3.5) no easy identification of the individual particles is feasible. For particles of the calcined precursor obtained at decreasing pH a significantly higher particle size (> 100 Å) can be observed. For the samples prepared at constant pH smaller agglomerates can be seen which is also in agreement with the smaller CuO and ZnO crystallite sizes determined by XRD for this sample series.

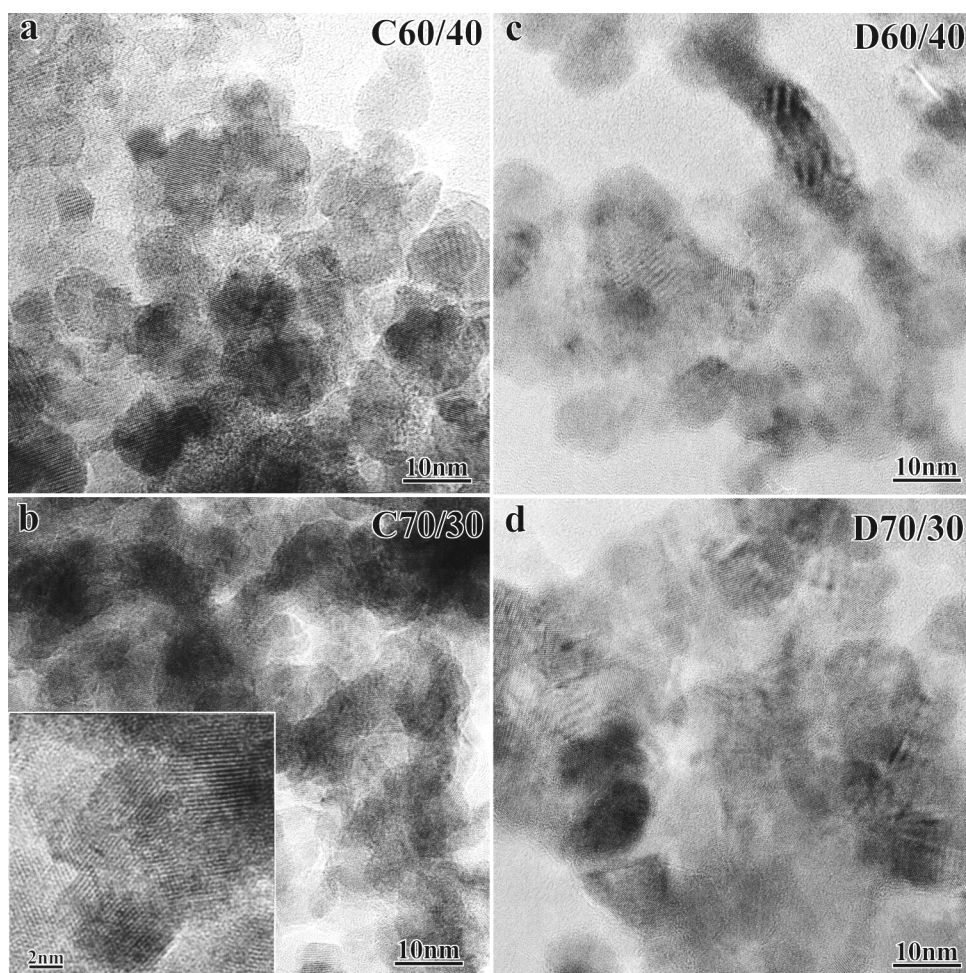


Figure 3.5: Transmission electron micrograph of calcined samples C60/40 (a), C70/30 (b), D60/40 (c), and D70/30 (d). The magnified inset of a catalyst particle of sample C60/40 shows lattice fringes.

In general, the mean size of the particles taken as the diameter of the crystalline parts is in close agreement with the XRD-size (see Figure 3.2). This confirms that the particle size of the CuO/ZnO precursor determined by XRD refers to a primary particle size with no considerable amount of x-ray amorphous phases present that do not contribute to the X-ray line broadening.

3.1.5 Discussion

The structural investigation of CuO/ZnO precursors by XRD and XAS provides evidence that a high interdispersion of both oxidic phase is achieved by the mild calcination conditions. The crystallite sizes of CuO and ZnO were found to be a function of the Cu/Zn ratio. The mutual interaction of both CuO and ZnO is indicated by the TEM images which showed the fine interdispersion of CuO and ZnO crystallites. The sizes determined by TEM are in accordance with those afforded by XRD line profile analysis which proves that no large amounts of amorphous oxides are formed. The EXAFS proved differences in structural features (amplitude) for CuO and ZnO that deviate from a supposed linear trend in composition.

The significant deviations in the intensity of the experimental Fourier transformed $\chi(k)$ for distinct Cu/Zn ratio can be related to changes in the phase composition of the hydroxycarbonate precursor. A phase assignment of the hydroxycarbonate phases obtained from a coprecipitation procedure at constant pH based on XRD and thermoanalytical data is described in detail elsewhere [Bems01]. Three multiphasic composition ranges in the hydroxycarbonate precursors can be distinguished as a function of composition. The first region extends from 0 mol-% Zn to ~15 mol-% Zn and encompasses the pure malachite phase ($\text{Cu}_2(\text{OH})_2\text{CO}_3$) as well as the zincian-malachite phase ($((\text{Cu,Zn})_2(\text{OH})_2\text{CO}_3)$). The second region extends from 20 mol-% Zn to ~50 mol-% Zn and encompasses the transition from the zincian malachite to the aurichalcite phase ($((\text{Cu,Zn})_5(\text{OH})_6(\text{CO}_3)_2)$). The third region at a Zn concentration larger than 50 mol-% encompasses the transition of aurichalcite to the hydrozincite phase ($\text{Zn}(\text{OH})_6(\text{CO}_3)_2$). The phase composition was found to be sensitive to the pH during the coprecipitation procedure. For hydroxycarbonates obtained at decreasing pH a similar phase assignment can be obtained [Bems01] but for the second region the existence of the aurichalcite phase is shifted to a lower Zn concentration (~40 mol-%). This is reflected by the decreased amplitude of the FT $\chi(k)$ of ZnO observed at this concentration (see Figure 3.3).

The change in short-range order of ZnO and CuO in samples with 10 mol-% Zn (see Figure 3.4) cannot be ascribed to a crystallite size effect because XRD measurements on the oxide precursors yielded an average crystallite size for CuO of ~75 Å. EXAFS data analysis using

theoretical phases and amplitudes of CuO yielded an enlarged metal-metal distance for shells above 3 Å. This indicates that Zn may occupy specific Cu sites in the CuO lattice rather than being randomly distributed. It has been shown in the literature that CuO can form solid solutions with several bivalent cations (*e.g.* Mg, Co, Zn, and Ni, concentration < 10 mol-%) [Delorme58]. Therefore, we propose that the inclusion or solid solutions of ZnO in the CuO bulk enables the formation of a Cu-Zn alloy at a temperature of 523 K. Otherwise, temperatures above 900 K would be required for the formation of brass from ZnO and CuO under reducing conditions. A possible dissolution of ZnO in CuO as evidenced by the EXAFS results may be related to the crystal structure of zincian malachite (rosasite) in which Zn and Cu cations occupy non-equivalent sites [Roberts86]. After mild calcination the local arrangement is preserved which could result in the observed Zn “ordering” in the CuO matrix. A second explanation for the structural disorder observed is possibly related to the incomplete removal of OH- and carbonate groups during thermal decomposition.

3.2 Microstructural characteristics of reduced Cu/ZnO catalysts

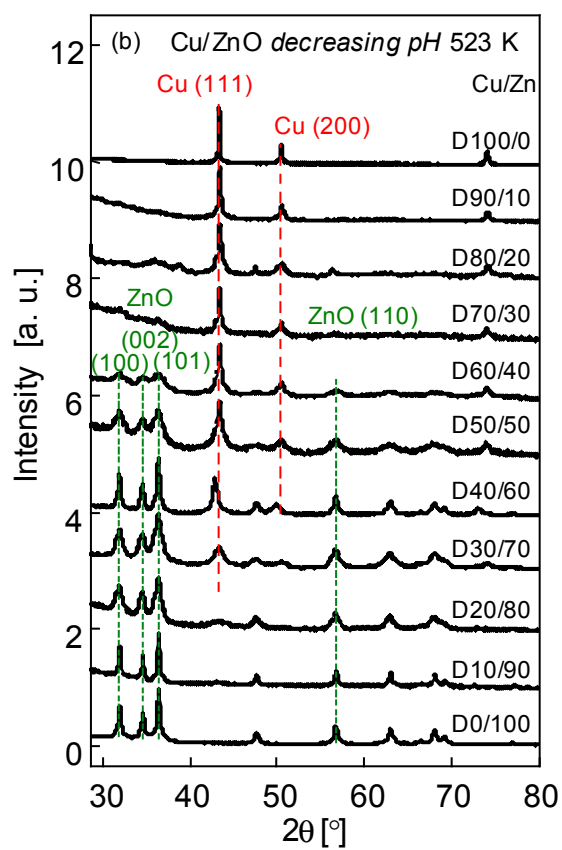
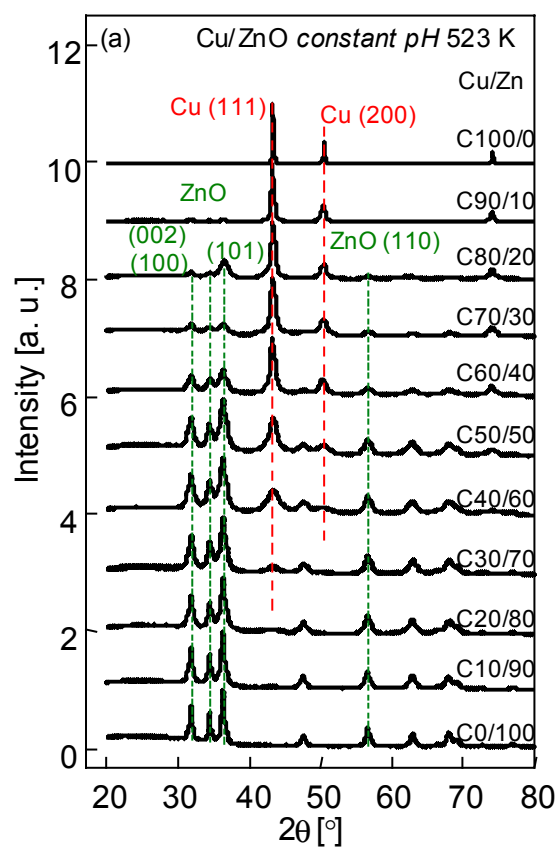
3.2.1 Introduction

During the course of the preparation of an active Cu/ZnO catalyst the reduction of the calcined CuO/ZnO precursor is the last stage. The activation is most often carried out by reduction with hydrogen or CO in which copper oxide is reduced to metallic copper. The structural properties of the copper phase are dependent on the Cu/Zn ratio and the preparation conditions. In this section the microstructural characteristics of copper and zinc oxide after reduction in hydrogen at 523 and 673 K are investigated. An X-ray diffraction line profile analysis based on the *Voigt* profile is applied to selected Cu and ZnO reflection peaks in order to separate the broadening influences due to crystallite size and microstrain effects. Those microstructural characteristics indicate deviations from the ideal structure (*i.e.* structural imperfection) that can originate from concentration variations, finite crystallite size and various kinds of defects such as dislocation, stacking faults, micro-twins, and stresses. The influence of the reduction temperature, the pH during coprecipitation of the hydroxycarbonate precursor, and the Cu/Zn ratio crystallite sizes and strain will be investigated. This approach aims at relating the so-called ‘synergistic’ effect in the Cu/ZnO system to the defective bulk structure of copper and zinc oxide.

In addition, transmission electron microscopy is utilized for a reduced commercial catalyst to investigate the morphology and the microstructural orientation of the Cu and ZnO particles.

3.2.2 X-ray diffraction Data

The experimental XRD pattern for the various sample batches of Cu/ZnO reduced at 523 K and 673 K are shown in Figure 3.6 (a) – (c). The XRD pattern indicate that the reduction conditions used (5 vol-% H₂) afforded metallic copper in all cases and that the ZnO phase is unaffected. No additional oxidic copper phases were detected indicating a complete reduction of CuO and the successful exclusion of oxygen contamination during sample preparation. In all XRD pattern series a significant broadening of the Cu (111) and (200) reflection at 43 °2θ and 50 °2θ, respectively, is observed with increasing ZnO content in the sample. The ZnO (*hkl*) lines exhibit an opposed dependence on the composition as their diffraction lines narrow with decreasing Cu content. After reduction at 673 K (see Figure 3.6 (c)) the triplet of ZnO reflections centered around 35 ° 2θ is much better resolved for samples with low Zn-content than in the case of the low temperature reduction (*e.g.* sample D60/40). No significant narrowing of the ZnO (*hkl*) lines is observed in the compositional range from 50/50 to 10/90.



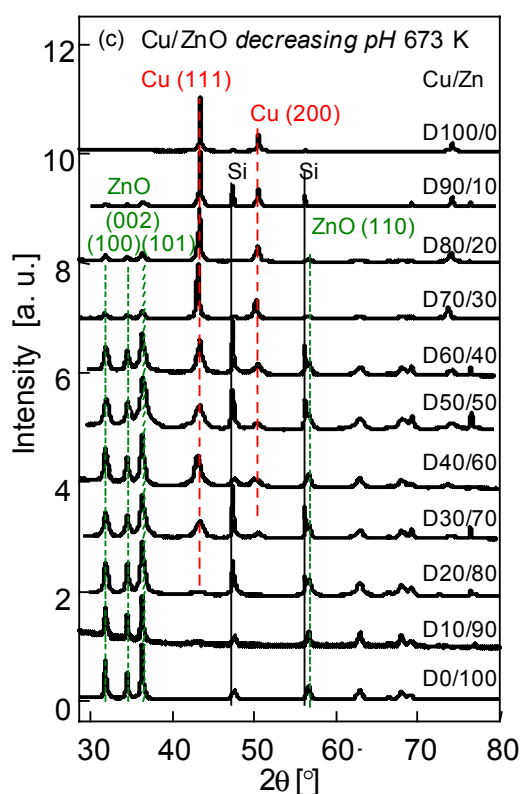


Figure 3.6: XRD patterns of systematic series of reduced Cu/ZnO catalysts. Samples have been prepared according to the (a) constant pH, and (b) decreasing pH preparation method after reduction with hydrogen at 523 K, and (c) decreasing pH preparation after reduction with hydrogen at 673 K, reflections due to an internal standard Si are marked. Characteristic (hkl) lines for Cu (111) and ZnO (002), (100), (101) and (110) are indicated.

3.2.3 Microstructural characterization of Cu

A Cu (111) peak of a sample with 60 mol-% Cu (reduced at 523 K; decreasing pH) refined with a Voigt function is shown in Figure 3.7 together with a difference plot after subtraction of the linear background function.

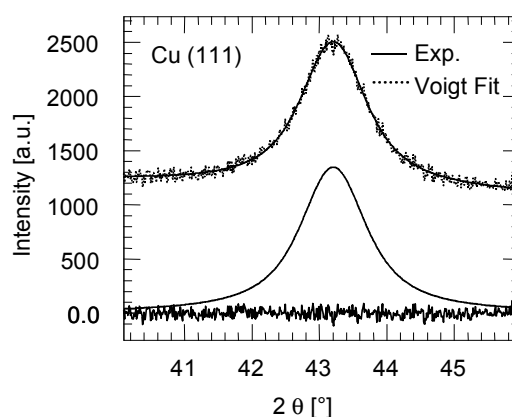


Figure 3.7: Experimental data and refined profile of a Cu (111) reflection using a Voigt function. The difference plot, measured minus refined profile, is shown in the lower part of the graph (sample with 60 mol-%, decreasing pH reduced at 523 K).

The numeric results (*e.g.* shape factor, deconvoluted integral Lorentzian and Gaussian breadth) of the profile fitting of the constant pH sample series reduced at 523 K and the calculated crystallite size and microstrain are summarized in Table 3.1. The shape parameter ϕ ranges in all cases within the allowed region for the Voigt function. With increasing ZnO-concentration the shape parameter ϕ increases indicating that the character of the employed Voigt function is more approximated by a Gaussian.

Table 3.1: Integral breadth parameters and microstructural properties of Cu based on XRD line profile analysis for various samples prepared at constant pH after treatment with H_2 at 523 K.

nominal Cu/Zn ratio [%]	shape factor ϕ	deconvoluted integral Lorentzian breadth β_{fL} [° 2 θ]	crystallite size $\langle D \rangle_V$ [Å]	deconvoluted integral Gaussian breadth β_{fG} [° 2 θ]	microstrain $\tilde{\epsilon}$ [%]
100/0	0.84	0.09	1000	0.07	0.07
90/10	0.73	0.45	210	0.16	0.17
80/20	0.68	0.77	123	0.16	0.18
70/30	0.71	1.03	92	0.19	0.22
60/40	0.69	1.08	88	0.04	0.05
50/50	0.74	2.07	46	0	0
40/60	0.83	1.87	51	1.14	1.25
30/70	0.88	1.16	82	1.66	1.82
20/80	0.91	0.91	104	2.13	2.36

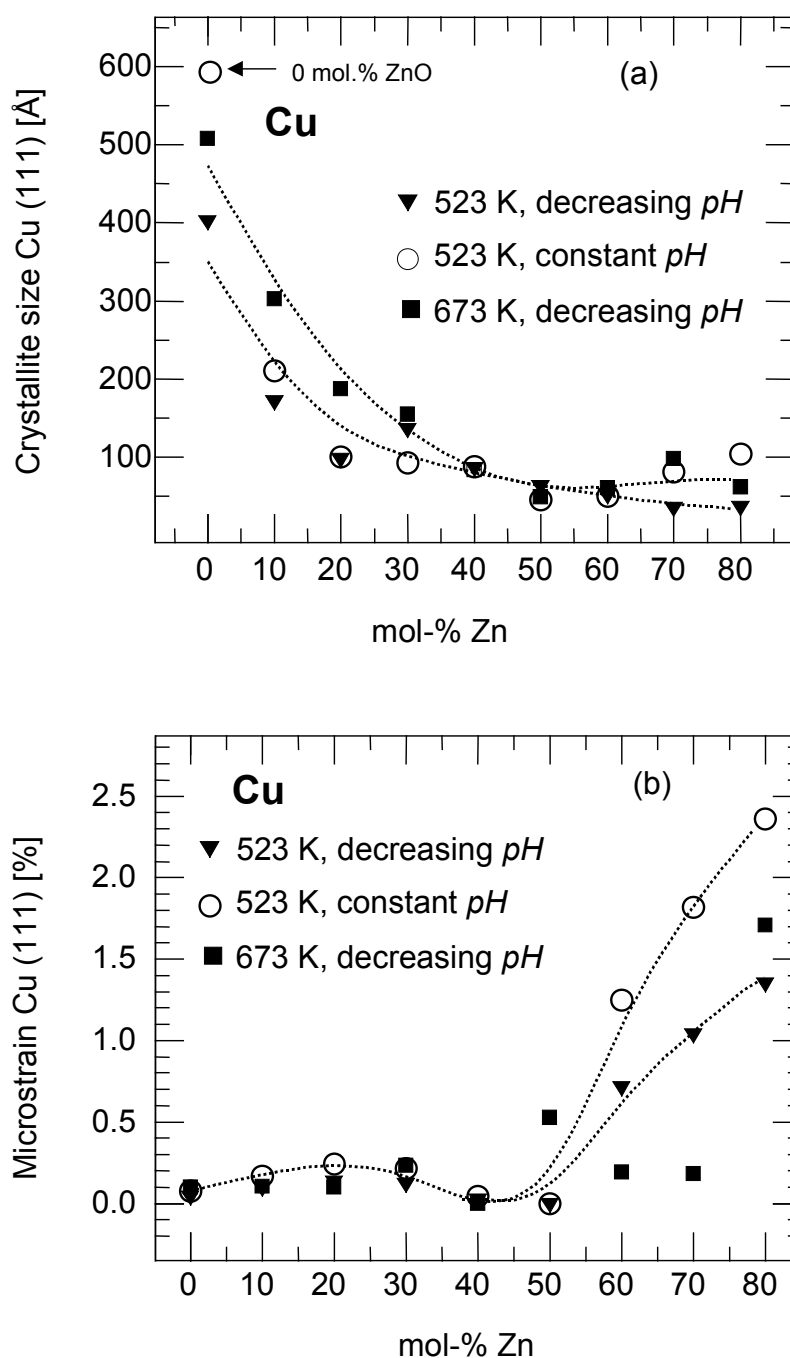


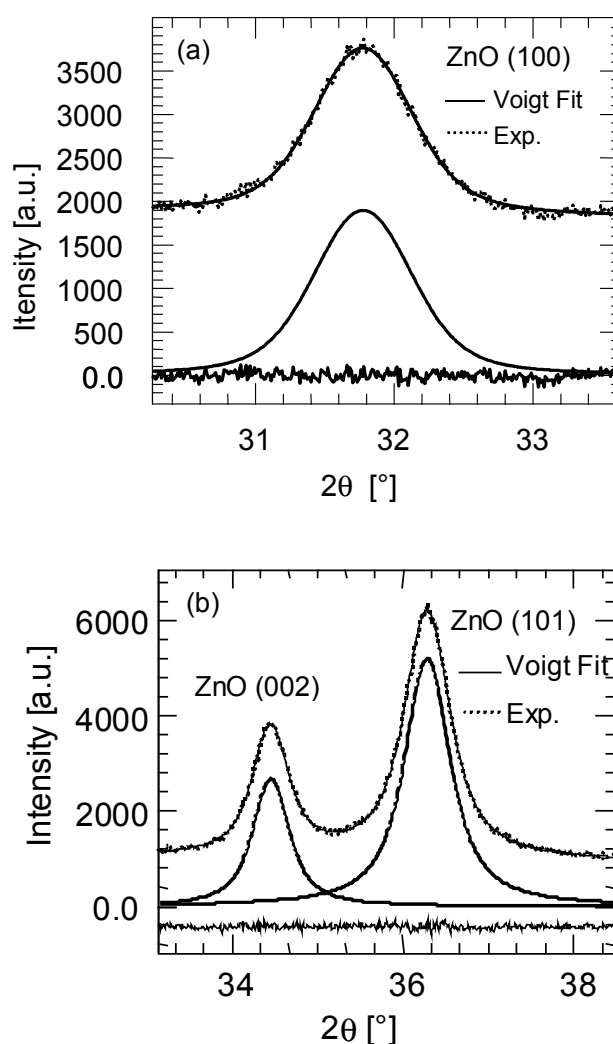
Figure 3.8: Copper crystallite size (a) and microstrain (b) determined according to the Voigt deconvolution procedure as a function of the nominal Zn-content of samples reduced in 5 vol-% H_2 at 523 K (decreasing and constant pH) and 673 K (decreasing pH). The data is based on the analysis of the copper (111) peak.

In Figure 3.8 the results of the analysis of the Cu (111) peak in terms of size (a) and strain (b) are shown for all sample series investigated. For all samples the Cu crystallite size is continuously decreasing with increasing Zn-content. The reduction at 673 K afforded larger crystallite sizes compared to those reduced at 523 K. For Zn-concentrations higher than 40 mol-% Zn only small differences in Cu crystallite size are detected (< 100 Å). For concentration < 50 mol-% Zn the Cu

microstrain exhibits only small strain contribution to the line broadening (Figure 3.8 (b)). For more diluted concentrations (50 - 80 mol-% Zn) an considerable increase in strain can be seen, whereas the samples prepared at constant pH expose higher strain values. The Cu strain for samples reduced at 673 K displays no systematic behavior in this compositional range, but mostly lower strain parameters are obtained.

3.2.4 Microstructural characterization of ZnO

In Figure 3.9 refined XRD peaks of ZnO are depicted for a sample with a Cu/Zn ratio of 40/60 (decreasing pH sample). The difference function displays no systematic deviation within experimental error indicating that the symmetric peak shape of the Voigt function is a good approximation to the experimental profile. The separation of two adjacent ZnO (002) and (101) peaks is displayed in Figure 3.9 (b).



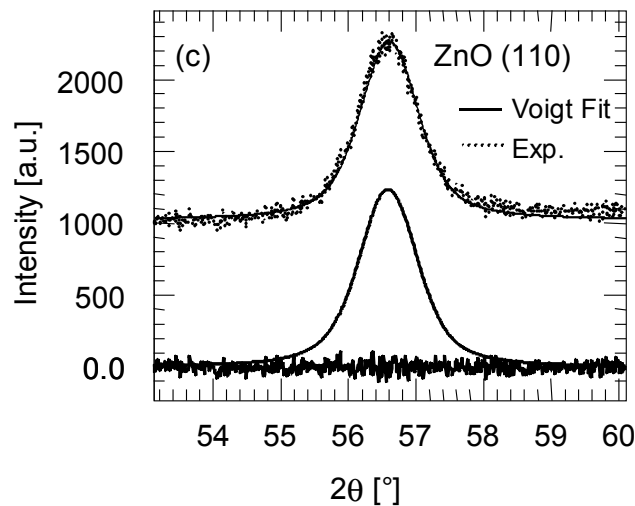


Figure 3.9: Experimental data and refined profile of ZnO (100), (002), (110) and (110) ((a)–(c)) reflection using the Voigt function. The difference plot, measured minus refined profile, is shown in the lower part of the graph (sample with 60 mol-%, decreasing pH reduced at 523 K).

The results (shape factor, deconvoluted integral Lorentzian and Gaussian breadth, crystallite size, and microstrain) derived from the line profile analysis of selected ZnO peaks of the constant pH sample series reduced at 523 K are summarized in Table 3.2. The shape parameter ϕ indicates that the Voigt function is a good approximation and applicable in all cases. With increasing Zn-concentration the Voigt profile fitting affords more Lorentzian contribution indicating that size effects become more prominent for line broadening.

In Figure 3.10 (a) the variation of the ZnO crystallite size based on the Lorentzian breadth of the (100) peak is shown as a function of the Zn-content in the samples for reduction at 523 K and 673 K. The ZnO sizes for samples reduced at 523 K exhibit a decreasing crystallite size with decreasing Zn-content (from 200 Å down to 100 Å) showing only small differences between both preparation methods (constant and decreasing pH). After reduction at 673 K the decreasing pH sample set exhibits a stronger dependence on the Zn-content with larger crystallite sizes (between ~ 450 Å and ~ 150 Å) than those obtained for samples after reduction at 523 K. A similar dependence on the reduction temperature is obtained for the ZnO microstrain (Figure 3.10 (b)). The ZnO microstrain was calculated from the Gaussian integral breadth of the deconvoluted Voigt function. Both sample sets which were reduced at 523 K (constant and decreasing pH) expose a slight decrease in strain with increasing Zn-content whereas only small differences in absolute microstrain are detected. After reduction at 673 K the strain has diminished to less than 50% as compared to the values obtained after low temperature reduction. In addition, no dependence of the microstrain on the Zn-content in the sample can be observed after high temperature reduction treatment. To further elucidate microstructural changes of ZnO for different crystallographic directions after reduction in hydrogen at 523 K and 673 K selected (*hkl*) reflections were analyzed.

Table 3.2: Integral breadth parameters and microstructural properties of ZnO based on XRD line profile analysis for various (hkl) reflections prepared at constant pH after treatment with H_2 at 523 K.

nominal Cu/Zn ratio [at.%]	reflection <i>hkl</i>	shape factor ϕ	deconvoluted integral Lorentzian breadth β_{fL} [° 2 θ]	crystallite size $\langle D \rangle_V$ [Å]	deconvoluted integral Gaussian breadth β_{fG} [° 2 θ]	microstrain $\tilde{\epsilon}$ [%]
80/20	100	0.89	0.53	173	0.74	1.1
	002	0.89	0.33	276	0.78	1.1
	110	0.85	0.85	188	0.53	0.69
70/30	100	0.81	0.77	120	0.77	1.2
	002	0.74	1.24	76	0.53	0.75
	110	0.82	1.12	90	0.78	0.63
60/40	100	0.78	0.90	101	0.62	0.95
	002	0.74	1.01	91	0.49	0.69
	110	0.81	1.05	95	0.84	0.68
50/50	100	0.79	0.65	141	0.66	1.02
	002	0.81	0.52	180	0.62	0.88
	110	0.83	0.88	114	0.75	0.61
40/60	100	0.78	0.86	106	0.64	0.99
	002	0.75	0.89	103	0.53	0.74
	110	0.82	1.03	98	0.81	0.65
30/70	100	0.82	0.71	128	0.53	0.82
	002	0.78	0.79	126	0.45	0.64
	110	0.79	0.94	106	0.66	0.94
20/80	100	0.77	0.64	143	0.49	0.75
	002	0.91	0.55	170	0.46	0.75
	110	0.78	0.88	114	0.54	0.44
10/90	100	0.77	0.50	183	0.44	0.68
	002	0.72	0.53	173	0.27	0.38
	110	0.80	0.72	140	0.56	0.46
0/100	100	0.70	0.45	204	0.39	0.61
	002	0.80	0.36	253	0.34	0.48
	110	0.80	0.52	195	0.50	0.40

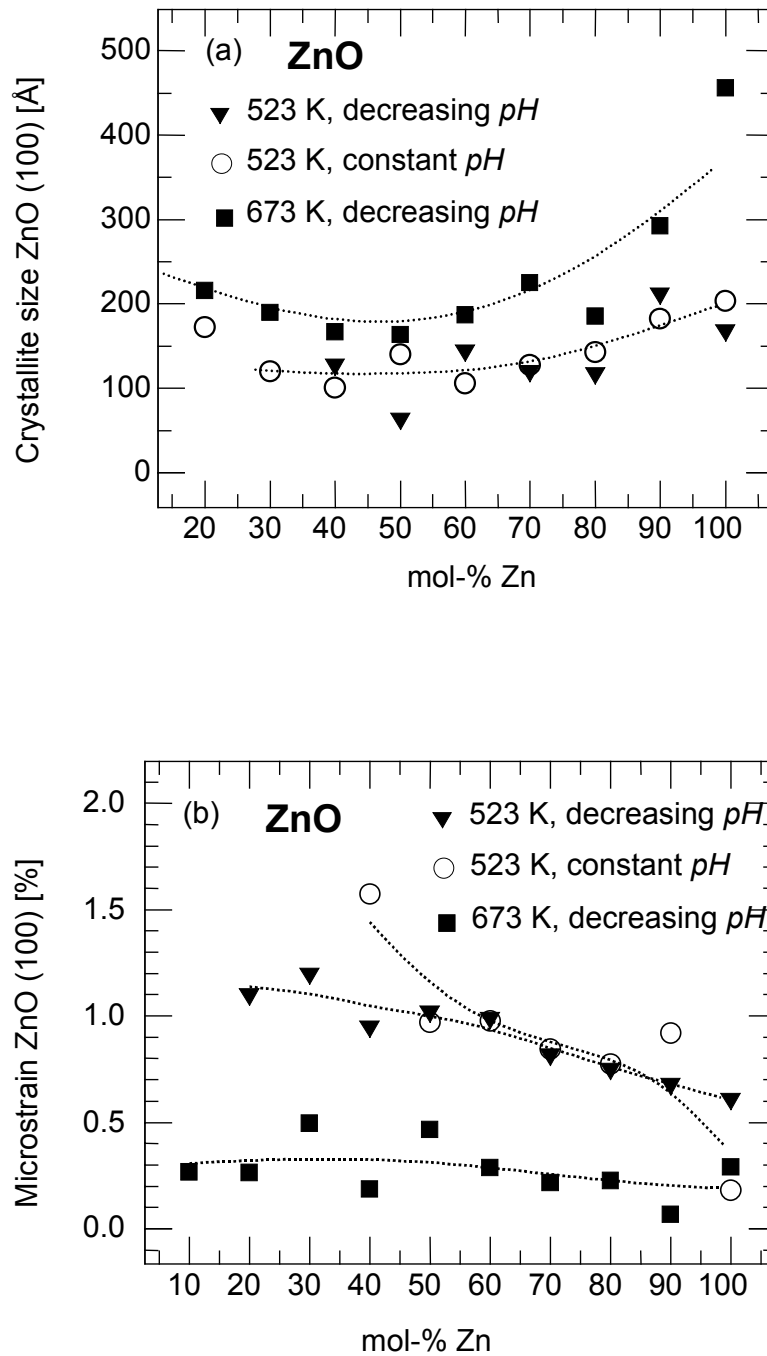


Figure 3.10: Zinc oxide crystallite size (a) and microstrain (b) determined according to the Voigt deconvolution procedure as a function of the nominal Zn-content for samples reduced in 5 vol-% H_2 at 523 K (decreasing and constant pH) and 673 K (decreasing pH). The data is based on the analysis of the zinc oxide (100) peak.

In Figure 3.11 (a) the ZnO crystallite size of the constant pH samples reduced at 523 K based on the (002), (100), and (110) are depicted as a function of the composition. It can be seen that with increasing ZnO concentration the crystallite sizes are increasing with no systematic difference in size for the different crystallographic directions. The large scatter of data is indicative of isotropic sizes for the different crystallographic directions. Contrary to the dependence of the ZnO crystallite size on the Zn-content the zinc oxide microstrain decreases with

increasing Zn content (Figure 3.11 b). Some differences in microstrain depending on the crystallographic direction can be observed. Apparently, the microstrain is anisotropic and highest values are measured mostly for the (100) reflection which ranges from 1.2 % at 30 mol-% Zn down to 0.7 % for pure ZnO.

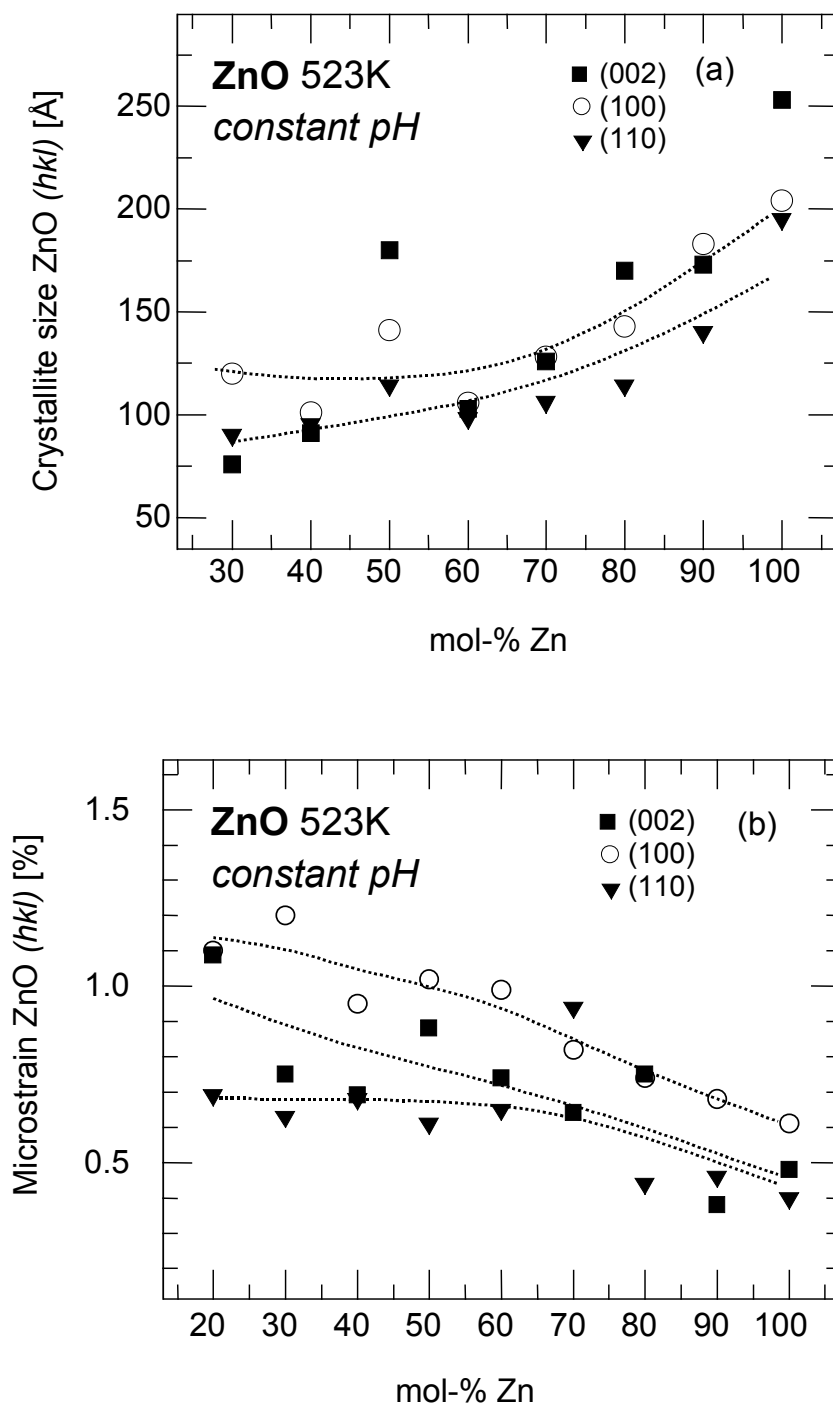
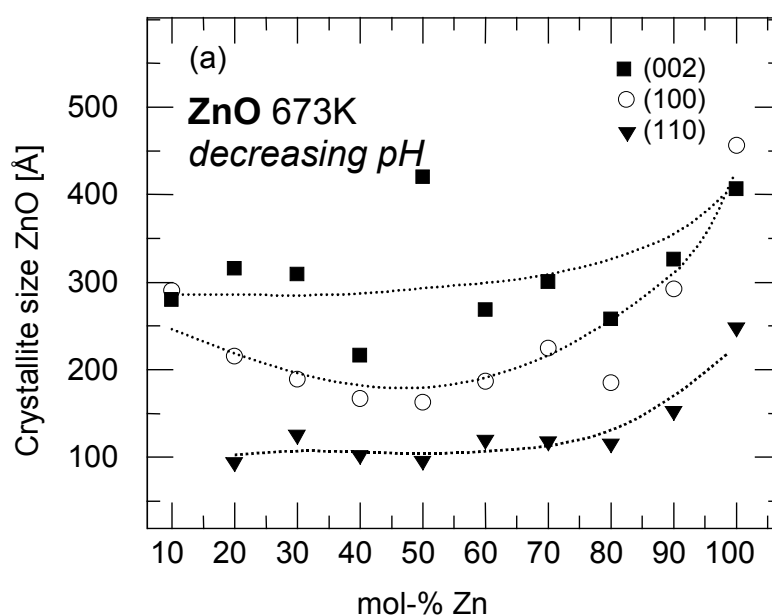


Figure 3.11: ZnO crystallite sizes (a) and microstrain (b) after reduction at 523 K as a function of the Zn-content (constant pH). The values are determined for different crystallographic directions based on the (100), (002) and (110) reflection.

The ZnO crystallite sizes based on selected (*hkl*) reflection after reduction at 673 K are shown in Figure 3.12 (a). After high temperature reduction the ZnO crystallite sizes display significant differences depending on the (*hkl*) reflection used for the size determination. The crystallite sizes based on the (002) reflection are on the average three times as large as those derived from the (110) reflection. In Figure 3.12 (b) the dependence of the ZnO microstrain after reduction at 673 K is shown as a function of the Zn-content (decreasing pH). The values are determined for the (100), (002) and (101) reflection. With decreasing Zn-content the microstrain is slightly increasing for the (100) reflection (from 0.3 % at 90 mol-% Zn up to 0.6 % at 10 mol-% Zn). The ZnO microstrain based on the (002) and (110) reflection shows only a weak dependence on the crystallographic direction. Moreover, the extent of strain has diminished by a factor of two after reduction at 623 K as compared to the values obtained for the samples reduced at 523 K.



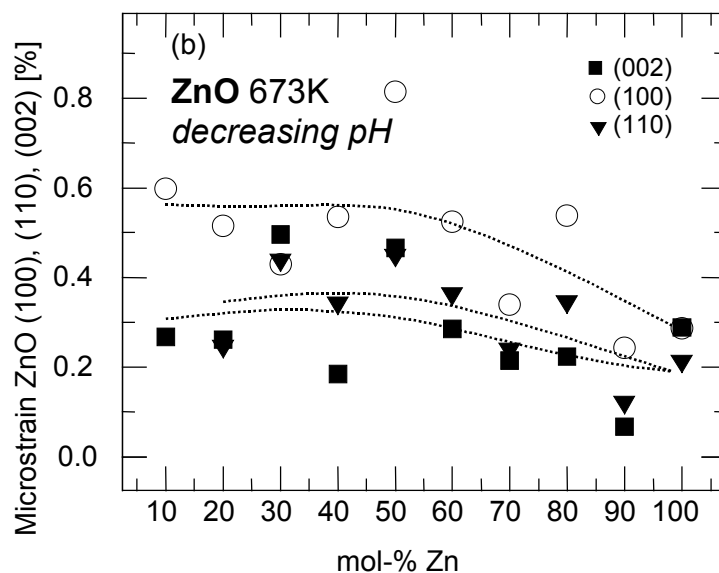


Figure 3.12: ZnO crystallite sizes (a) and microstrain (b) after reduction at 673 K as a function of the Zn-content (decreasing pH). The values are determined for different crystallographic directions based on the (100), (002) and (110) reflection.

3.2.5 Transmission electron microscopy of Cu/ZnO

For a selected commercial catalyst after reduction in hydrogen the morphology and the crystallographic orientation of the Cu and ZnO crystallites is investigated in detail by transmission electron microscopy.

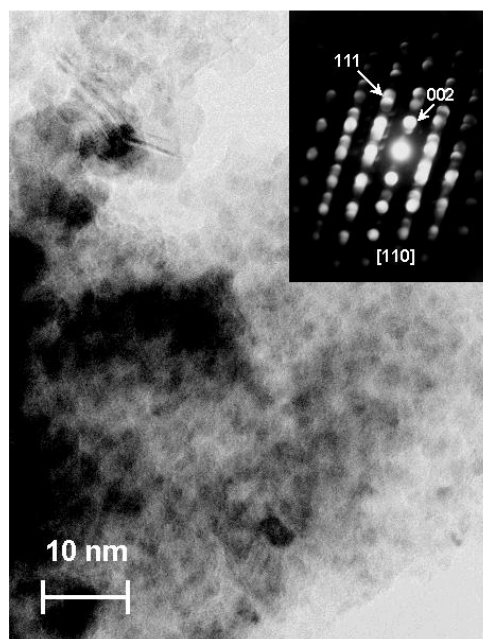


Figure 3.13: Transmission electron micrograph and convergent beam electron diffraction (inset) of a commercial catalyst reduced at 523 K.

The morphology of a reduced commercial Cu/Zn-catalyst particle is given in a TEM image shown in Figure 3.13. Spherically shaped particles are evidenced by the dark contrast ranging from 40 to 70 Å in diameter. The inset given in Figure 3.13 depicts a convergent electron beam diffraction pattern which was obtained of the same area. The diffraction pattern exhibits diffraction spot characteristic of *fcc* copper along the [110] zone axis. Furthermore, the double appearance of the spots indicates twinning of the Cu crystallite, which can be related to the line defect in the micrograph detectable in the upper left-hand corner. No diffraction spots belonging to ZnO can be detected which implies that for the particle investigated the ZnO support was either not favorably oriented to the electron beam for diffraction or of amorphous nature.

In Figure 3.14 a selected area electron diffraction pattern and the corresponding bright and dark field images of a reduced commercial catalyst are shown. The diffraction pattern with sharp diffraction spots indicates that catalyst particle investigated consists of single crystalline parts. In the bright-field image a large particle is shown which is built up by a network of interconnected finely dispersed crystallites with sizes well below 100 Å. This further implies that the single crystallites are not randomly oriented to each other but rather obtain a preferred orientation. Using dark field image technique the particles belonging to the Cu and ZnO phase can be distinguished. Furthermore, this technique gives an estimate about the size and the spatial distribution of the individual crystallites. The dark field image from the Cu (111) spot gives the dispersion of the Cu microcrystallites supported on the ZnO crystallites. The copper particles size ranges from 30 – 70 Å. However, only a small fraction of the Cu crystallites give rise to bright spots (Figure 3.14 (b 3)) whereas the bright areas in the dark field image resulting from the ZnO (010) and (100) diffraction spot (Figure 3.14 (b 1-2)) are much more widespread. For the ZnO similar crystallite sizes can be observed. The electron diffraction patterns reveal further microstructural relationships within the composite particle investigated. A mutual parallel crystal orientation relationship can be seen between the ZnO support and the Cu clusters by the coincidence of the reflections along certain crystallographic directions. Indexing of the pattern affords that the ZnO phase is in crystallographic registry to the metallic copper phase. The spot pattern from an (110) orientation of Cu is superimposed to an (001) orientation of ZnO. This indicates that the Cu (110) and the ZnO (001) planes are parallel while the Cu zone axes are [100] is parallel to ZnO [210] axis.

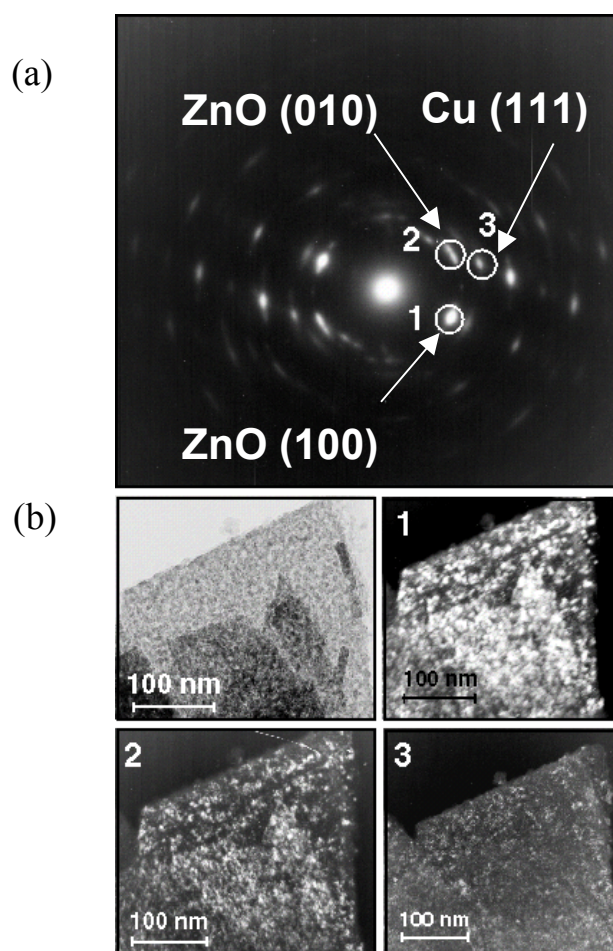


Figure 3.14: Selected area electron diffraction pattern from a reduced catalyst reduced in 5 vol-% H_2 at 523 K (a); corresponding bright field image and dark field of image of the ZnO phase using the (100) and (010) diffraction spot ((b) 1,2); dark field image of the Cu phase using the Cu (111) reflection ((b) 3).

This approach gives evidence that there exists a orientation relationship between the Cu and ZnO phase for this particular sample. However, it can be assumed that more possible parallelism exist between the Cu and ZnO planes that are not observed. It appears that the epitaxial interface interaction of both phase is a characteristic property of the Cu/ZnO system. Based on the epitaxial orientation between the ZnO phase and the reduced copper phase the following schematic structural arrangement can be proposed to describe the Cu/ZnO interface (Figure 3.15). It is assumed, that the interface interaction of both phase is of high importance for the structural interaction of the Cu and ZnO phase. Considering the detected microstrain in the reduced Cu and ZnO crystallites it appears that the Cu/ZnO interface is the main reason for the structural disorder observed. At the incoherent interface the lattice mismatch of the adjacent lattice planes can induce *e.g.* lattice expansion and/or contraction that can cause microstrain effects.

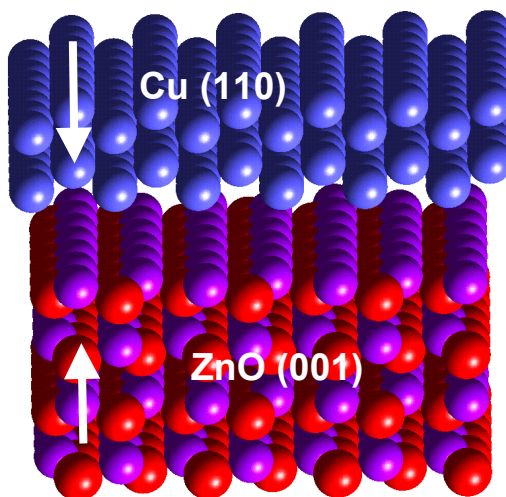


Figure 3.15: Schematic representation of crystallographic orientation at the Cu/ZnO interface of a reduced catalyst showing

3.2.6 Discussion

3.2.6.1 Dependence of microstructure on preparation and reduction treatment

The reduction of CuO/ZnO with 5 % H₂ at 523 K and 673 K afforded completely reduced metallic copper with no copper oxide phases detectable by XRD (lower detection limit ~ 5 %). The line broadening analysis according to the Voigt method was applicable in all cases to separate line broadening effects for different reflection lines of ZnO and Cu in terms of size and strain. The mutual structural interaction of both constituents in binary Cu/ZnO is clearly shown by the dependence of size and strain effects on the concentration of Zn in the sample (Figure 3.8, 3.9, and 3.10). The line profile analysis afforded a decrease of the Cu crystallite sizes as a function of the Zn content whereas the microstrain increased with increasing Zn content. For the ZnO crystallites a similar dependence on the Cu content is detectable. The microstrain measured for ZnO reduced at 523 K exhibits a monotonous increase in strain with increasing Cu content for both sample sets (Figure 3.11 b). The thermal treatment during reduction at 673 K is sufficient to cause a release in microstrain for ZnO that amounts to ~ 50% with respect to the strain measured after reduction 523 K.

The reduction treatment at 673 K gives evidence that the reduction temperature has an influence on both the crystallite size and the microstrain of Cu and ZnO. After reduction at 523 K the ZnO crystallite sizes are almost isotropic with mean diameters ranging between 75 and 250 Å.

The XRD profile analysis results obtained for the ZnO microstrain at 673 K indicate that the

strain is dependent on the reduction temperature. Apparently, a higher reduction temperature induces annealing processes of the defects that lead to the lattice distortions. This process is accompanied with an increasing ZnO crystallite size which is a consequence of sintering of the ZnO particles (see Figure 3.12 (b)). Thus, the total area of the phases boundaries between ZnO and Cu is reduced leading to a decrease of the microstrain in the ZnO matrix.

In addition, an anisotropy of the domain sizes for ZnO was detected based on a single line analysis applied to the (002), (100) and (110) reflections representative for different crystallographic directions after reduction at 673 K (see Figure 3.12). With regard to the ZnO-crystallite sizes obtained after reduction at 523 K which appeared to be equiaxed, the crystallite growth proceeded preferentially along the hexagonal basal plane. Assuming a cylindrical crystallite shape with the long axis along the *c* – axis the height is given by the size parameter of the reflection for the (002) peak whereas the perpendicular plane (100) describes the thickness of the cylinder. The ratio of both crystallite sizes is described by an aspect ratio (*i.e.* diameter/height $\sim D_{\text{ZnO}(100)} / D_{\text{ZnO}(002)}$).

Comparing our results to data of ZnO crystallite morphology based on different precursors of pure ZnO precursor compounds (*e.g.* hydroxide nitrate, oxalate, and hydroxide carbonate) by Audebrand *et. al* [Audebrand98] differences in the aspect ratio can be found. Those authors observed a constant aspect ratio of ZnO nanodomains with the diameter slightly larger than the height. Our results, however, point to a different aspect ratio of the ZnO crystallites except for the pure ZnO sample. After hydrogen reduction the crystallite size determined from the (002) reflection is always larger than the size derived from the (100) peak. Only for the pure ZnO sample (sample D100/0) the reversed sizes are observed (see Figure 3.12 (a)). Consequently, this indicates that the crystallite shape of ZnO is influenced by the presence of the Cu-phase resulting in a crystallite shape anisotropy due to a preferential growth along the *c*-axis after reduction at 673 K.

In addition, the non uniform distribution of microstrain for different crystallographic orientations may be associated with stress fields that build up due to distortions in the zinc oxide lattice. Those distortions might be caused by the interface interaction of the reduced copper clusters with the ZnO support which are most probably in epitaxial orientation to each other as shown by TEM. Further possible explanation for the occurrence of strain in ZnO includes the formation of misfit dislocation due to interface interaction of ZnO with the adjacent Cu-phase. Especially for low copper concentration an epitaxial orientation of flat Cu particles onto the ZnO lattice was previously reported by [Herman80]. Former investigation by Warren reported on the

broadening influence of stacking faults on the XRD line profile which are a common defect in hexagonal close-packed material [Warren69]. It was shown that only certain orders of reflection are affected by faulting effect (for hkl with $h-k = 3n \pm 1$). However, those reflections were not taken into account for the line profile refinement. Therefore, no assumptions concerning this common type of defect in ZnO can be made on the basis of XRD line broadening. The relieve of strain upon reduction at higher temperatures together with crystallite growth (Figure 3.12 a + b) of ZnO is indicative of sintering processes (increase in ZnO crystallite size) together with an annealing of structural defects (*i.e.* decrease in microstrain). This might be associated with a destruction of the Cu/ZnO interface and a loss of the structural interaction of both phases.

In summary the XRD line profile analysis affords reasonable results for size and strain effects using a large number of samples. The investigation of a series samples enabled to establish general trends of microstructural properties. Hence, it was possible to determine relative changes of size and strain parameters as a function of the Cu/Zn-ratio and the pH during preparation. It is not intended to determine microstructural parameters on an absolute scale but rather to compare relative values by using a large set of samples. A disadvantage of the size determination is that it affords crystallite sizes that are volume weighted without any more specific information concerning the distribution of the crystallite sizes.

3.2.6.2 *Microstructure and Catalysis*

On the basis of recently published literature [Kampshoff94], [Mavrikakis98] we envisioned that the detected microstructural bulk defects of in Cu and ZnO can have an impact on the catalytic activity. Those bulk defects terminate at the surface of the crystallite where they can introduce various forms of defect (*e.g.* terraces and kinks) that modify the surface properties. In contrast to the prevailing opinion in the literature [Burch90], [Spencer99] the microstructural analysis by XRD gives evidence that the role of ZnO has to be redefined in the sense that it is not an inert support under typical operation conditions (*e.g.* temperature). Previous investigation attributed the active phase exclusively to metallic copper and therefore sintering of the Cu crystallites was considered as the main reason for the loss of activity. However, it remains open at this stage if the defect structure of ZnO directly influences the catalytic activity or if it serves in maintaining certain copper sites. This question will be further addressed in chapter 5, in which the results of a combined *in situ* XRD and XAS approach together with catalytic data is presented.

Presently, there are different models of the microstructure of Cu-Zn catalysts discussed to

explain the enhanced catalytic activity by the promotional effect of ZnO in methanol synthesis. In the model developed by *Klier* the formation of solid solution of copper in ZnO with a upper limit in solubility with 15 mol-% up to Cu/Zn ratios 30/70 was regarded responsible [Dominiquez83]. The subsequent formation of solute Cu^+ in ZnO upon reduction is regarded as one kind of active site. However, for higher copper concentration (90 mol-% Cu) we have shown on the basis of EXAFS measurements of CuO/ZnO precursors (see chapter 3.1) that ZnO is incorporated in the CuO lattice. Therefore, the observed copper microstrain at lower concentration ZnO (< 30 mol-% Zn) might also be caused by the incorporation of Zn in the Cu-lattice which can be preserved .

In summary, in this chapter the copper microstrain was proven to be an additional bulk property beside the copper surface area that varies with composition.

3.3 Conclusion

For the calcined precursor samples a dependence of the CuO and ZnO crystallite sizes on the composition was detected. Although monophasic CuO-ZnO solid solutions are only known in the case of high temperature preparation (*e.g.* 0.7 mol-% Cu at 1173 K [Stirling]) the dissolution of higher amounts of CuO in ZnO (~ 5 mol-%) for high Cu content Cu/ZnO catalysts on the basis of extended X-ray absorption spectroscopy (EXAFS) investigation was detected. Therefore, the formation of Cu-Zn bulk alloys was assumed to be enabled under typical reduction temperatures at 523 K.

Furthermore, for reduced Cu/ZnO catalyst with varying molar ratios (90/10 through 10/90) the single line profile analysis based on the Voigt has been applied to determine the crystallite size and microstrain. This XRD line profile analysis is especially useful for the investigation of polyphasic catalyst materials where higher orders of reflection are not accessible for an analysis. This analysis procedure was successfully performed on the Cu/ZnO catalyst system for a large number of samples prepared at neutral and decreasing pH with different Cu/Zn ratios. The CuO/ZnO samples were reduced with 5 vol-% H_2 at 523 K and 673 K prior to the XRD investigation. For copper metal and zinc oxide a separation of size and strain broadening effects could be performed. Both, the crystallite size and the microstrain in Cu and ZnO are dependent on the composition and the reduction temperature. According to the results it seems that the pH during preparation has only a small effect on the microstructure for a given reduction temperature. Hydrogen reduction at 673 K leads to a pronounced sintering of the ZnO particles with respect to reduction temperatures at 523 K. The Cu crystallites showed only a minor sintering tendency especially at higher ZnO concentrations. For the reduced Cu clusters no indications of a size

anisotropy can be found which supports the assumption of spherical copper particles. This is a reasonable assumption concerning the morphology for this crystallite size regime of the Cu particles (100 – 200 Å) investigated, in which a plate- or needle like shape is unlikely to occur. However, morphological changes (wetting/non-wetting phenomenon) of copper clusters upon changing the reduction potential in the gaseous environment were reported by Clausen *et al.* [Ovesen97]. Those Cu particles refer to Cu/ZnO systems with very low Cu concentration (~5% Cu) and smaller cluster size (< 30 Å). This crystallite size is not accessible by XRD techniques and an indication of texture effects due to morphological changes is not feasible. It can be argued that these small clusters might not represent the industrially important system. However, using surface science data on Cu single-crystal surfaces Nørskov and coworkers [Rasmussen94] formulated a microkinetic model for the methanol synthesis reaction. Incorporating dynamical morphological changes considering differences in surface area and the higher activity of Cu(110) and Cu(100) compared to Cu(111) planes a much better description of the measured rates could be provided by Clausen and coworkers [Ovesen97].

A dimensional anisotropy of the ZnO crystallite shape was observed with the crystallite growth occurring preferentially along the [001] direction. In addition, the reduction at 623 K afforded a strain release in the ZnO matrix whereas for copper crystallites only minor differences in microstrain are detectable. For the occurrence of strain effects compositional inhomogeneities, the formation of solid solutions of Cu in Zn and interfacial interaction were considered to be the main reason. The application of transmission electron microscopy for a reduced industrial catalyst gave evidence for an epitaxial crystallographic orientation of the Cu and ZnO planes at the interface. The close interfacial interaction of Cu/ZnO is regarded as a main factor for the observed structural disorder due to an incoherent interface (*i.e.* lattice mismatch).

Furthermore, the results provide evidence that the hydroxycarbonate precursor phases indeed have an effect on the microstructural properties of the reduced samples. Taking the results for the EXAFS characterization of CuO/ZnO precursors into account it was shown that the discontinuous behavior of the Cu/ZnO microstructure *i.e.* the increase of the Cu microstrain and the ZnO particle size is directly influenced by a change in the phase composition of the hydroxycarbonate precursor.

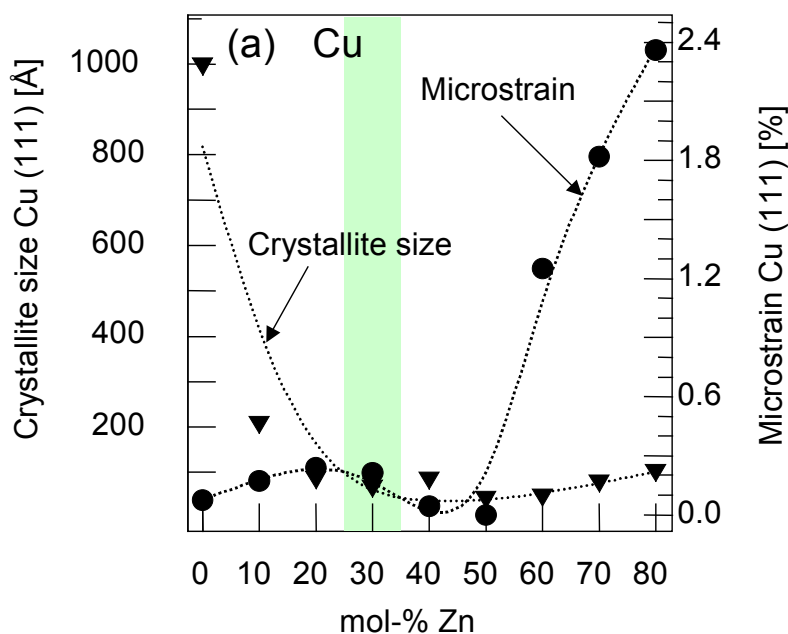
4 Implication of Cu microstructure for methanol synthesis activity

4.1 Introduction

In this chapter a correlation between the defective bulk structure of copper and the methanol synthesis activity of Cu/ZnO catalysts will be revealed. Therefore, the composition of the Cu/ZnO catalyst is systematically varied in order to detect a corresponding variation of the catalytic performance. The microstructural data of the bulk structure of copper in terms of size and strain afforded in chapter 3 is utilized for this correlation. The methanol synthesis activity data was obtained in screening experiments at atmospheric pressure performed in a collaborative effort with the Ruhr-Universität-Bochum. For the investigation presented emphasis is put on those systems that are of industrial interest (~ 70 mol-% Cu).

4.2 Microstructural characteristics revealed by X-ray diffraction line profile analysis

First, the essential microstructural bulk parameters results for the line-profile analysis for the constant pH sample series are briefly summarized.



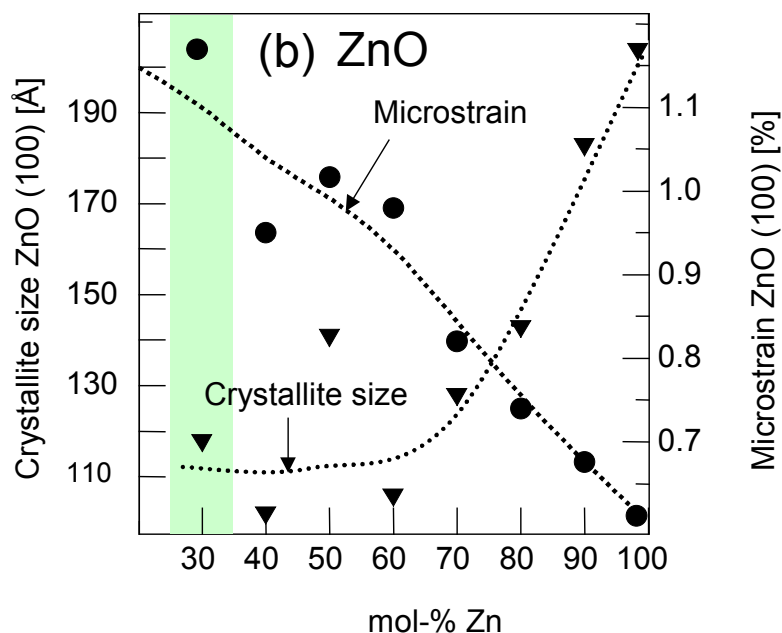


Figure 4.1: Variation of crystallite size and microstrain of copper (a) and zinc oxide (b) as a function of the nominal composition after reduction at 523 K in 5 vol-% H_2 in He. The data are based on the analysis of the copper (111) peak and the ZnO (100) peak. Composition of interest for industrial application is shown in the shaded area.

The results of a detailed Cu (111) and ZnO (100) line profile analysis using a Voigt function are shown in Figure 4.1 (a) and (b), respectively. Both graphs show a conspicuous dependence of Cu and ZnO size and strain on the nominal composition of the samples. For both Cu and ZnO an increase in strain with decreasing crystallite size can be seen. The calculated strain in copper rich samples (< 60 mol-% Zn) is small, but a considerable increase in strain can be observed for more diluted samples (60 – 80 mol-% Zn). The crystallite size of Cu shows a continuous decrease from ~ 1000 Å down to < 100 Å from pure Cu to 20 mol-% Zn and then remains relatively constant through 80 mol-% Zn. For ZnO a monotonous increase in strain with increasing Cu content was obtained. With an increasing Cu loading, ZnO exhibits a decrease in crystallite size (from 200 Å for pure ZnO down to 120 Å for a sample with 60 mol-% Zn). Apparently, the ZnO crystallite growth is retarded by the presence of copper in the samples.

In Figure 4.2 the refined Cu lattice constant a (fcc, $Fm\bar{3}m$, $a = 3.6150$ Å [Swanson53]) is depicted with increasing Zn content. Already at a Zn content of 10 mol-% a considerable lattice expansion ($\Delta a_{Cu}/a_{0,Cu} \sim 0.14\%$) can be observed. In the range from 90/10 to 40/60 the Cu lattice constant does not change significantly, whereas at Zn concentrations of 70% and 80% mol-% a strong lattice expansion is obtained ($\Delta a_{Cu}/a_{0,Cu} \sim 0.35\%$).

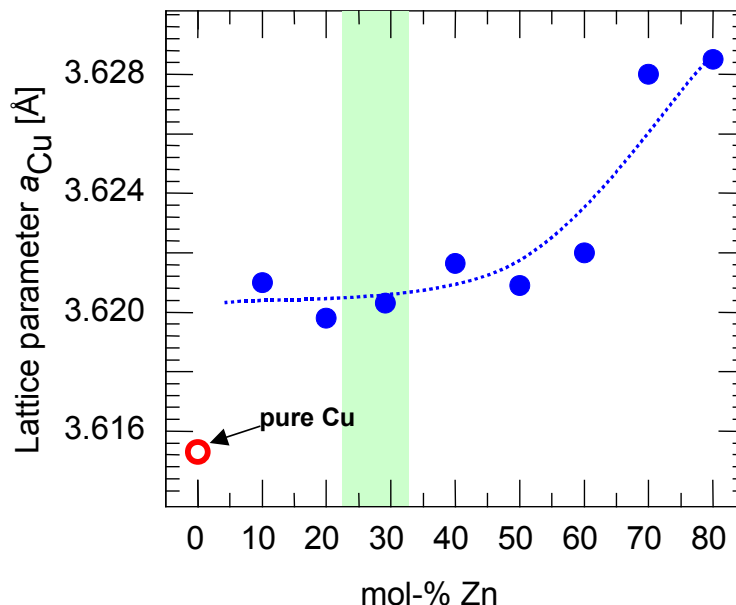


Figure 4.2: Variation of the Cu lattice parameter a with Zn content after reduction in 2 vol.-% hydrogen at 523 K (measured at RT). Composition of interest for industrial application is shown in shaded area.

4.2.1 Copper surface area measurements

Figure 4.3 shows the dependence of the specific copper surface area, determined by N_2O RFC ($S_{Cu(N_2O)}$) or estimated using the crystallite size determined by XRD ($S_{Cu(XRD)}$), on Zn concentration. It can be seen that the “XRD surface areas” $S_{Cu(XRD)}$ on the average are higher than the $S_{Cu(N_2O)}$ values. This difference may originate from a small degree of agglomeration of copper particles or support interactions which reduce the accessible Cu surface area. In addition, a varying Cu particle size distribution could result in differences in surface areas.

The deviation of $S_{Cu(XRD)}$ from $S_{Cu(N_2O)}$ appears to be more pronounced in the intermediate composition range. However, in total, both surface areas are in good agreement, which underlines the applicability of the XRD surface area calculation. Hence, the reliable copper surface area based on N_2O RFC and the nominal Cu content of the sample permits to calculate the ratio of copper surface atoms to those in the bulk in order to obtain an estimation of the Cu dispersion.

Figure 4.4 shows an increase of dispersion of copper atoms in terms of $N_{surface\ atoms(N_2O)} / N_{bulk\ atoms}$ with increasing Zn concentration reaching a maximum at a composition of 70 mol-% Zn.

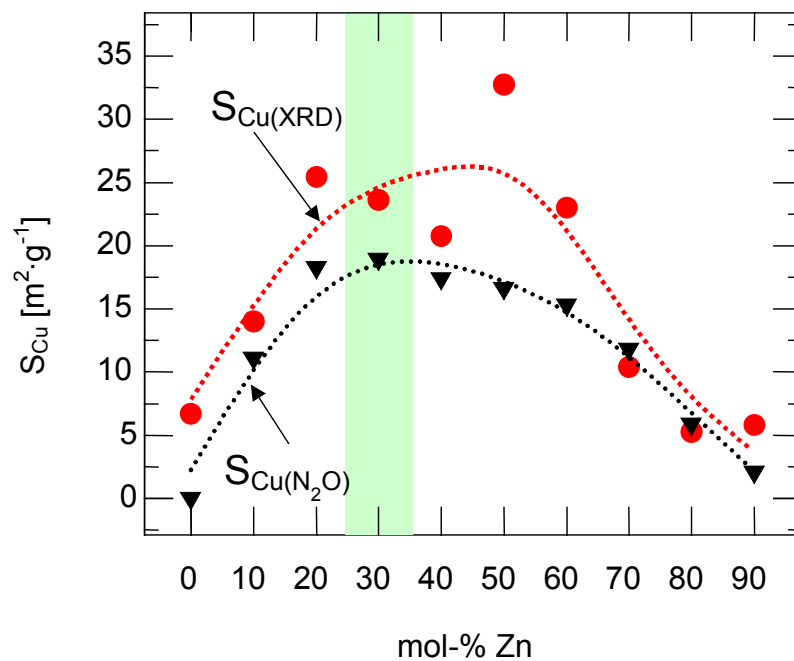


Figure 4.3: Copper surface area as a function of the nominal composition. Values are determined either by N_2O RFC ($S_{Cu(N_2O)}$) or estimated using the crystallite size determined by XRD ($S_{Cu(XRD)}$). Composition of interest for industrial application is shown in the shaded area.

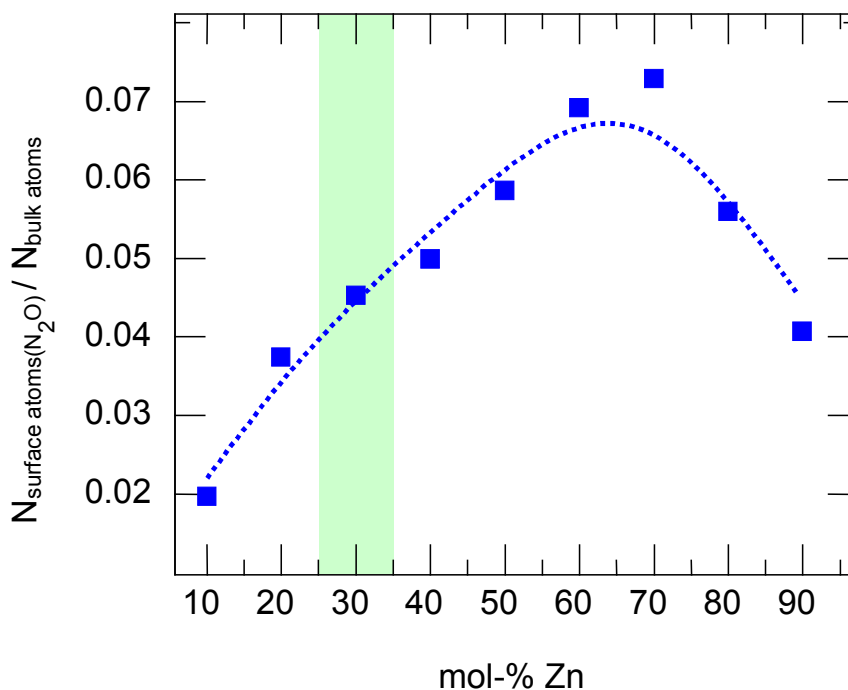


Figure 4.4: Ratio of copper surface atoms determined by N_2O RFC to bulk atoms from XRD crystallite size assuming a spherical shape as a function of the Zn content. Composition of interest for industrial application is shown in the shaded area.

4.2.2 Catalytic activity screening

In agreement with previous investigations [Chinchen86] the methanol synthesis activity of the Cu/ZnO samples studied proved to be strongly dependent on the nominal composition. The methanol production rate as a function of composition shows a volcano type behavior as depicted in Figure 4.5. The maximum in normalized production rate is obtained for the sample with a composition of Cu/Zn = 80/20, in good agreement with previous publications [Rasmussen87].

An approximately linear dependence of the normalized methanol production rate on the specific Cu surface area is obtained (Figure 4.6) which is in agreement with result by Joyner *et al.* [Joyner90], [Burch90b].

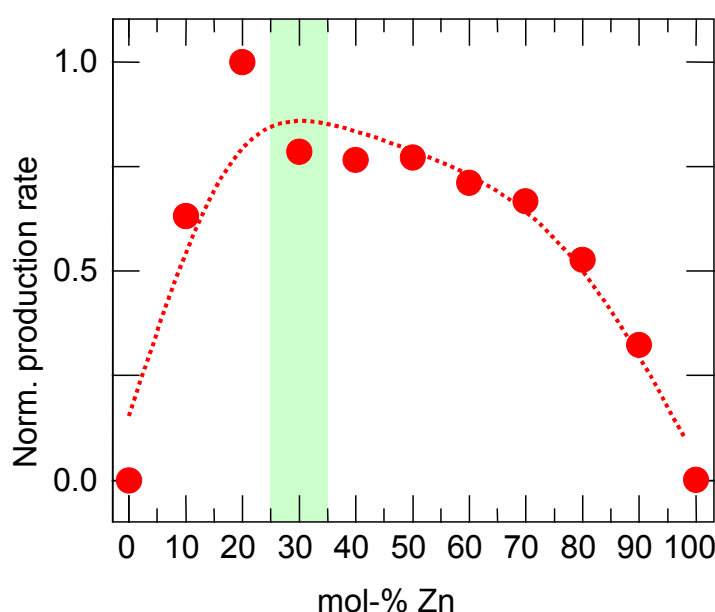


Figure 4.5: Normalized production rate of methanol with increasing Zn concentration. The reaction was carried out at 493 K under atmospheric pressure with a feed gas composition of 10% CO, 4% CO₂, 72% H₂ in He.

This would imply a constant TOF independent on the composition with no other structural parameters influencing the catalytic activity. In order to clarify if in addition to the Cu surface area other structural parameters affect the methanol synthesis activity of the samples studied, the normalized turn-over frequency as a function of the Zn content is shown in Figure 4.7.

Evidently, deviations from the supposedly constant TOF with increasing Zn content exist. A minimum in normalized TOF is observed for those samples that exhibit basically no microstructural strain according to Figure 4.1 a. For higher Zn contents (> 70 mol-% Zn) a considerable increase in TOF can be seen, indicating that other parameters in addition to the Cu surface area determine the methanol synthesis activity.

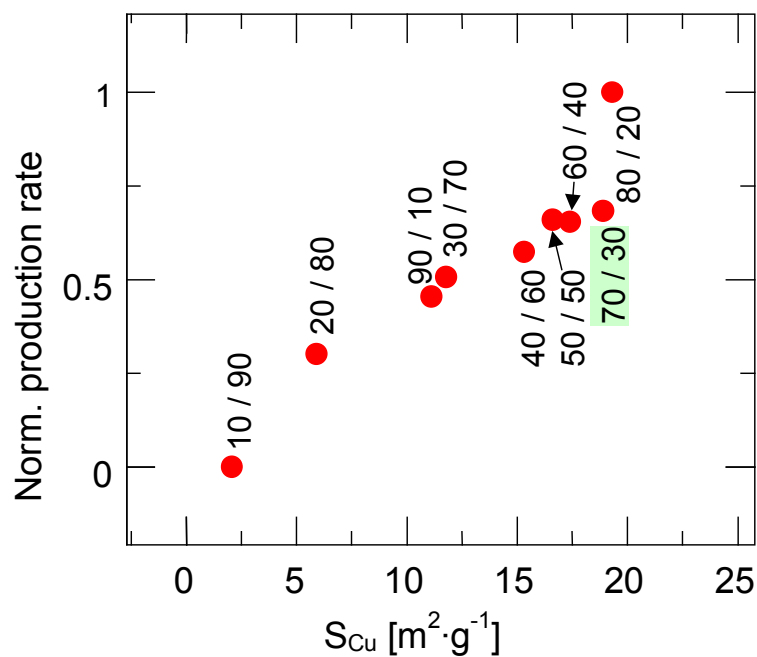


Figure 4.6: Normalized methanol production rate as a function of copper metal surface area. Composition of interest for industrial application is shown in the shaded area.

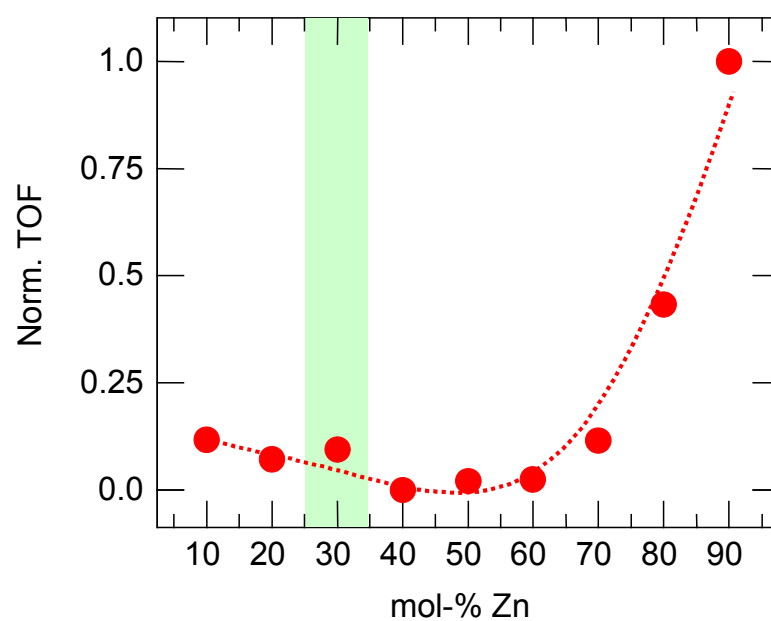


Figure 4.7: Normalized turn-over frequency (TOF) for methanol production as a function of Zn content. Composition of interest for industrial application is shown in the shaded area.

4.2.3 Impact of Cu microstrain on Turn-over-frequency

The normalized TOF for methanol production as a function of the copper lattice strain is displayed in Figure 4.8.

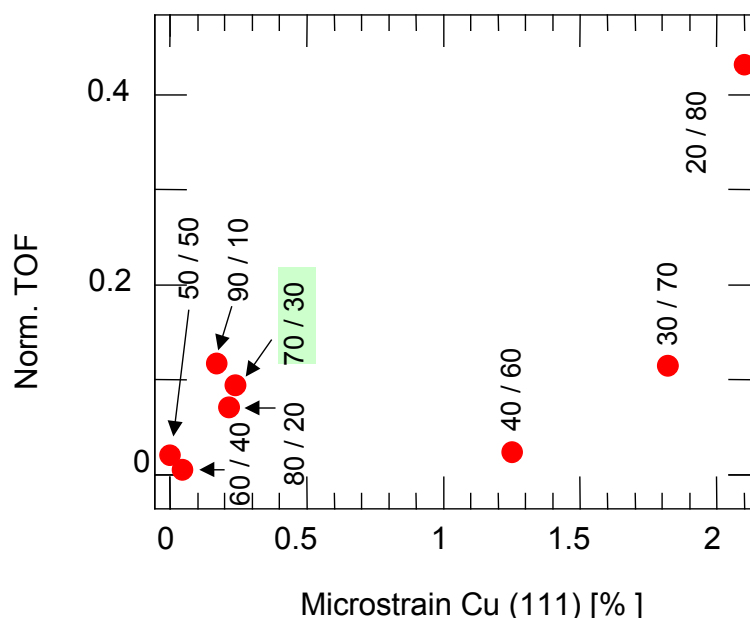


Figure 4.8: Normalized turn-over frequency (TOF) for methanol production as a function of the Cu microstrain derived for the Cu (111) peak.

Evidently, the TOF for methanol production on the Cu/ZnO systems studied exhibits a positive correlation with the microstrain in the Cu crystallites. Hence, a higher turn-over frequency is attained for strained copper particles. It appears that a high specific Cu surface area is a necessary prerequisite for an active Cu/ZnO catalyst but that other microstructural parameters also affect methanol synthesis activity. However, for moderately strained copper particles (microstrain $< 0.5\%$) a spread in TOF for various samples can be seen. This can originate from other factors that can also influence the activity (*e.g.* different precursor phases and Zn contamination in the Cu particles).

A correlation of the TOF for methanol production with the degree of dispersion estimated from the $S_{\text{Cu}(\text{N}_2\text{O})}$ surface area (Figure 4.4) is depicted in Figure 4.9 (a). It can be seen that the TOF cannot unequivocally be correlated to the degree of dispersion. Interestingly, two groups of samples can be observed. One group (A in Figure 4.9 a) shows a constant TOF independent on the degree of dispersion, whereas the other group (B in Figure 4.9(a)) exhibits a decreasing TOF with increasing dispersion. The behavior of the group B samples can be ascribed to the increased

contribution of the Cu strain in these systems which is enhanced by a slight increase in crystallite size for more diluted samples (*e.g.* sample 10/90). While maintaining a similar crystallite size as that of the 30 mol-% Zn the more diluted and strained samples expose a more active surface for methanol synthesis. In contrast, the group A samples exhibit no significant strain contributions. Furthermore, it can be seen that Cu/ZnO samples that are of interest for industrial applications (< 60 mol-% Zn) do not possess the most highly dispersed crystallites as it has been claimed in the literature with respect to *e.g.* the dynamic spreading behavior of Cu on ZnO [Ovesen97].

The correlation of TOF and Cu lattice strain presented in this work indicates that a combination of Cu surface area and Cu and ZnO microstructural strain determines the methanol synthesis activity of Cu/ZnO catalysts. Our results substantiate the assumption of Topsøe and Topsøe [Topsøe99] that strain would be one possible explanation for the strong CO band shift which was previously observed with FTIR by Kampshoff *et al.* [Kampshoff94]. The origin of the microstrain observed can be explained by (I) an certain fraction of the minority phase dissolved in the bulk of the majority phase (*e.g.* ZnO in Cu), or (II) incomplete reduction and hence residual oxygen in the Cu matrix, (III) interfacial strain caused by epitaxial bonding of Cu on ZnO. Increased CO adsorption energies on strained surfaces have been predicted on the basis of self-consistent density functional calculations in ref. [Mavrikakis98]. The model described therein could, in principle, be extended to the adsorption properties of hydrogen on metal surfaces. The underlying model assumes that the surface chemisorption properties and the reactivity of metals are affected by a strain induced shift in the center of the metal *d* bands. Although the authors report on a linear variation of adsorption energies of different molecules (*e.g.* CO and O) with the surface strain the non-linear dependence of the TOF (onset in TOF at 2% strain) on the copper microstrain observed in Figure 4.8 might be caused by additional external factors influencing the activity on a macroscopic scale (*e.g.* temperature, flow rates).

In Figure 4.9 (b) the normalized TOF for methanol production is shown as a function of the Cu lattice parameter *a*. Only the sample 20/80 shows a significant increase in the TOF with expansion of the Cu lattice. In a previous publication, Fujitani and Nakamura [Fujitani98] have assigned the observed increase in Cu lattice parameter to a Cu-Zn alloy formation and, hence, have identified this alloy phase as being responsible for an increasing methanol production activity. Compared to the Cu lattice parameter of monophasic α -brass [Rao63] the lattice expansion obtained corresponds to 5 mol-% Zn dissolved in Cu. The amount of Zn dissolved in Cu appears to be constant up to 60 mol-% Zn. Evidently, the assumption of ZnO incorporated in the CuO bulk is corroborated by the EXAFS measurements (see Figure 3.4). The dissolution of Zn in CuO may cause both the Cu lattice expansion and the Cu microstrain measured in the reduced Cu/ZnO

catalysts.

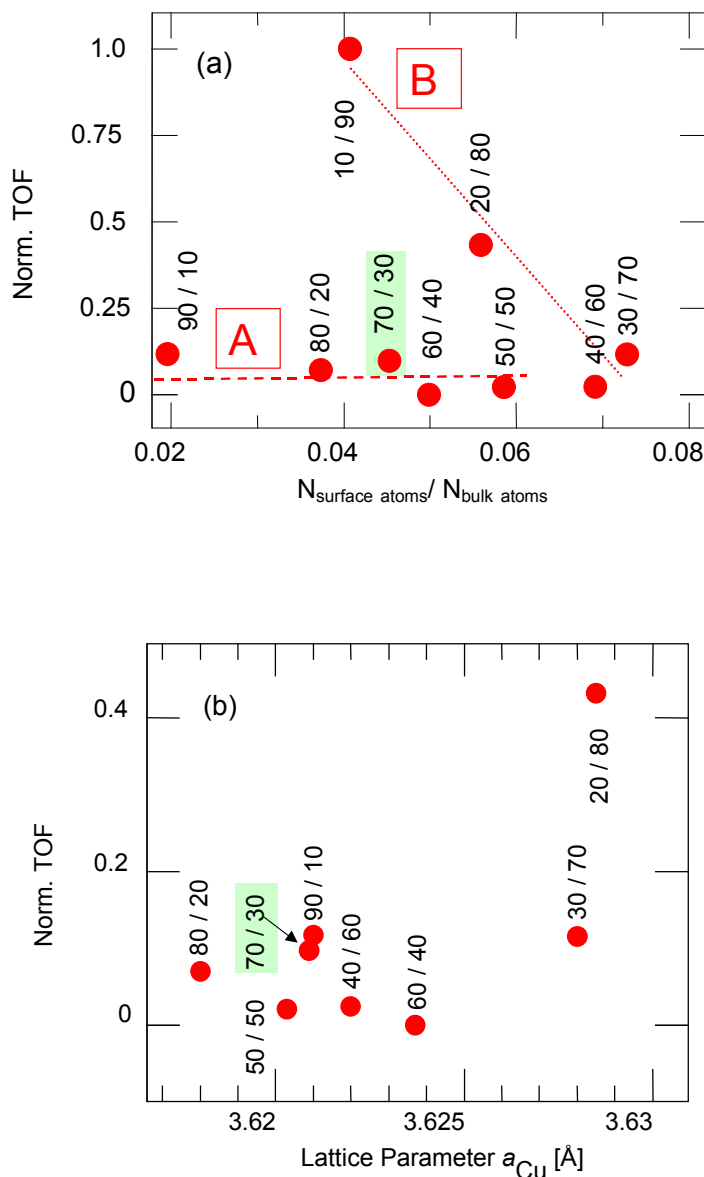


Figure 4.9: Normalized turn-over frequency (TOF) for methanol production as a function of (a) the copper atom dispersion (expressed as the ratio of Cu surface atoms determined by N_2O RFC to the number of the bulk atoms based on XRD crystallite size determination), (b) the copper lattice parameter a .

Binary Cu/ZnO samples of industrial interest possess Cu crystallites in the range of 100 – 200 Å. Obviously, XRD is a suitable method to investigate microstructural parameters (*e.g.* size and strain) within this crystallite size regime. Other techniques that are more surface sensitive or probe the short range structural order (*e.g.* IR and EXAFS) require smaller cluster sizes to elucidate the minor structural changes in the systems described in this work. Therefore, mostly copper loadings that are less relevant for industrial application have been investigated and it needs to be kept in

mind that results obtained for smaller copper clusters may not be directly transferable to the catalysts used in industry.

There is only a seemingly discrepancy between our findings and other experimental work by Spencer concerning the precursor phase affording a maximum activity [Spencer99]. In his publication the activity is given as an absolute production rate expressed per weight catalyst, whereas we refer to an intrinsic rate in terms of TOF for the most active catalyst. Nevertheless, a maximum in absolute production rate is attained for a sample with ~ 30 mol-% Zn stemming from a zincian malachite precursor which is similar to the results by Spencer. Therefore, we propose that an optimum catalyst should feature both a high specific Cu surface area and strained Cu clusters.

4.3 Summary

A complete series of binary Cu/ZnO samples was subjected to methanol synthesis screening experiments. It was found that the production rate of methanol is not a linear function of the specific Cu surface area over the entire Cu/ZnO composition range. XRD line profile analysis revealed a considerable microstructural strain in both Cu and ZnO in some samples. Furthermore, it was shown that the TOF of methanol synthesis is directly correlated to the strain in the Cu metal phase. This experimental evidence clearly indicates that the specific Cu surface area of Cu/ZnO samples alone cannot unequivocally account for the observed methanol production rates of these systems. Structural defects of Cu resulting from ZnO in Cu, incomplete reduction or epitaxial orientation to ZnO are believed to cause strain which modifies the Cu surface area and, thus, influences the catalytic activity.

Furthermore, changes in the microstructure of both copper and ZnO (*i.e.* size, strain, and lattice parameter) were found to coincide with changes in phase composition of the hydroxycarbonate precursors (structure of zincian malachite and the transition from the aurichalcite-rich to a Cu containing hydrozincite phase composition). The formation of ZnO-CuO solid solutions (~ 5 % ZnO in CuO) was detected which may lead after reduction to the formation of Cu-Zn alloy. For a compositional range of more than 60 mol-% Zn the strained Cu crystallites expose a Cu surface which is more active than that of a 30 mol-% Zn catalyst. Hence, it is concluded that the phase composition of the hydroxycarbonate precursor directly influences the active phase of the Cu/ZnO catalyst.

5 In situ Studies on Cu/ZnO using X-ray diffraction and absorption

5.1 Introduction

In this chapter the two complementary bulk techniques, *in situ* X-ray diffraction and X-ray absorption spectroscopy are employed to elucidate bulk structural changes of Cu in Cu/ZnO systems during activation and under methanol steam reforming conditions. Recently, the methanol steam reforming reaction has attracted much interest because hydrogen can be produced with high selectivity and activity which can be used for mobile fuel cell applications. The steam reforming reaction can be regarded as the reversed methanol synthesis reaction, which was investigated in the previous chapter. However, it is assumed that the concept of micro-reversibility can not be applied to make predictions about the mechanism and kinetics of methanol steam reforming due to the differences in operating conditions and partial pressures of reacting species (*e.g.* higher concentration of MeOH than in methanol synthesis). Furthermore, different bulk phases can be present due to the different redox potential of the reaction gas which can lead to different bulk phases and hence active sites.

First, the evolution of bulk phases during activation of the catalyst (*i.e.* reduction in hydrogen with ('wet') and without ('dry') additional water vapor) is investigated. Two different reduction atmospheres are employed in order to obtain active catalysts with different structural properties. Second, correlations between the bulk structure of Cu on ZnO and activity or selectivity in the steam reforming of methanol are presented. Furthermore, oxygen addition to the feed is used to change the oxidation state of copper during a working conditions for methanol steam reforming. Corresponding changes in the local structure are followed by a EXAFS analysis carried out at the Cu K and Zn K edge.

5.2 In situ XRD

5.2.1 Reduction of the CuO/ZnO precursor

Structural changes of the CuO/ZnO system were monitored by *in situ* XRD during temperature programmed reduction (TPR). The evolution of the intensity of the Cu (111) line afforded the onset and extent of reduction while the evolution of the crystallite size was obtained from the linewidth. In Figure 5.1 (a) the evolution of XRD patterns (for the Cu (111) peak) is shown during TPR of the sample D70/30 in the range from 433 K to 523 K in 2 vol-% hydrogen. In Figure

5.1 (b) the normalized H_2 and H_2O MS signals are correlated to the intensity evolution of the Cu (111) peak. It can be seen that the uptake of H_2 coincides with the evolution of H_2O . The increase in the intensity of the Cu (111) peak indicates the growth of Cu crystallites. Because Cu particles large enough to be detected by XRD need to form, the onset of the evolution of the Cu (111) line is delayed with respect to the hydrogen uptake and the evolution of water.

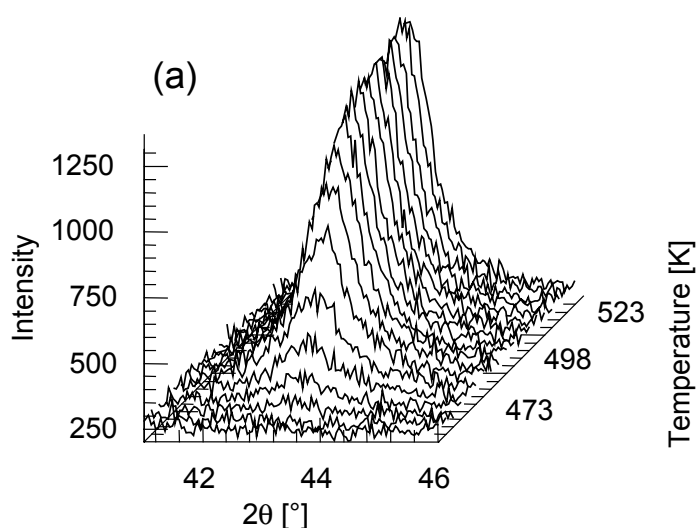
Results of the TPR of all samples are summarized in Table 5.1. In most cases the ‘wet’ reduction occurred at a higher temperature of about ~ 10 K than the dry reduction. In contrast, the onset temperature is only slightly affected by the Cu and Zn concentration. With decreasing copper content the onset of reduction is shifted from 468 K (pure CuO, sample C100/0 ‘wet’) to 448 K for the sample C40/60 (‘dry’). In addition, in most cases, the wet reduction leads to an increase in Cu particle size with respect to that of the ‘dry’ reduced samples (~ 10 Å larger). With an increasing Zn content the Cu/ZnO samples exhibited a decreasing Cu particle size. The exception to the decreasing particle size trend are the 60/40 samples.

Table 5.1: Onset of reduction during TPR and the corresponding copper crystallite sizes after reduction measured by in situ XRD. The reduction was performed under ‘dry’ and ‘wet’ reducing conditions.

Sample	pH during precipitation	Onset of reduction [K]		Cu crystallite size [Å]	
		Reduction conditions			
		‘dry’	‘wet’ ^d	‘dry’	‘wet’
C100/0	constant	463	468	215	190
C90/10	constant	443	458	112	127
C80/20	constant	473	443	90	92
C70/30	constant	438	458	68	70
C60/40	constant	443	453	77	78
C50/50	constant	463	453	50	58
C40/60	constant	443	448	42	47
D100/0	decreasing	458	468	148	171
D70/30	decreasing	448	463±5 ^a	81	79
D60/40	decreasing	448	453	101	108
D50/50	decreasing	448	468	45	52
D40/60	decreasing	443	453	38	40

^a reproduced in 3 measurements. ^b determined at the end of the TPR run at 523 K. ^c reduction performed in ~ 2 vol-% H_2 . ^d reduction performed in ~ 2.5 vol-% H_2 and 3 vol-% H_2O .

The evolution of the Cu crystallite size for the constant pH and decreasing pH sample batches is shown in Figure 5.2 as a function of reduction temperature. The Cu crystallite size appears to grow linearly with time (applying an effective heating rate of 0.5 K/min). The decreasing slope with increasing Zn-content indicates that ZnO exerts an “anti-sintering” influence on the Cu particles during temperature programmed reduction. Figure 5.2 (a) + (b) illustrate that during TPR the samples with the highest Zn-concentration (samples with C40/60 and D40/60) exhibit only minor crystallite growth with increasing temperature, whereas the Cu clusters in samples with a higher Cu-concentration tend to sinter more. Apparently, the tendency to sinter depends on the interaction with the ZnO-matrix and the Cu/Zn ratio. The exception to the previously mentioned trends are the samples with 70 mol-% Cu (C70/30 and D70/30) which show after reduction a Cu crystallite size that is 10 Å lower than that of the sample with 60 mol-% Cu (C60/40 and D60/40). For lower Cu-concentrations the difference in crystallite size for ‘wet’ and ‘dry’ reduced samples is much less pronounced than for Cu-rich samples.



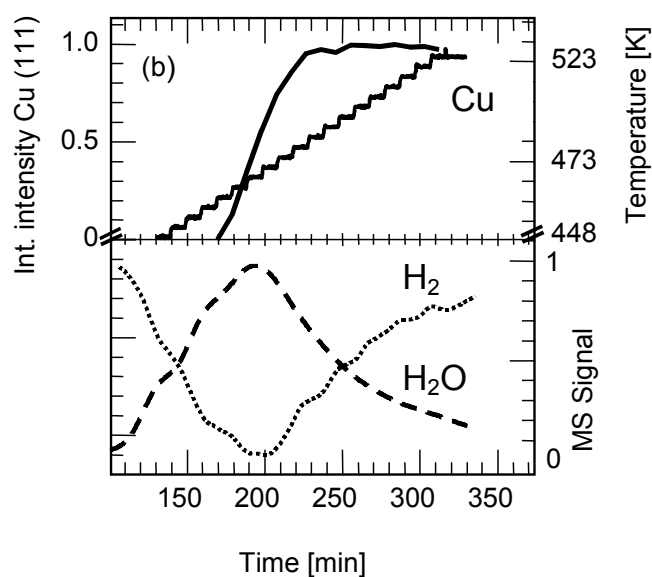
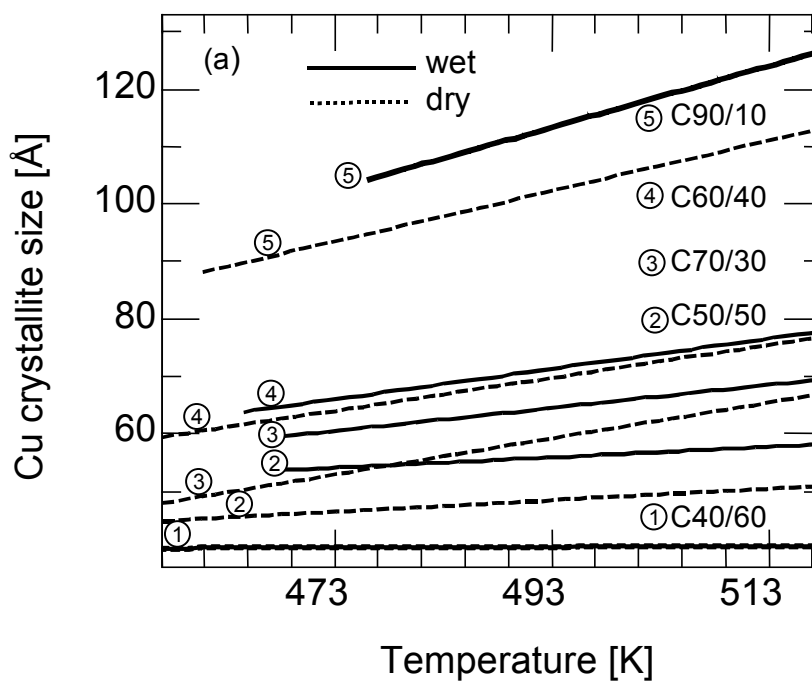


Figure 5.1: (a) Evolution of the Cu (111) peak during reduction of a CuO/ZnO sample (D70/30) in 2 vol-% hydrogen measured by in situ XRD. Measuring time 7 min/scan and an effective heating ramp of 0.5 K/min. (b) Corresponding normalized mass spectrometer signals of H₂O and H₂ during TPR and evolution of integrated intensity of the Cu (111) peak.



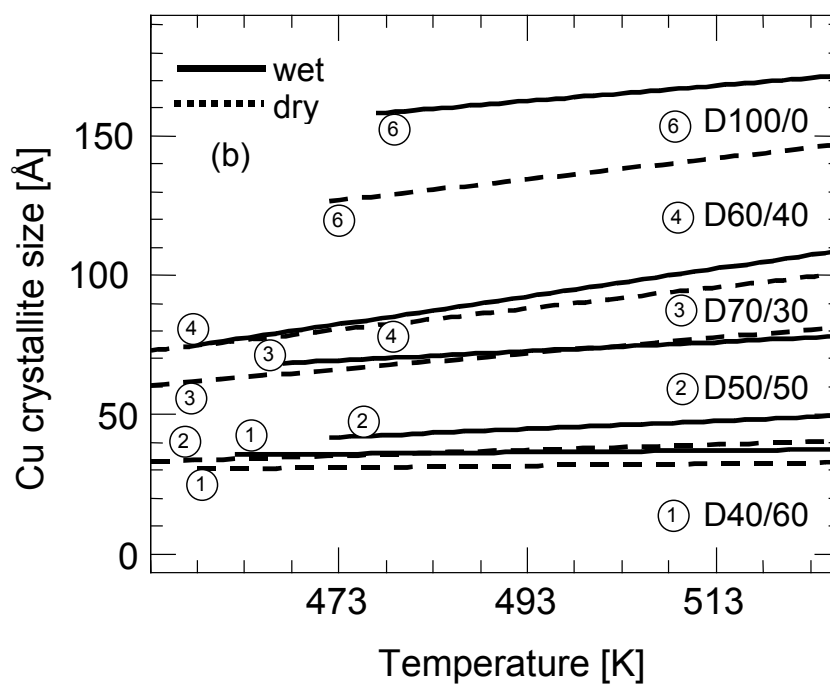


Figure 5.2: Evolution of Cu crystallite size during TPR for samples with different Cu/Zn ratio measured both in 3 vol-% H₂ ('dry') and 2.5 vol-% H₂ + 3 vol-% H₂O ('wet') in 100 ml/min for both sets of sample preparations: (a) constant pH preparation, (b) decreasing pH preparation. The temperature was raised with an effective heating ramp of 0.5 K/min.

5.2.2 Steam Reforming of Methanol

The time on stream behavior of sample D60/40 in the *in situ* XRD cell is shown in Figure 5.3 (a). The catalyst was heated in the feed (MeOH/H₂O ~ 4/1 in a flow of 120ml/min He) from RT to 430 K at 5 K/min and then heated stepwise to 523 K at 0.5 K/min during which XRD measurements were taken at constant temperature. The onset of the steam reforming reaction at 433 K is detectable by the consumption of water and methanol and the evolution of the products H₂ and CO₂. The long-term behavior shows a gradual deactivation of ~ 9 % after 7 h. The concentration of CO during this run was < 1000 ppm. The rapid deactivation of a pure copper sample (D100/0 ‘wet’ reduced) is depicted in Figure 5.3 (b). It can be seen that the initial activity for hydrogen production is only 25 % of that of the more active D60/40 Cu/ZnO sample. After 7 h time on stream the final activity amounted to only 30 % of its initial peak activity. The characteristics of the catalytic activity of Cu/ZnO catalysts obtained from both preparation batches and reduction procedures (‘dry’ and ‘wet’) are summarized in Table 5.2. Because the pure copper samples deactivated very rapidly no reliable conversion and selectivity data could be obtained. Highest conversion (53 %) is obtained for the ‘wet’ reduced sample D70/30, whereas the copper rich sample ‘dry’ C90/10 exhibits the lowest conversion. Similarly, the selectivity shows a strong dependence on the composition and reduction compositions and ranges from 69 % (‘wet’ C50/50) to 16 % (‘dry’ C90/10). In Figure 5.4 (a) + (b) the selectivity to CO₂ is shown as a function of methanol conversion for both preparation methods (constant and decreasing pH) and for both reduction procedures (‘dry’ and ‘wet’). It can be observed that the ‘wet’ reduced samples exhibit an enhanced selectivity compared to that of the ‘dry’ reduced samples at the same conversion.

Table 5.2: Initial methanol steam reforming catalytic activity data (conversion of methanol, selectivity to CO₂, hydrogen production rate) for differently reduced Cu/ZnO catalysts at 523 K.

Sample	Reduction conditions	Conversion of MeOH, X _{MeOH} [%]	Selectivity to CO ₂ , S _{CO2} [%]	Hydrogen production rate, r _{H2} [$\mu\text{molH}_2\cdot\text{g}_{\text{cat}}^{-1}\cdot\text{s}^{-1}$]	Cu Surface area ^b S _{Cu(XRD)} [$\text{m}^2\cdot\text{g}^{-1}$]	TOF ^c [s^{-1}]
C100/0	<i>dry</i>	No activity	No activity		13	-
	<i>wet</i>	-	-		16	-
C90/10	<i>dry</i>	14	16	92	20	0.19
	<i>wet</i>	15	17	77	18	0.17
C80/20	<i>dry</i>	26	34	245	22	0.46
	<i>wet</i>	13	0	145	23	0.27
C70/30	<i>dry</i>	24	60	293	25	0.55
	<i>wet</i>	22	78	333	22	0.54
C60/40	<i>dry</i>	36	39	350	18	0.80
	<i>wet</i>	20	79	318	19	0.74
C50/50	<i>dry</i>	29	56	380	24	0.64
	<i>wet</i>	20	72	349	22	0.64
C40/60	<i>dry</i>	22	50	318	23	0.67
	<i>wet</i>	27	56	385	20	0.61
D100/0	<i>dry</i>	- ^d	- ^d		13	-
	<i>wet</i>	10	29	131	13	0.41
D70/30	<i>dry</i>	33	42	485	21	0.94
	<i>wet</i>	38	37	426	21	0.84
D60/40	<i>dry</i>	32	43	482	15	1.27
	<i>wet</i>	23	72	480	13	1.47
D50/50	<i>dry</i>	19	50	402	27	0.61
	<i>wet</i>	20	67	460	25	0.75
D40/60	<i>dry</i>	29	53	433	27	0.66
	<i>wet</i>	27	59	480	23	0.85

^areaction conditions H₂O/MeOH = 1/4, p = 101 kPa, total flow ~ 140 ml/min. ^bcalculated from the Cu crystallite size based on XRD data obtained during reaction. ^chydrogen molecules produced per surface copper atom per second. ^dfast deactivation.

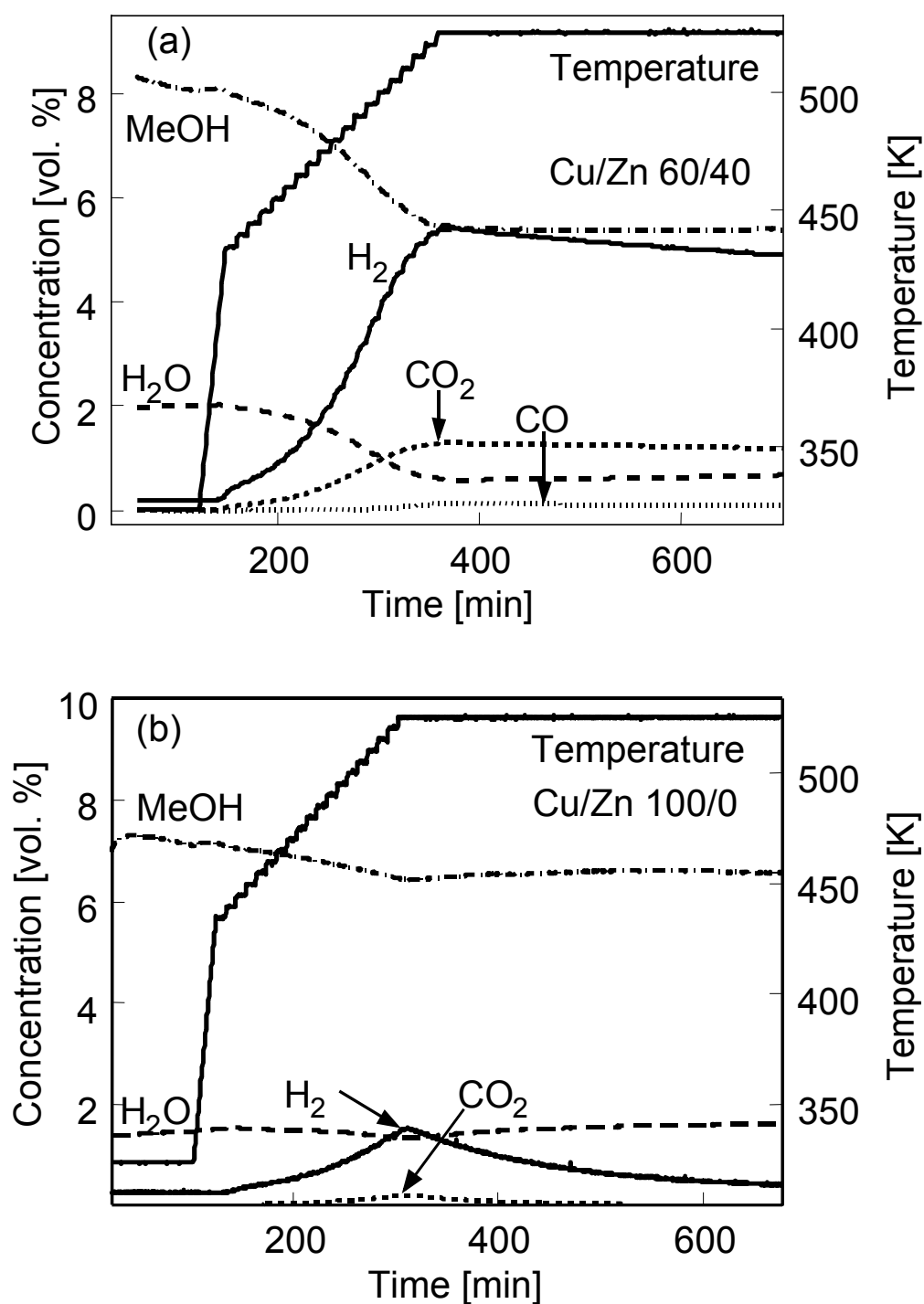


Figure 5.3: (a) Time on stream behavior for sample D60/40 ('dry' reduced) measured in XRD in situ cell. (b) deactivation behavior of a pure Cu sample (D100/0, 'wet' reduced). Experimental conditions: MeOH/H₂O ~ 4/1 in 120 ml/min He and temperature ramp from 433 K to 523 K at 0.5 K/min.

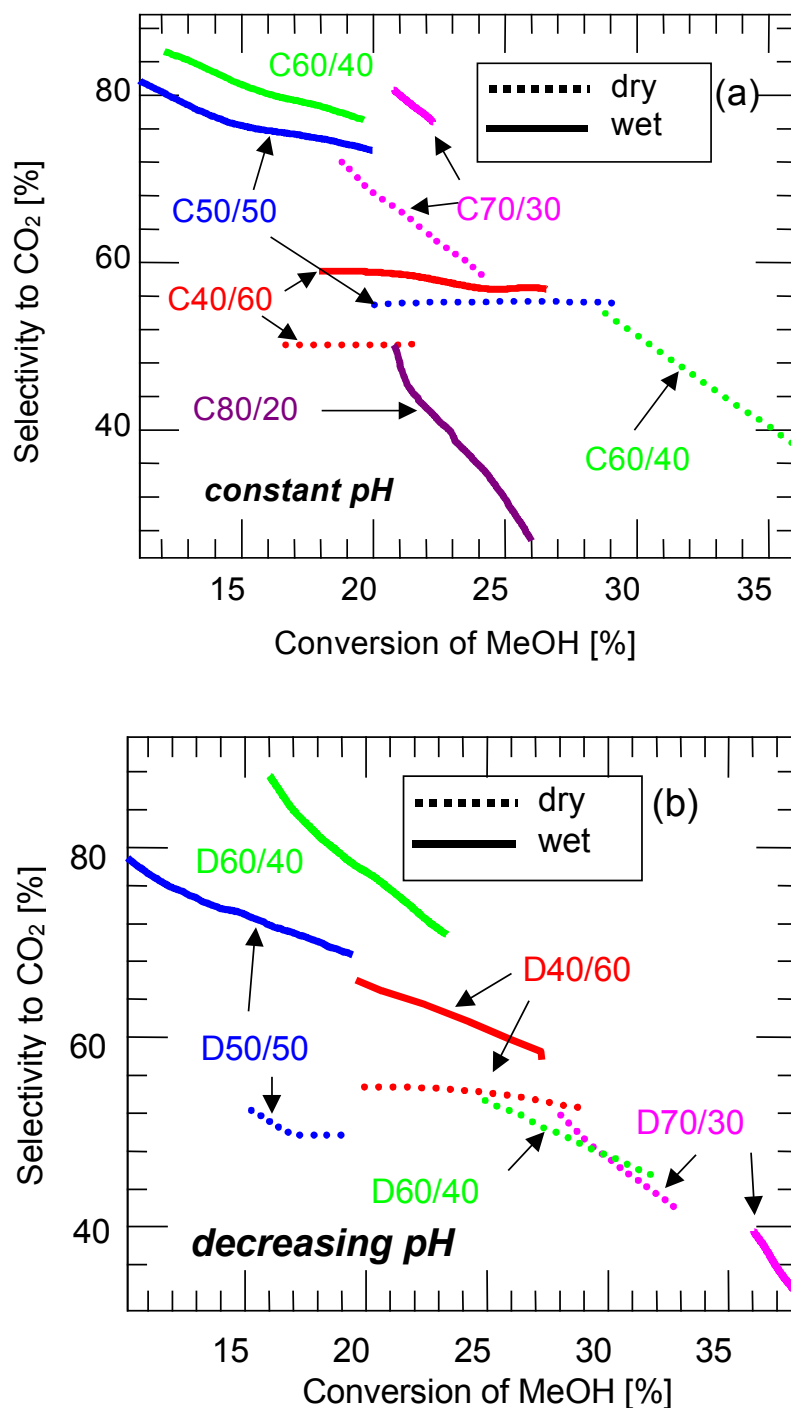


Figure 5.4: Selectivity to CO_2 as a function of the conversion of MeOH at 523 K with a flow of MeOH/ H_2O (ratio of $\approx 4/1$) in 120 ml/min He; samples were obtained by 'dry' and 'wet' reduction, (a) samples prepared by the constant pH method, (b) samples prepared by the decreasing pH method.

In addition, the *in situ* XRD investigations allowed to calculate the Cu crystallite sizes of *operating catalysts* which can be used to estimate copper surface areas. Hence, it is possible to detect influences of the Cu crystallite size (and metal surface area) on the activity without transferring the sample for *ex situ* measurements. In Figure 5.5 the initial hydrogen production rate under methanol steam reforming conditions is depicted as a function of the copper surface area for both reduction and preparation methods.

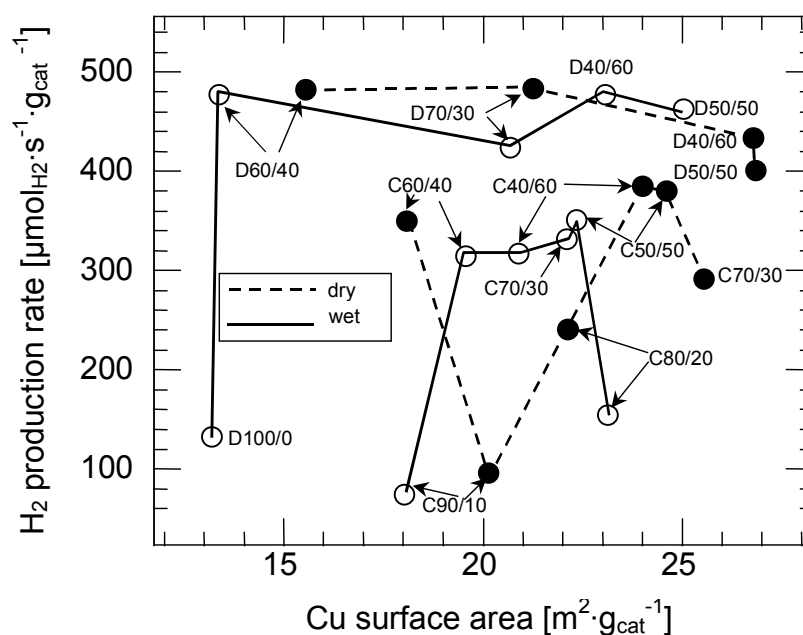


Figure 5.5: Initial hydrogen production rate as a function of the Cu metal surface area for catalysts prepared at constant pH method and at decreasing pH method. Both sample series were activated under 'wet' and 'dry' reduction conditions. The Cu surface area is estimated by XRD. Reaction conditions were the same as in Figure 5.3.

No common trend of the production rate on the surface area can be established for all samples. It can be seen that the D-series samples exhibit a higher hydrogen production rate than the samples of the C-series. Furthermore, the samples prepared at constant pH show a higher variation in production rate with increasing copper surface area.

The TOF for the initial activity as a function of ZnO-content in the catalysts is given in Figure 5.6. The reaction rate is normalized to the number of Cu metal surface atoms which are all assumed to be the catalytically active sites of copper. It can be seen that the TOF values vary with the composition. In addition, samples prepared at decreasing pH show a higher intrinsic activity than the samples of the constant pH series. The reduction conditions afford only small differences in activity for a given set of samples.

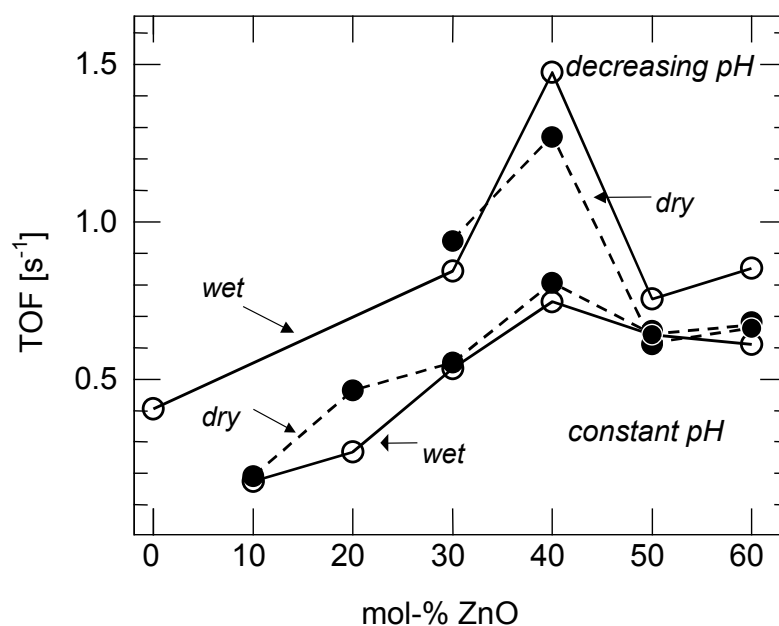


Figure 5.6: Initial turn-over-frequency (TOF) for hydrogen production as a function of ZnO-content for catalysts prepared according to the decreasing and the constant pH method (both under 'dry' and 'wet' reduction conditions). Reaction conditions where the same as in Figure 5.3.

5.2.2.1 Deactivation during time on stream

The evolution of the FWHM of the Cu (111) line is measured during steam reforming reaction at 523 K for 7 h by *in situ* XRD. Figure 5.7 (a) + (b) shows the evolution of Cu crystallite sizes, as determined from the Cu (111) line width, during time on stream for both preparation batches. Evidently, the Cu crystallite sizes exhibit only minor changes as a function of the time on stream.

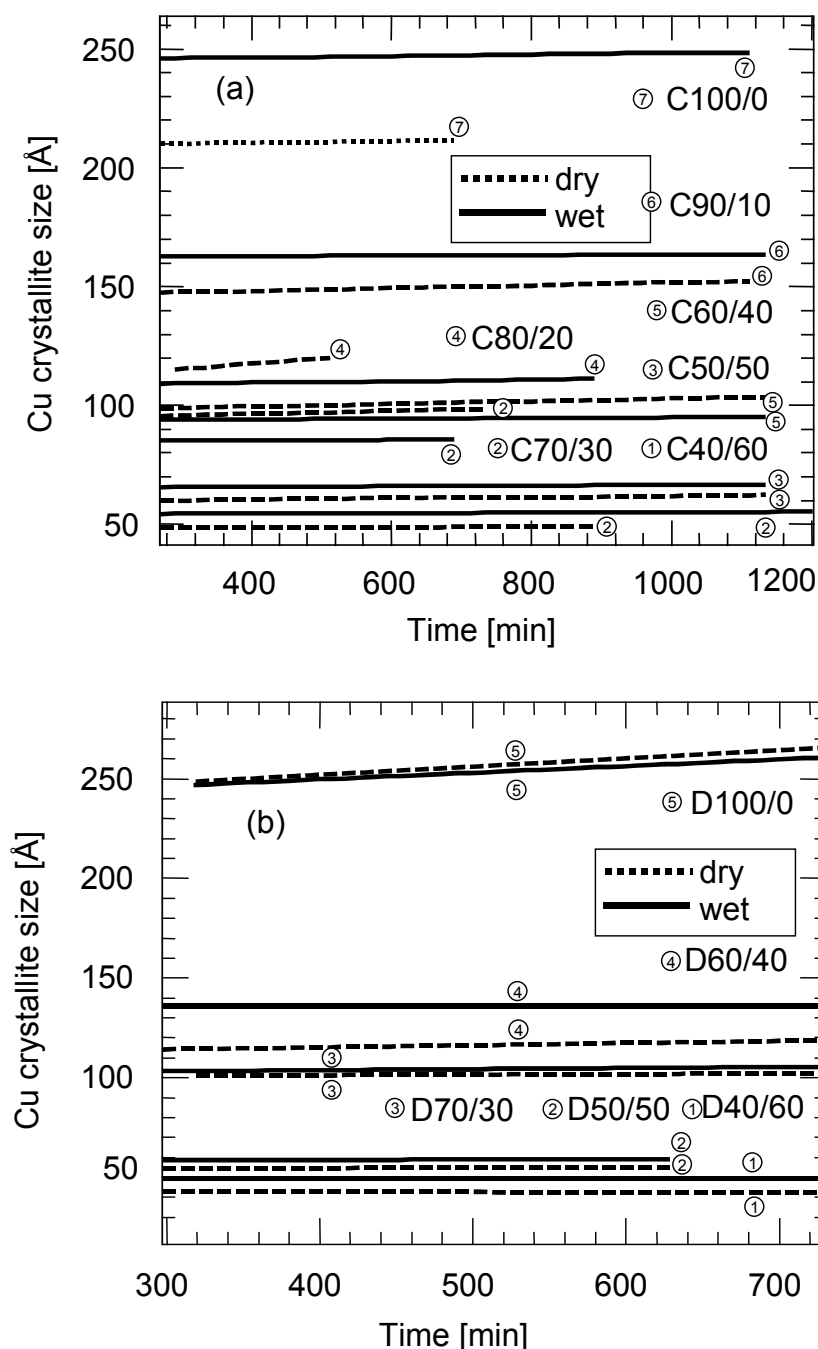


Figure 5.7: Evolution of Cu crystallite size under steam reforming conditions at 523 K for different catalyst with compositions and different reduction pretreatment as indicated over course of 7 h: (a) constant pH preparation, (b) decreasing pH preparation. Reaction conditions: same as in Figure 5.3.

It can be seen that the crystallite size has increased compared to the crystallite sizes after reduction (Figure 5.2). Furthermore, the same sequence of crystallite sizes as a function of the composition is obtained, but in some cases the initially larger ‘wet’ reduced particles now exhibit a smaller crystallite size (*e.g.* samples C80/20, C60/40, C70/30) than the dry reduced samples. It was found, that the Cu crystallites sizes exhibit only minor changes as a function of the time on stream.

In Figure 5.8 the decrease in hydrogen concentration during time on stream is shown for two samples together with the increase in crystallite size resulting from sintering. The increase in crystallite size for the pure copper sample (D100/0) is almost twice as large as that of a copper-rich sample (D60/40). In addition, this corresponds to a larger decrease in the hydrogen production rate detected for the pure copper sample.

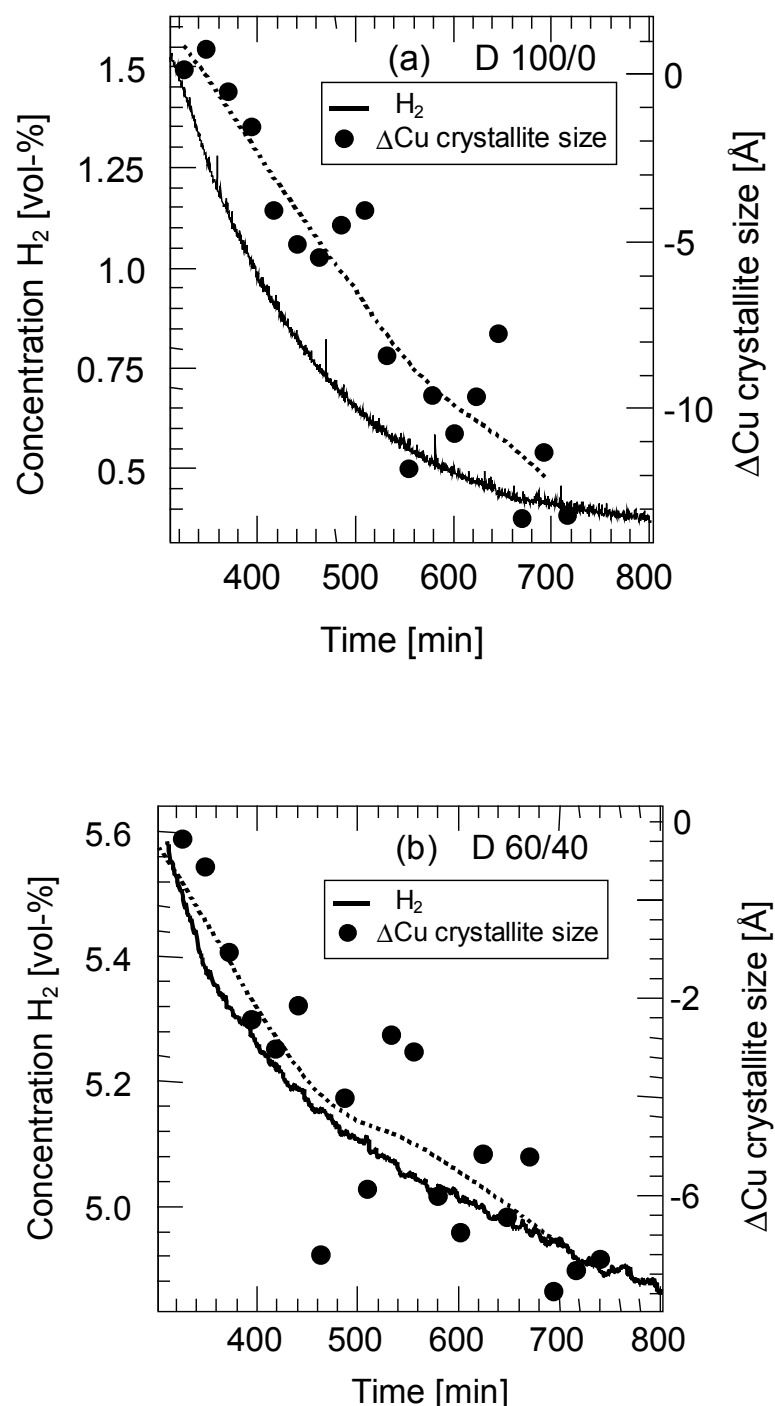


Figure 5.8: Evolution of copper crystallite size during time on stream at 523 K together with the effluent concentration of H_2 in the in situ XRD cell; (a) sample D 100/0 ('wet' reduced), (b) sample D 60/40 ('dry' reduced). Dashed line is guide to the eye.

5.2.3 Oxygen addition cycle

In Figure 5.9 four XRD patterns of a Cu/ZnO catalyst (sample C60/40) obtained after calcination (a), steam reforming (b), oxidation (c), and re-reduction (d) are displayed. The pattern indicative of CuO (a) is converted to that of metallic Cu (b) after the calcined sample is reduced in the steam reforming feed with no additional copper oxide phases detectable. The addition of 15 vol-% O₂ to the feed at 523 K for 100 min resulted in the formation of mostly Cu(I) oxide together with some minor amounts of CuO (c). After re-reduction in the feed at 523 K the XRD pattern of metallic Cu can be seen but with a decreased line width of the Cu (111) peak (d).

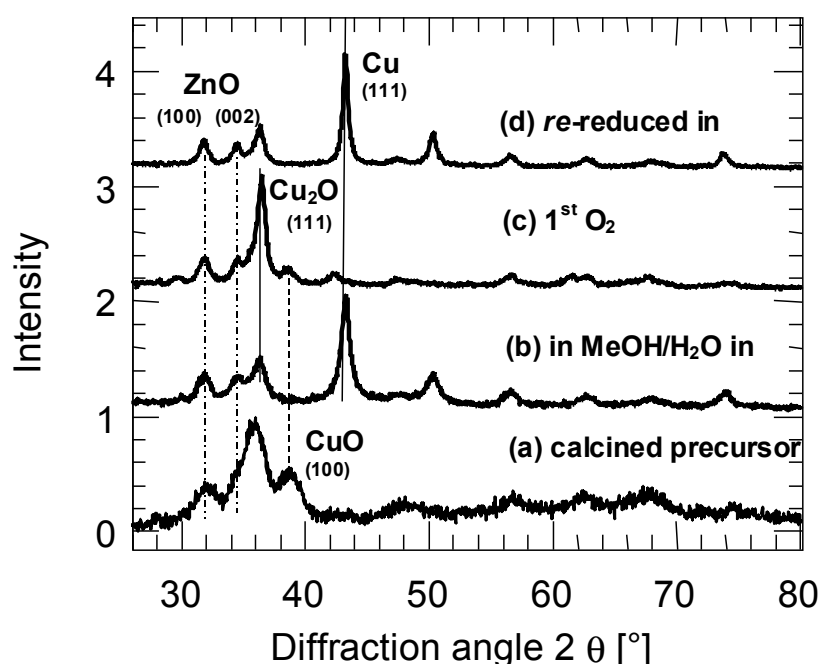


Figure 5.9: X-ray diffraction patterns of a sample with a composition of 60 at-% Cu and 40 at-% Zn (C60/40) during different stages of treatment. Upon reduction the calcined CuO (a) is transformed into Cu metal which is preserved under methanol steam reforming conditions at 523 K (b). Oxygen treatment resulted in a mixture of Cu(I) oxide and Cu(II) oxide (c). The oxidic copper phases are re-reduced in the feed to metallic Cu with a decreased line width (d). Characteristic (hkl) diffraction lines of CuO, Cu₂O, and Cu metal are indicated.

Changes in the gas phase composition (H₂, MeOH, CO₂, and H₂O) during two oxygen addition cycles are depicted in Figure 5.10. It can be seen that adding oxygen to the feed resulted in a complete loss of activity for the steam reforming reaction. In addition, the formation of water and CO₂ during the oxygen addition indicates the occurrence of total oxidation of methanol. The low hydrogen concentration during oxygen addition intervals might result from methanol dehydrogenation. The oxidative poisoning was, however, completely reversible with no loss in hydrogen productivity. Oxidation and re-reduction experiments were carried out on selected samples (C70/30, C60/40, C40/60) activated under ‘dry’ reduction conditions. The copper

crystallite sizes, the methanol steam reforming activity, and selectivity are summarized in Table 5.3. An increase in conversion, selectivity and hydrogen production rate with the number of oxidation-reduction cycles is detected. In addition, for all samples the copper crystallite size is increasing with each oxidation cycle (Table 5.3). For instance, the copper crystallite size of the sample C70/30 increases from 76 to 110 Å. After the oxidative treatments the XRD peaks of ZnO (e.g. 100, 002) are equally affected as their profiles become gradually more pronounced. Profile fitting of the ZnO (100) peak of the same sample gives crystallite sizes that increase slightly upon oxidation and re-reduction from 80 to 90 Å. The relative changes of the copper and zinc oxide lattice parameter after reduction, under stream reforming conditions, and after successive oxygen/re-reduction cycles are depicted in Figure 5.11. The continuous increase in lattice parameter of Cu and ZnO indicates an expansion of the unit cell under methanol steam reforming conditions after each oxidation/re-reduction steps with respect to the freshly reduced sample.

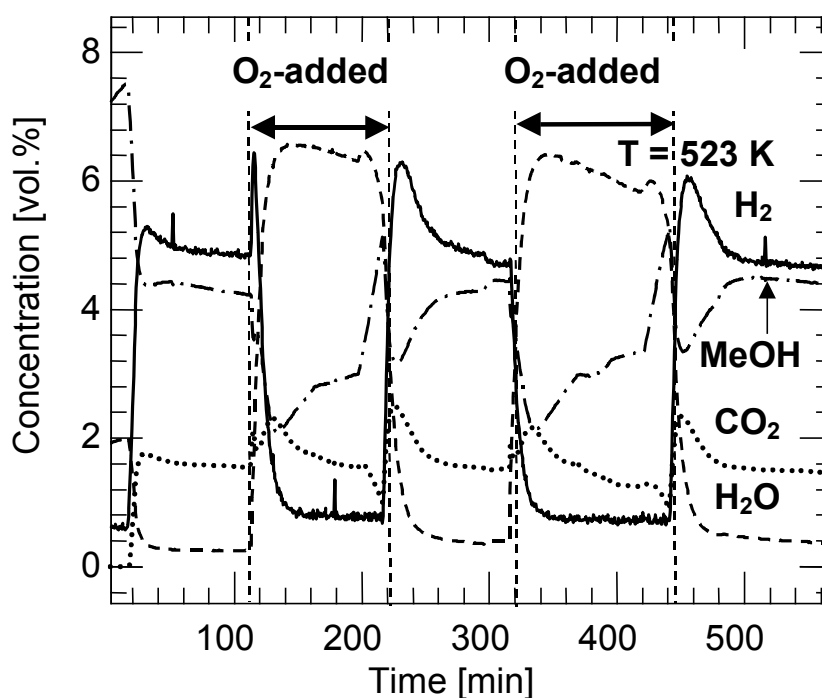


Figure 5.10: Evolution of gas phase concentration of H_2 , MeOH, CO_2 , and H_2O in XRD cell under methanol steam reforming conditions during addition of oxygen (15 vol-% O_2) to the feed for two intervals of ~ 100 min. Sample C60/40 'dry' was used.

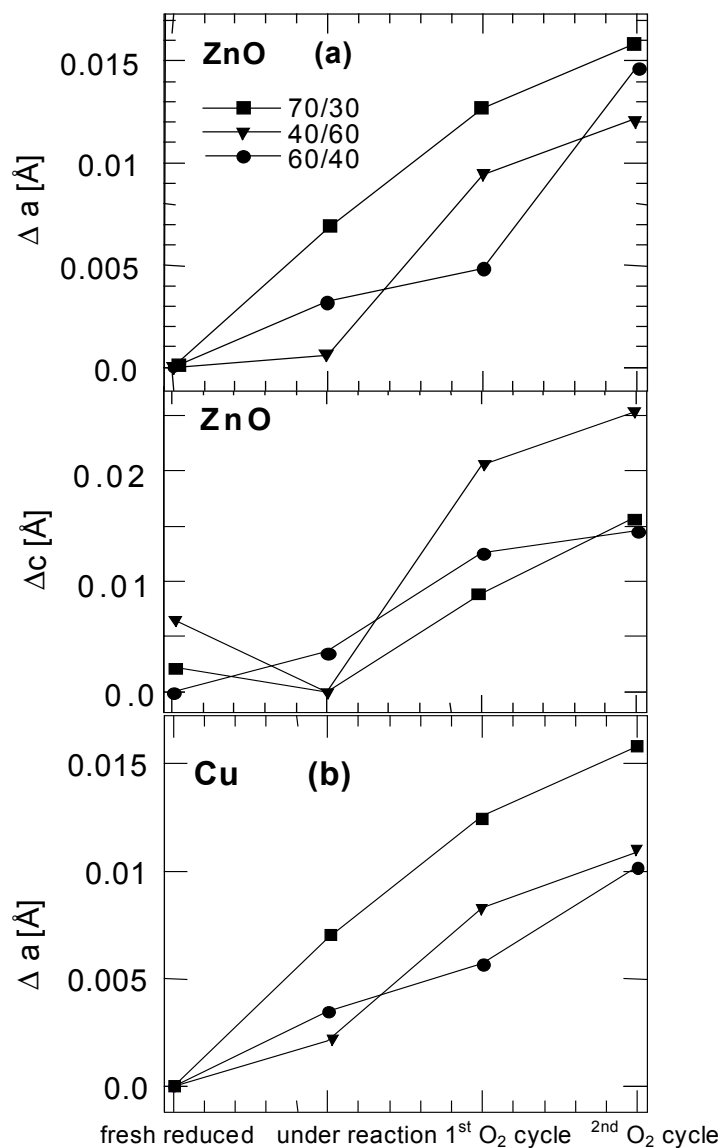


Figure 5.11: Relative change of ZnO lattice parameters a and c (a) and Cu lattice parameter a (b) with respect to the values of the fresh reduced samples C70/30, C60/40, and C40/60 under methanol steam reforming, and after two successive oxygen addition cycles.

Table 5.3: Change of catalytic activity data (conversion of methanol, selectivity to CO₂, hydrogen production rate) obtained in XRD and XAS cells after repeated oxidation and reduction steps. All samples were prepared according to the constant pH method and reduced at 'dry' conditions. The data was obtained at 523 K with a flow of MeOH/H₂O (ratio ~ 4/1) in 120 ml/min (XRD cell) or 25 ml/min (XAS cell). Conversion and selectivity are given as initial values.

Sample name ^a	Number of oxidation/reduction cycles ^b	Cu crystallite size [Å] ^a	XRD cell			XAS cell		
			X _{MeOH} [%]	S _{CO2} [%]	r _{H2} ^d [μmolH ₂ ·g _c at·s ⁻¹]	X _{MeOH} [%]	S _{CO2} [%]	r _{H2} ^d [μmolH ₂ ·g _c at·s ⁻¹]
C70/30	0	76	25		483	25	54	145
	1	110	62	61	531	25	58	155
	2 ^c	120	-	-	-	23	70	166
C60/40	0	100	51	37	470	20	48	133
	1	120	64	42	556	26	51	162
	2	130	62	42	535	27	53	176
C40/60	0	50	40	50	450	20	53	150
	1	70	44	80	620	24	53	160
	2	80	36	94	618	-	-	-
C30/70	0	- ^c	-	-		20	53	105
	1					24	53	146
C10/90	0	-	-	-		13	55	92
	1					14	55	92
	2					14	62	103

^a based on the Scherrer equation for the Cu (111) reflection. ^b "0" denotes the fresh reduced catalyst, where "I" and "II" refer to first and second oxidation/reduction cycle, respectively. ^c second oxidation step not performed. ^d production rate of hydrogen per g catalyst and second.

5.3 In situ XAFS

5.3.1 Reduction of CuO/ZnO precursor

In situ X-ray absorption spectroscopy was performed at the Cu K edge to determine the amount of less crystalline or amorphous copper phases and the evolution of the short-range order structure under reaction conditions, not accessible by the *in situ* XRD measurements (less than ~ 5%). In Figure 5.12 (a) the evolution of Cu K near-edge spectra measured during TPR of a sample with 70 mol-% copper (D70/30) is presented. The gradual decrease of the 'white line' of the Cu K edge indicates the reduction of the copper oxide bulk phase to the Cu metal. A principal component

analysis of the Cu K edge XANES spectra revealed that three primary components were necessary to reconstruct the experimental XANES spectra.

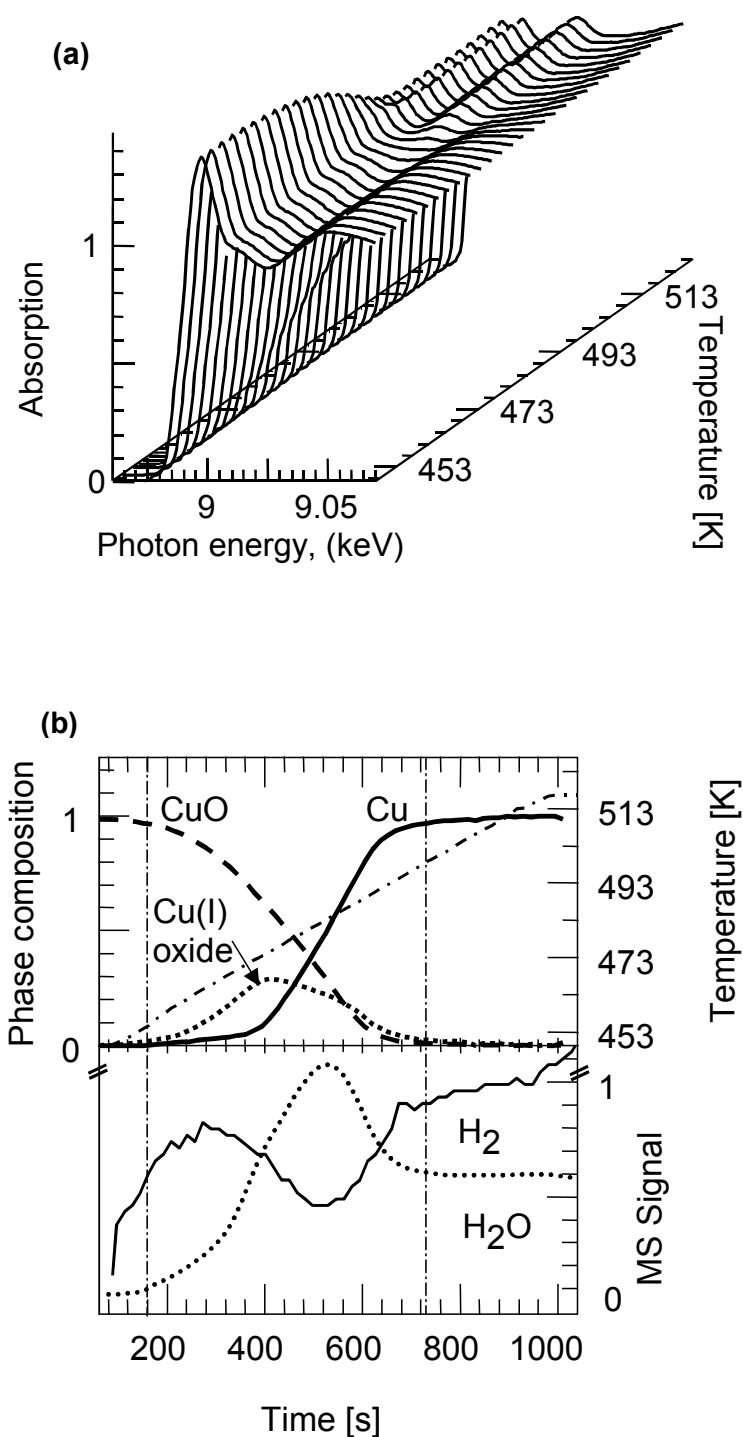


Figure 5.12: a) Evolution of Cu K edge XANES spectra of a CuO/ZnO sample (C70/30) during TPR in 8 vol-% H₂ with 5 s/frame and a heating rate of 5 K/min. (b) Change in phase composition together with the MS signal of H₂O (dotted) and H (solid) during TPR. The quantitative phase analysis is based on a least squares fit using suitable reference spectra of Cu, Cu(I) oxide, and CuO as described in the text.

Using target transformation three probable reference compounds (*i.e.* copper, Cu(I) oxide, Cu(II) oxide) were identified. (Further details on the underlying mathematical algorithm can be obtained from reference [Ressler00]). *In situ* XRD results have shown that Cu in the oxide precursor was CuO and that it was completely reduced by TPR to pure Cu. The “target-transformed” spectra showed a good match with the first experimental XANES spectrum (containing only CuO) and the last spectrum (containing only Cu) in the TPR run. However, the result of the transformation for the third component showed considerable deviations from the experimental spectra of commercially available pure Cu₂O. The poor match is probably due to the high crystallinity of the reference compound which may not reflect the local disorder (structural defects, decreased crystallinity and/or crystallite size) of the intermediary formed Cu(I) oxide. In order to account for the small crystallite sizes a reduction of the amplitude above the XANES edge of the experimental spectra resulted in an enhanced agreement with the transformed spectra. Hence, Cu(I) oxide is indeed an intermediate during TPR and the “target-transformed” spectrum was taken as a reference for Cu(I) oxide for the least square fits. As an example, a Cu K edge XANES spectra of a partially reduced sample is shown in Figure 5.13 together with a linear fit of the corresponding reference components. The evolution of the phase composition during TPR of a D70/30 sample under ‘dry’ reduction conditions (2 vol-% H₂ in 25 ml/min He, heating ramp 5 K/min, temperature ramp 448 K to 523 K) is depicted in Figure 5.12 (b). It can be seen that the onset of reduction coincides with the evolution of H₂O and the uptake of H₂.

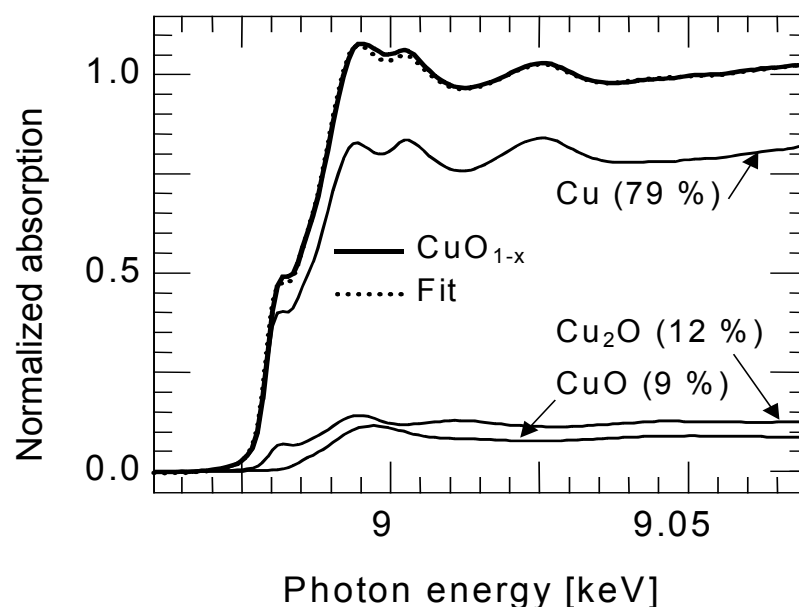


Figure 5.13: Linear combination XANES fit to a CuO_{1-x} spectrum during reduction using Cu, Cu(I) oxide, and CuO reference XANES spectra.

In Figure 5.14 (a) and (b) reduction curves (increase of extent of reduction to copper metal α , *i.e.* the amount of metallic copper formed (ranging from 0 to 1)) obtained from TPR (448 – 523 K) experiments for selected samples are presented. The sigmoidal shape of the reduction curves can be described by the Avrami-Erofeev equation ($\alpha = 1 - \exp(-kt)^n$), with k the rate constant, t the reduction time, and n the exponential factor (ranging from 2.5 to 4.6)).

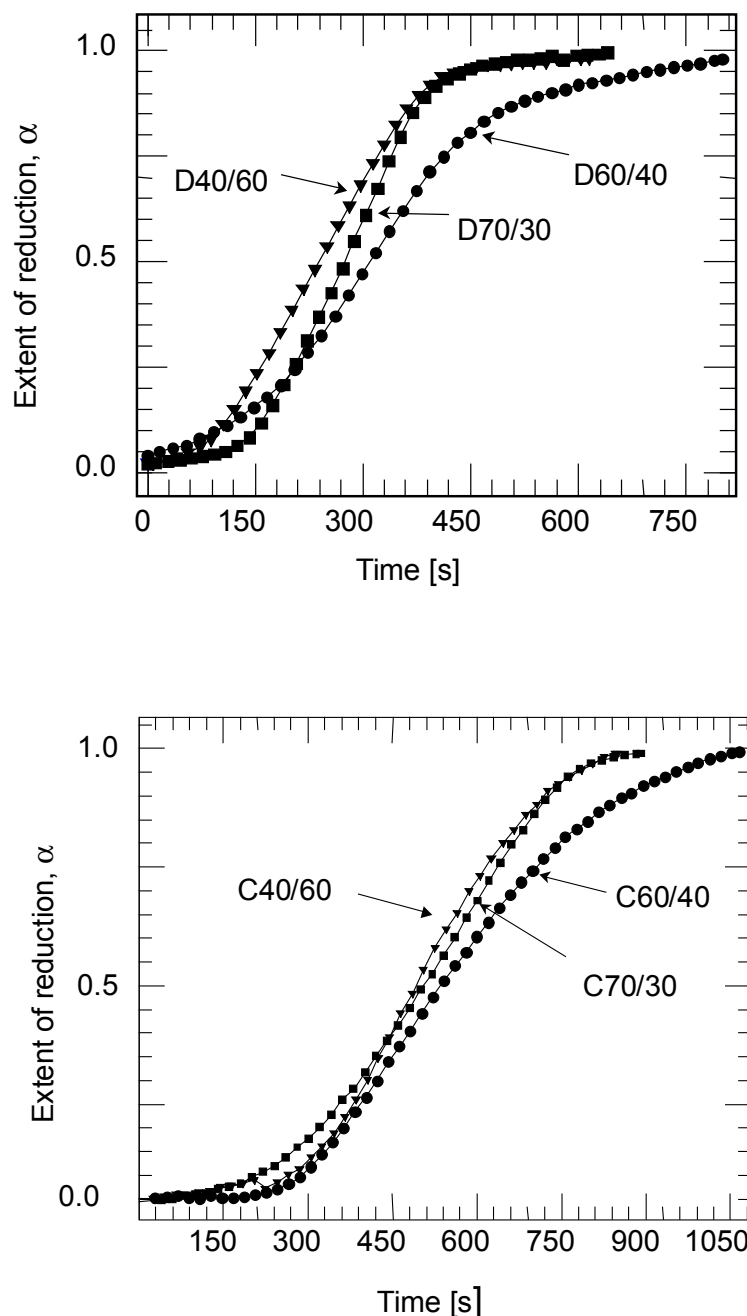


Figure 5.14: Evolution of extent of reduction, α , of CuO/ZnO precursor for (a) three decreasing pH samples (D70/30, D60/40, D40/60) measured by *in situ* XAFS (8 vol-% H_2) at 5 K/min from 433 K to 523 K; (b) three constant pH samples (C70/30, C60/40, C40/60) reduced with (2 vol-% H_2) at 5 K/min from 433 K to 523 K. The extent of reduction α was taken as the amount of Cu phase as determined by the linear combination XANES fits. The zero time is defined as the onset of reduction.

The Avrami-Erofeev kinetic behavior indicates a solid state process whose rate is determined by the formation and the growth of product nuclei. The fitting parameters obtained from least-square refinements of the reduction curves using this rate law are given in Table 5.4. For the CuO/ZnO samples prepared at constant pH the reaction rate k of the reduction in hydrogen decreases according to $k_{C40/60} > k_{C70/30} > k_{C60/40}$ while for the sample set prepared at decreasing pH a different sequence in reduction rate is obtained ($k_{D70/30} > k_{D40/60} > k_{D60/40}$). However, in both cases the sample with 60 mol-% Zn exhibits the lowest reduction rate. The exponential factor n shows an increase with decreasing copper content in the samples, pointing to differences in the growth of the Cu nuclei in three dimensions. The D-series samples reduced in a higher H_2 partial pressure (8 vs. 2 vol-%) showed larger exponential factors indicating a different dimensionality in crystal growth or a different rate (*i.e.* steps) in nucleation formation.

Table 5.4: Fitting parameters obtained from least-squares refinements using the Avrami-Erofeev equation, $\alpha = 1 - \exp(-kt)^n$, with α representing the extent of reduction (ranging from 1 to 0), k the rate constant, t the reduction time, and n the exponential factor for the evolution of the Cu metal phase measured during temperature programmed reduction in the XAS cell ('dry' reduction conditions: 2 vol-% H_2 for C-series samples and 8 vol-% H_2 for D-series samples, heat ramp from 433 K to 523 K at 5 K/min) experiments for samples C70/30, C60/40, C40/60, D70/30, D60/40 and D40/60.

Sample	rate constant, [$\cdot 10^3$] k (s^{-1})	exponential factor, n
C70/30	1.633	2.5
C60/40	1.612	2.7
C40/60	1.77	3.0
D70/30	2.64	4.0
D60/40	1.55	4.2
D40/60	2.03	4.6

In addition to a quantitative phase analysis based on the XANES spectra, the extended fine structure (EXAFS) was used to analyze the short-range order structure. Repeated cycles of reduction and re-oxidation at 523 K were investigated by *in situ* EXAFS. A reversible change between copper oxide and reduced copper clusters is evident from the Fourier transformed Cu K edge EXAFS of re-oxidized and re-reduced Cu/ZnO sample (60 mol-% Cu, sample D60/40) (Figure 5.15). Moreover, the increased amplitude of the Cu-Cu nearest neighbor shells (2.4 Å) in

the re-reduced state indicates an increased crystallinity and/or crystallite size. The ZnO FT($\chi(k)$) also reveals an increased intensity of higher Zn-O shells after reduction, which parallels with the increased crystallinity or particle size of the bulk Cu phase. The observation of the increasing amplitude of both Cu and ZnO after reduction implies that ZnO undergoes microstructural modification during reduction and re-oxidation as well and hence may not be a completely inert support.

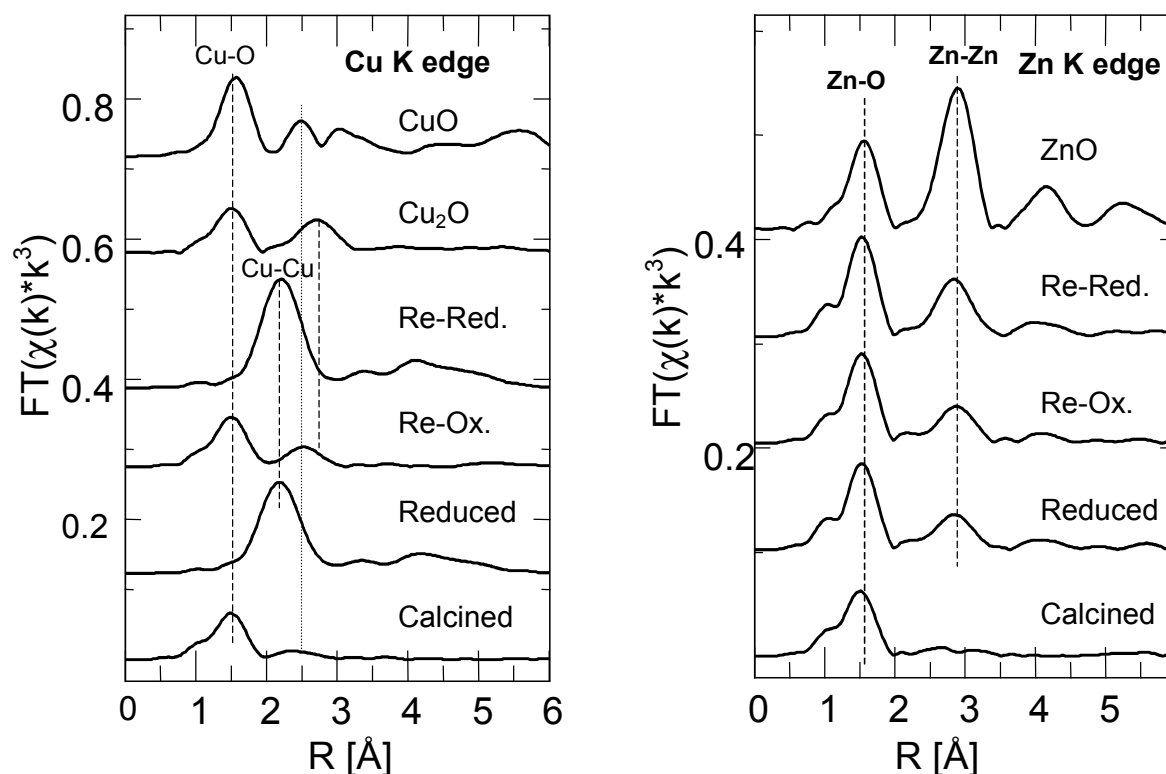


Figure 5.15: Fourier transformed Cu K edge $\chi(k)$ of (a) the oxidized (calcined and re-oxidized (Re-Ox.)) and reduced state (Reduced, Re-Red.) at 523 K together with $\chi(k)$ of CuO, Cu_2O (both at room temperature). (b) Zn K edge FT[$\chi(k)$] of the oxidized and reduced state of the same catalyst sample together with $\chi(k)$ of pure ZnO. Repeated reduction (2 vol-% H_2) and oxidation (15 vol-% O_2) cycles at 523 K of a sample C60/40.

5.3.2 Redox cycles during steam reforming of methanol

In Figure 5.16 the Cu K edge XANES spectra measured over a period of 20 min during oxygen addition to the feed at 523 K is presented. It can be seen that adding O_2 to the feed (15 vol-%) results in an increase of the Cu K pre-edge feature. This corresponds to an oxidation of Cu to CuO.

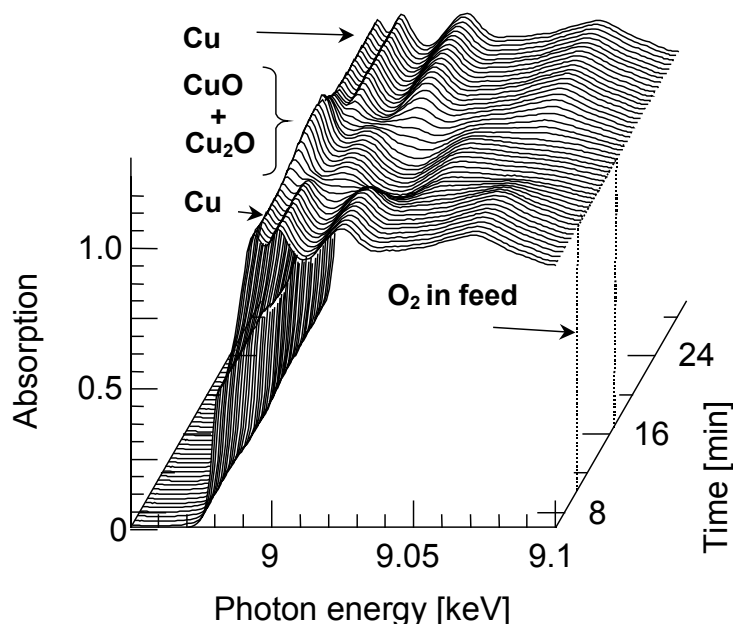


Figure 5.16: Evolution of Cu K-edge XANES of CuO/ZnO at 523 K during oxygen addition to a methanol steam reforming feed ($c(\text{MeOH}) \sim 6$ vol-%, $c(\text{H}_2\text{O}) \sim 1.5$ vol-% in 25 ml/min He). Different Cu phases are indicated.

The evolution of the concentration of MeOH, H_2 , H_2O and CO_2 during two oxygen addition cycles together with traces of methylformate and CO (lower part of the graph) are depicted in Figure 5.17 (a). The variation in activity, selectivity and production rate during the cycle experiment is shown in Figure 5.17 (b). It can be seen that after each oxygen and subsequent reduction cycle the resulting copper phase exhibited an increased activity and selectivity (see Figure 5.17 (b)) compared to the initial values obtained after the first reduction. The catalytic performance after two oxidation/reduction cycles of a number of samples is given in Table 5.3.

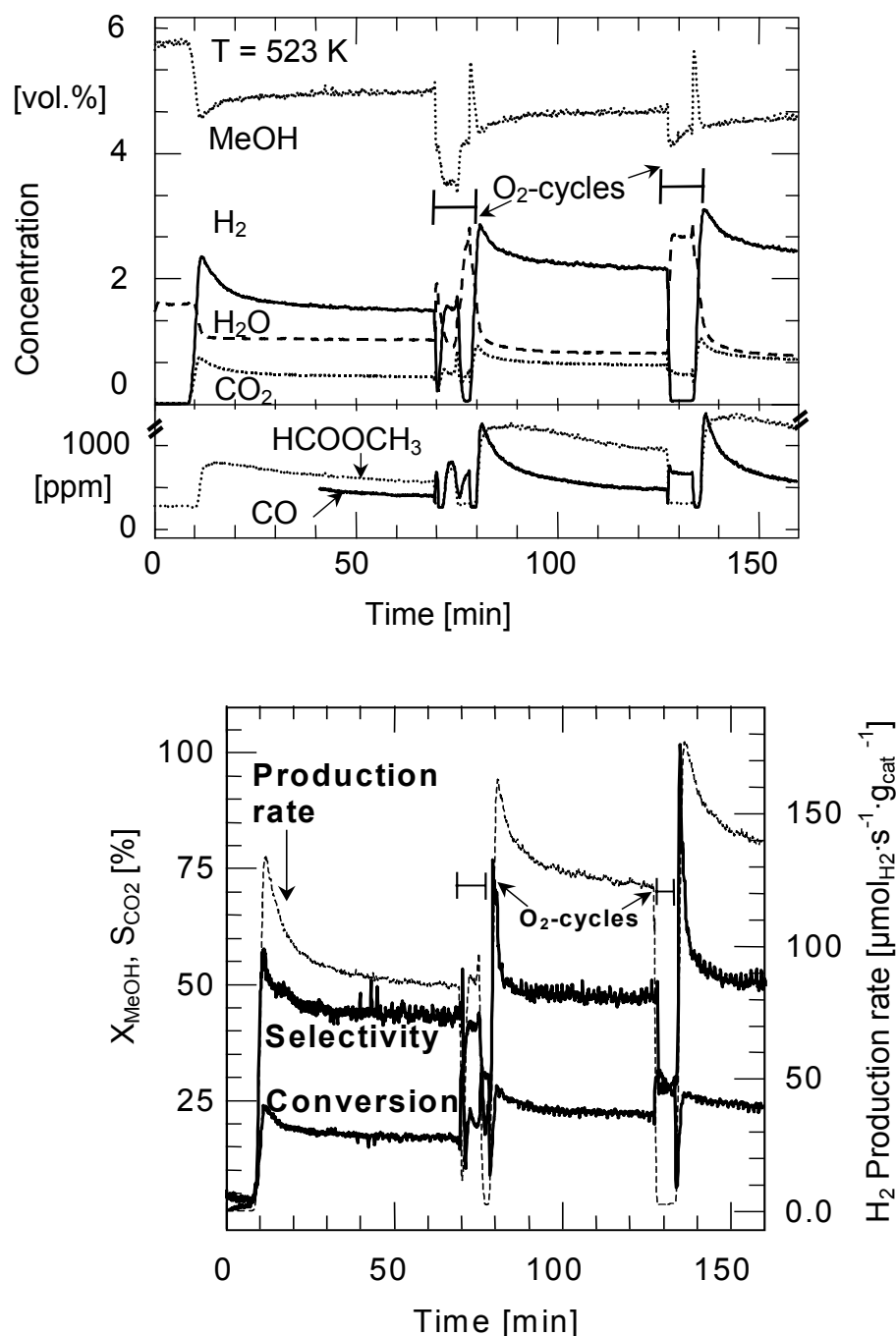


Figure 5.17: (a) Evolution of gas phase composition (H_2 , MeOH, CO_2 , and H_2O) during oxygen addition to a methanol steam reforming feed in the in situ XAFS cell. Concentration of CO and HCOOCH_3 is shown in the bottom part of the graph. (b) Changes in selectivity, conversion, and production rate during oxidation and re-reduction (sample C60/40).

The evolution of the copper bulk phases (*i.e.* formation of CuO_{1-x} and re-reduction) and the corresponding gas phase composition during one oxygen addition to the feed is shown in Figure 5.18. In the bottom part of Figure 5.18 the concentration of CO and methyl formate are shown on a different scale. It can be seen that oxygen in the feed leads to a rapid oxidation of the copper particles to Cu(I) oxide and CuO (with a ratio of $\sim 3/1$). After the O_2 has been switched off the CO and H_2O concentration decrease, whereas the H_2 and CO_2 concentration increase. Furthermore,

after the oxygen is switched off the catalyst is re-reduced in the feed. Apparently, reversible changes of the oxidation state of copper can be observed during oxygen cycles due to oxidation and subsequent re-reduction processes in the feed (see Figure 5.18). A catalytic activity similar to that before the oxidation is regained after 4 min. After that only copper metal can be detected.

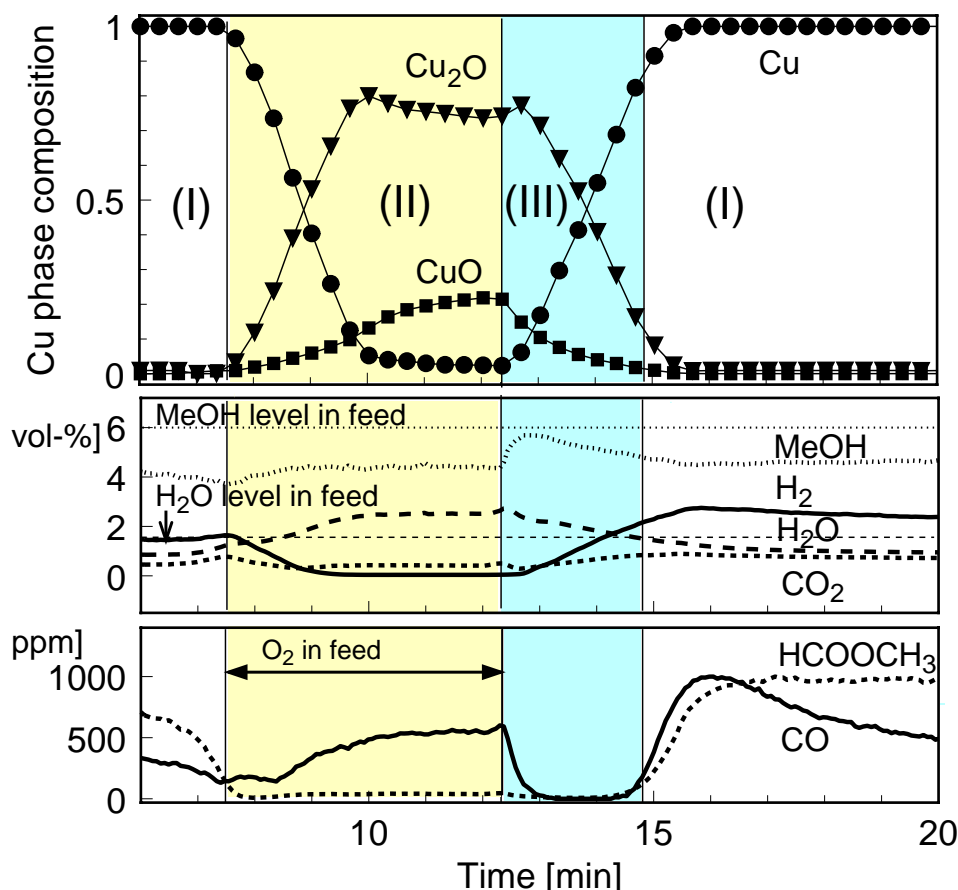


Figure 5.18: Evolution of Cu phase composition during oxygen addition cycles into steam reforming feed at 523 K. Phase analysis was obtained from least-squares fit of reference spectra to the corresponding XANES spectra shown in Figure 5.16. The two lower sections of the graph depict the evolution of the gas phase in percent and ppm, respectively. Three transitions in bulk and gas phase composition are marked: I.) copper metal during steam reforming, II.) oxidation to CuO_{1-x} , III.) re-reduction of CuO_{1-x} phases.

The extended fine structure (EXAFS) of the experimental XAFS spectra measured under reaction conditions at the Cu K and Zn K edge was investigated to analyze changes in the short-range order structure of Cu and ZnO during repeated oxidation and re-reduction at 523 K during methanol steam reforming reaction. In Figure 5.19 a refinement of a theoretical Cu EXAFS function to an experimental Cu FT ($\chi(k)$) of sample C70/30 at 523 K under steam reforming conditions is depicted. Only the four most intense single scattering paths in copper metal are displayed and a good agreement between experimental data and fit can be seen.

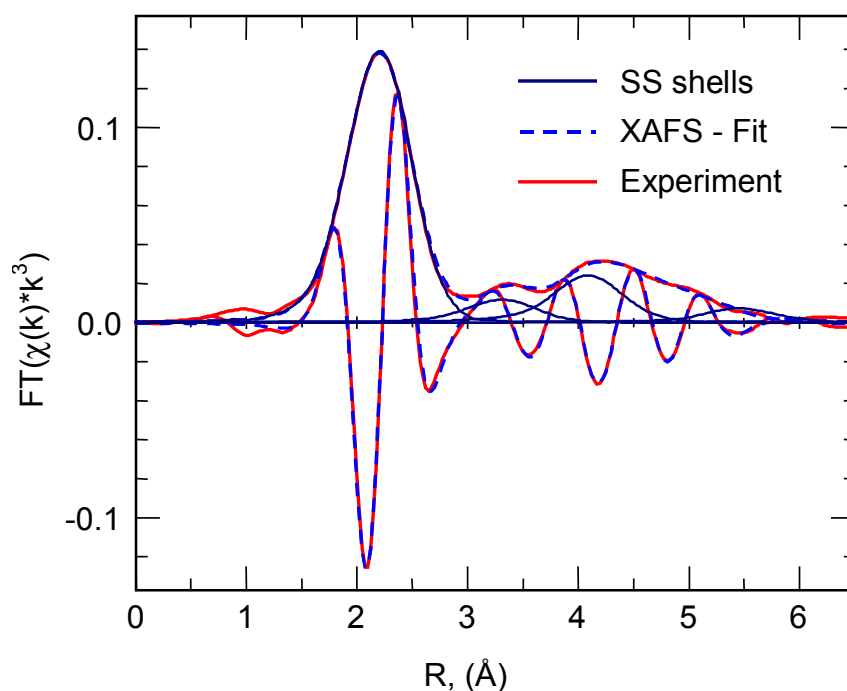


Figure 5.19: Refinement of a sum of theoretical EXAFS function (dashed line) of Cu to an experimental $FT(\chi(k))$ of sample C70/30 at 523 K after reduction in 2 vol-% H_2 . Only the four strongest single scattering EXAFS functions are indicated (thin dark lines). Fitted parameters are found in Table 5.5.

The structural parameters refined are given in Table 5.5. During the fit the coordination numbers of Cu were kept constant to the values of bulk copper. This restriction is a reasonable assumption for the particle sizes investigated which are larger than 80 Å as it was shown by XRD. Therefore, size effects are assumed to play only a minor role for the reduction of the amplitude in the $FT(\chi(k))$ [Clausen00]. However, an EXAFS refinement with the Debye-Waller factor fixed to those of Cu bulk afforded an apparent coordination number of ~ 9 for the first Cu-Cu shell. Here the Debye-Waller (DW) factor is treated as a fitting parameter with coordination numbers fixed to those of the bulk metal. Hence, the Debye-Waller factor accounts for the apparent structural disorder in the copper crystallites and, hence, for the reduction in amplitude in the $FT(\chi(k))$.

In the EXAFS analysis the Debye-Waller factors for the first, second, third and fifth Cu-Cu shells are determined from a refinement of a theoretical EXAFS function to the experimental EXAFS functions of reduced binary samples measured at room temperature and at 523 K (shown in Figure 5.20).

Table 5.5: Structural parameters of Cu/ZnO (C70/30) at 523 K under methanol steam reforming conditions (Figure 5.19) obtained from a refinement of theoretical EXAFS functions calculated for Cu metal cluster ($k = 2.0$ to 13.0 \AA^{-1} , $R = 1.5$ to 6.0 \AA , $N_{\text{ind}} = 32$, $N_{\text{free}} = 12$, 5 single scattering paths and 14 multiple scattering paths). Parameters refined are $E_0(\text{Cu}) = 3.83 \text{ eV}$. The fit residual amounted to 2.8. Based on shells # 1, 2, 3, 5 an average lattice constant of $a_0 = 3.6410 \text{ \AA}$ (Cu, $Fm3m$) was obtained.

Shell	CN _{fixed}	R, (Å)	ΔR_{foil} , (Å)	σ^2 , (Å ²)	w (%)
1. Cu - Cu	12	2.552	- 0.004	0.0158	100
2. Cu - Cu	6	3.647	0.032	0.0246	9.567
3. Cu - Cu	24	4.437	0.01	0.0258	19.86
4. Cu - Cu	12	5.098	0.014	0.0963	0.443
5. Cu - Cu	24	5.826	0.111	0.030	6.187

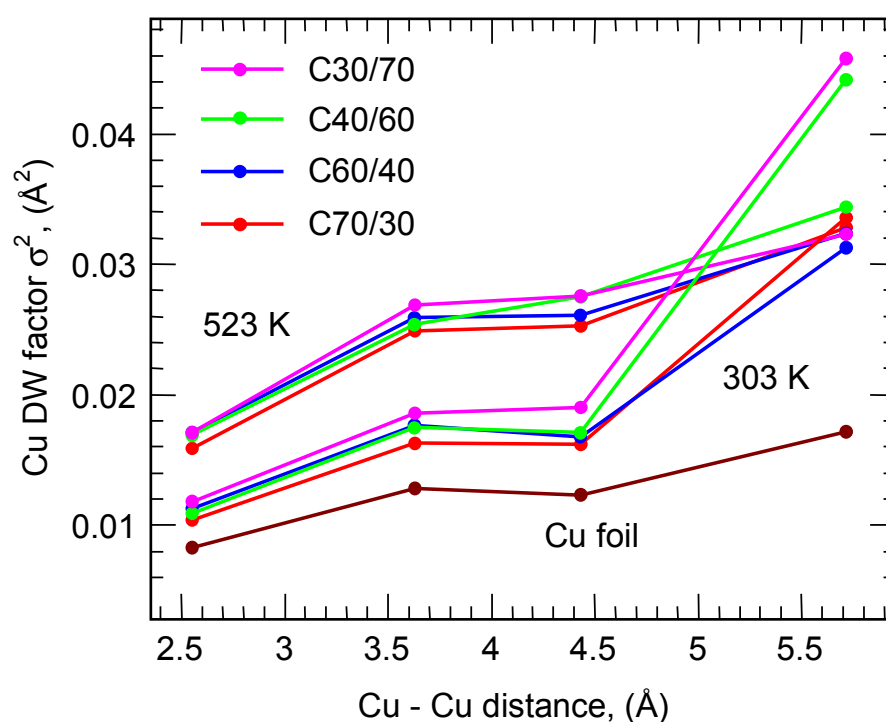


Figure 5.20: Cu Debye-Waller (DW) Factors, σ^2 , for the first, second, third, and fifth Cu-Cu distance obtained from a refinement of a theoretical EXAFS function to experimental data for reduced samples C70/30, C60/40, C40/60, C30/70 and Cu foil obtained at 303 K and 523 K under methanol steam reforming conditions.

For comparison, the DW factors obtained for a copper foil at room temperature are also given. It can be seen that the DW factors for the first three Cu-Cu shells for the samples at 523 K are

higher than for those measured at room temperature. However, conspicuous deviations from this trend are detected for the DW factors of the fifth shell at 5.7 Å for the samples (C70/30, C60/40) measured at 523 K as they are in the same order than that of the samples measured at room temperature. For the samples C40/60 and C30/70 even higher DW factor are determined at room temperature than at 523 K. The DW factors of the Cu foil are the lowest in all cases. In Figure 5.21 the Fourier transformed experimental Cu K edge of sample C70/30 is shown under working conditions at 523 K after different oxidative treatments. As can be seen from Figure 5.21 the oxidation and *re*-reduction cycles lead to an increase in the amplitude of the FT peak indicating structural changes with respect to the fresh reduced catalyst under steam reforming conditions, with a smaller difference in $FT(\chi(k))$ after the first and the second oxidation cycle.

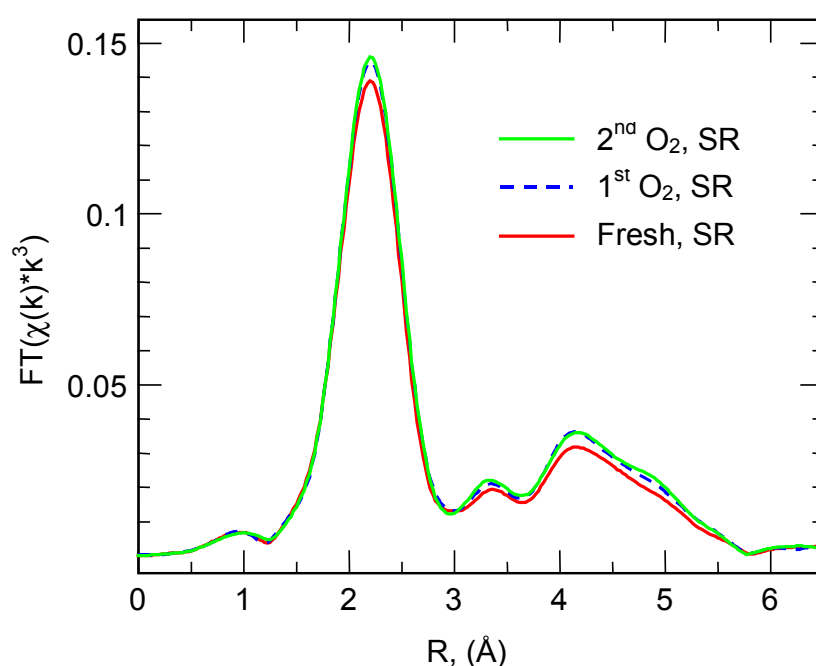


Figure 5.21: Fourier transformed experimental Cu K edge $\chi(k)$ of sample C70/30 under working conditions for methanol steam reforming at 523 K (feed composition: $c(\text{MeOH}) \sim 6 \text{ vol-\%}$, $c(\text{H}_2\text{O}) \sim 1.5 \text{ vol-\%}$ in 25 ml/min He) after initial reduction (fresh reduced) and after two subsequent oxidation and reduction (denoted as first and second oxidation step).

The variation of the Cu DW factors for the first, second, third, and fifth Cu-Cu distance obtained from fitting experimental spectra of samples C70/30 and C60/40 obtained under working conditions at 523 K for different oxidative treatments is displayed in Figure 5.22 a and b. An increasing Debye-Waller factor for the fifth Cu shell is detected for both samples with each oxygen addition cycle. This effect seems to indicate an increasing medium range structural disorder in the copper particles with repeated oxygen addition cycles. Furthermore, changes in the local structural order of ZnO after oxidation/*re*-reduction cycles under reaction conditions was analyzed.

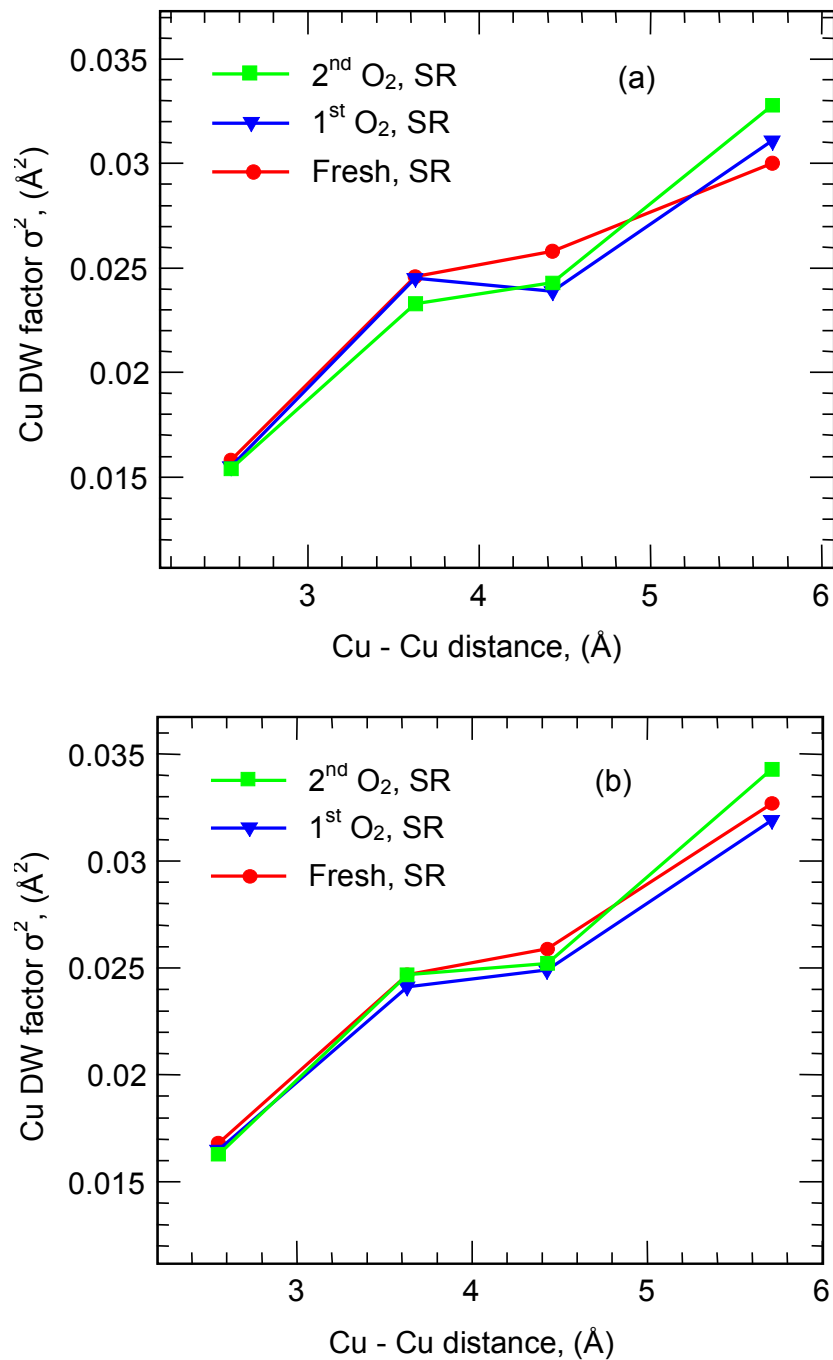


Figure 5.22: Cu Debye-Waller (DW) Factors, σ^2 , for the first, second, third, and fifth Cu-Cu distance obtained from a refinement of a theoretical EXAFS function to experimental data for sample C70/30 (a) and C60/40 (b) obtained at 523 K during methanol steam reforming conditions after different pretreatment (fresh reduced) and after two subsequent oxidation and reduction steps (denoted as 1st O₂, SR and 2nd O₂, SR step).

In Figure 5.23 the evolution of the experimental $\text{FT}(\chi(k))$ of ZnO of the sample C70/30 at 523 K during methanol steam reforming after initial reduction and after two oxidation/re-reduction cycles is depicted. A significant increase in amplitude of the $\text{FT}(\chi(k))$ is clearly detectable with repeated O₂-addition cycles. Especially for the Zn-Zn distance at 2.8 \AA a

continuous increase can be seen. Higher shells also become more developed after repeated oxidation steps. The observation of the increasing amplitude of both Cu and ZnO after oxidation and reduction implies that ZnO undergoes microstructural modification during oxidation/reduction cycles as well.

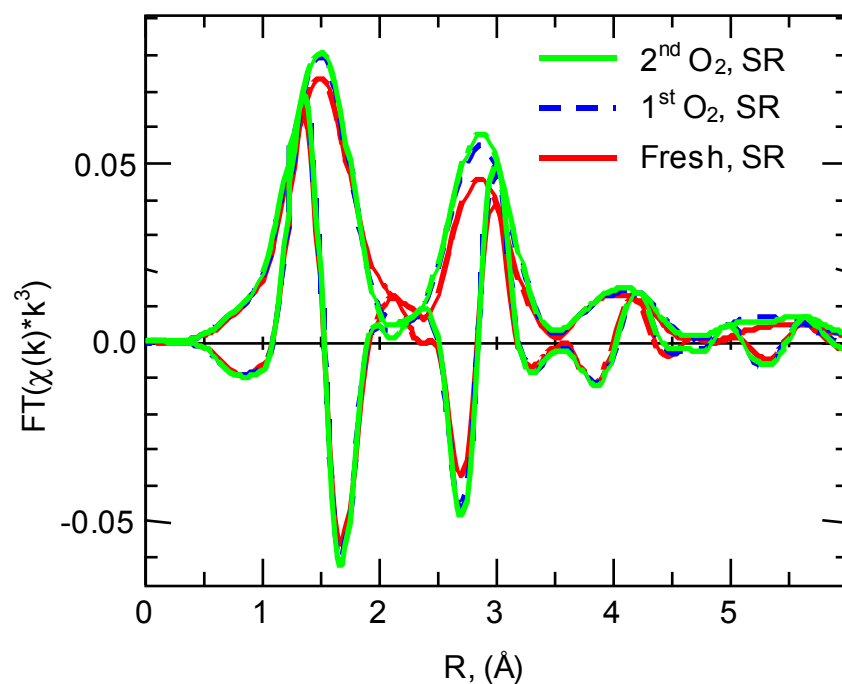


Figure 5.23: Experimental Fourier transformed Zn K edge $\chi(k)$ (magnitude and imaginary part) of ZnO for sample C70/30 obtained at 523 K during methanol steam reforming reaction after different pretreatment (fresh reduced) and after two subsequent oxidation and reduction steps (denoted as 1st O₂, SR and 2nd O₂, SR step).

To further elucidate the structural changes in the short-range order of ZnO after oxidation/reduction cycles, a refinement of theoretical EXAFS functions to the experimental spectra was performed. As an example, Figure 5.24 (a) shows the fit of a theoretical EXAFS function of ZnO to the experimental Zn K FT($\chi(k)$) of sample C70/30 under steam reforming conditions at 523 K. A significant deviation in amplitude and imaginary part of the FT($\chi(k)$) is observed between the experimental and the fitted spectra. However, by adding Zn-Cu shells for Zn atoms occupying Cu sites in Cu clusters a much better fit to the experimental FT is obtained as shown in Figure 5.24 (b). This indicates that Zn in Cu clusters contributes significantly to the FT($\chi(k)$) of ZnO. By quantitative EXAFS-fitting of a sum of the two phases (ZnO + Zn in Cu) it is possible to determine the amount of Zn in the Cu clusters. It was found that a considerable contribution to the total amplitude from scattering paths of Zn in Cu is present for the fresh reduced samples under reaction conditions which amounts to $\sim 10\%$ for the sample C70/30. This amount diminishes to

5.1% after the first oxygen addition cycle and to 2.6 % after the second cycle. By relating the contributions of scattering paths of Zn in Cu to the nominal Zn-content of the samples, the concentration of Zn in Cu can be estimated. For the fresh reduced sample C70/30 4.3 mol-% Zn was found to be dissolved in copper. After two subsequent oxygen addition cycles the concentration of Zn in Cu was 2.2 and 1.1 mol-%, respectively. For the sample C60/40 an amount of 2.4 mol-% is dissolved in the Cu bulk which is reduced to 1.3 mol-% and 0.8 mol-% after two oxygen addition cycles.

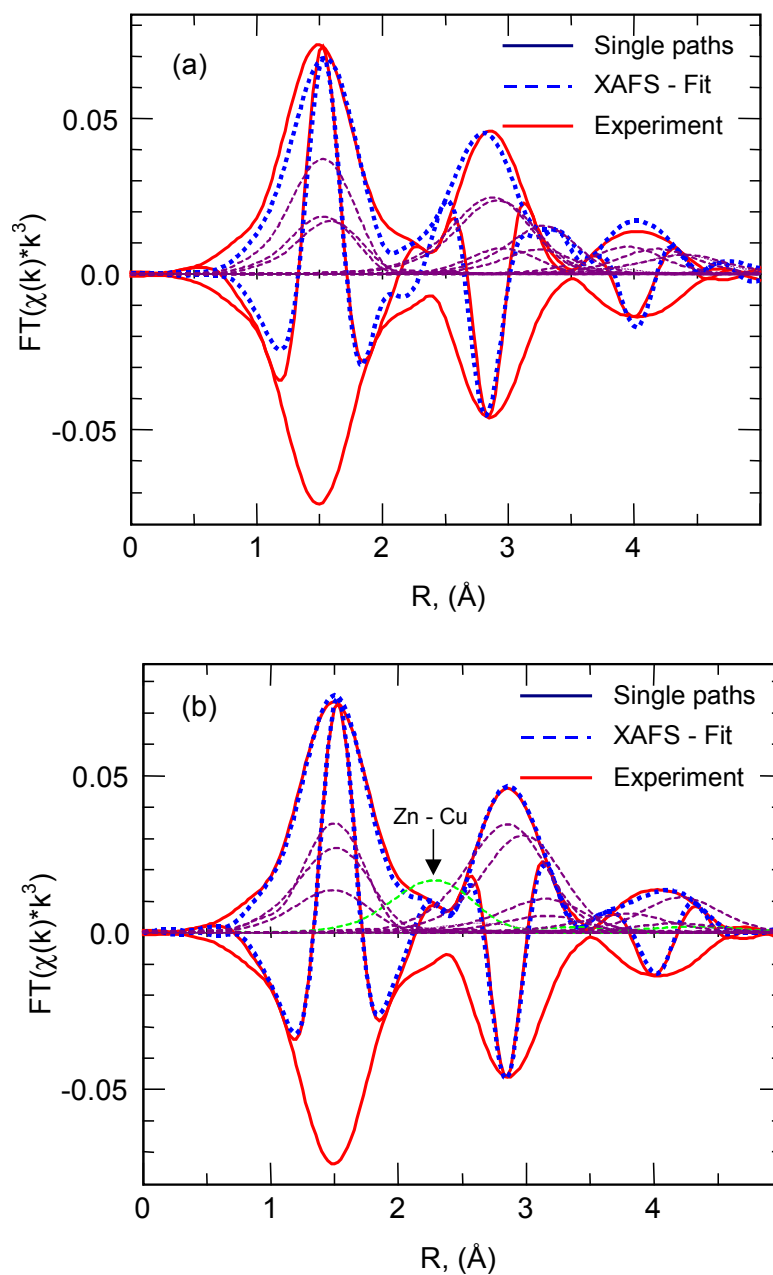


Figure 5.24: Refinement of a theoretical EXAFS function (dotted line) of ZnO to an experimental $FT(\chi(k))$ for the sample C70/30 after reduction in 2 vol-% H_2 at 523 K (a) pure ZnO and (b) assuming additional Zn-Cu shells by doping Zn into the Cu cluster.

5.4 Discussion

5.4.1 In situ XRD

5.4.1.1 *Dependence of reducibility on catalyst composition*

The presence of water retards the reduction onset temperature (~ 10 K) and results in higher Cu crystallite sizes (Figure 5.2). Whereas the Cu/Zn ratio has only a slight effect on the onset temperature the Cu particle size decreases with increasing Zn-content. However, the lower crystallite size for both samples with 70 mol-% Cu (C70/30, D70/30) is an exception to the trend seen in the other samples (Table 5.1). This behavior of the crystallite size of sample 70/30 can be traced back to changes in phase composition of the hydroxycarbonate precursor for this compositional range. It was shown in by Bems *et al.* that for Zn concentrations larger than 40 mol-% the multiphasic phase composition of the hydroxycarbonate precursor shows a transition from the rosasite phase $((\text{Cu,Zn})_2(\text{OH})_2\text{CO}_3)$ to the aurichalcite phase $((\text{Cu,Zn})_5(\text{OH})_6(\text{CO}_3)_2)$ [Bems01]. The influence of the precursor structure which is apparently preserved in the calcined CuO/ZnO precursor can lead to an enhanced reduction rate through the beneficial interaction of various types of defects leading to a better gas phase transport (*e.g.* solid state diffusion) during the reduction. Those defects may be introduced during calcination of the hydroxycarbonate precursor at mild decomposition temperatures affording a high density of defects in the oxide. Furthermore, the nucleation process influences the reduction rate and it can be imagined that the interaction of the Cu metal nucleus with ZnO can lead to differences in the growth in three dimensions. In most cases the addition of water in ‘wet’ reduction experiments caused a shift of the onset of reduction to higher temperatures (Table 5.1). The influence of water addition could be explained by both thermodynamical and kinetic effects. First, the water partial pressures employed for the ‘wet’ TPR (~ 30 mbar) experiments dilutes the hydrogen and results in an increased formation temperature of the Cu phase. Furthermore, the inhibition of the reduction by additional water according to the law of mass action can occur as well. Second, there may be a retarding influence of water on the formation of Cu nuclei. This kinetic explanation has been previously discussed by Wimmers *et al.* for a TPR study of Fe_2O_3 particles under ‘wet’ reduction conditions [Wimmer86].

5.4.1.2 *Effects of precursor preparation and reduction conditions on the catalytic performance*

The influences of the Cu/Zn ratio and the reduction method on the selectivity in methanol steam reforming are discussed for both constant and decreasing pH sample preparation methods.

The MS analysis used for the *in situ* XRD set-up enables to quantify the initial catalytic activity and the time on stream behavior (Figure 5.3). The selectivity to CO₂ for the catalysts tested as a function of the conversion of methanol is shown in Figure 5.4. The ‘wet’ reduced samples C60/40, C50/50, C40/60 and D60/40, D50/50, D40/60 of both sample sets show the same sequence in selectivity (*i.e.* $S_{\text{CO}_2,60/40} > S_{\text{CO}_2,50/50} > S_{\text{CO}_2,40/60}$) with similar absolute values (see also Table 5.3). Selectivities of the ‘dry’ samples are between 10 and 40% lower than those of the ‘wet’ reduced samples. Highest selectivities to CO₂ of ~ 80% at 20% conversion are obtained for the ‘wet’ reduced samples C60/40 and D60/40 (see Figure 5.4). Most samples exhibit an increasing selectivity with decreasing conversion. For instance, the selectivities of samples C50/50 and D50/50 increase from ~70% to ~80% while the conversion drops from 20 to 10%. The reduction procedure affects the catalytic selectivity more clearly than the pH during precipitation of the precursors. This dependence of the selectivity on the reduction conditions is in contrast to the TOF which seems to be unaffected by the reduction treatments of the samples. In addition, the elemental composition has a strong effect on the selectivity. An optimum composition in terms of selectivity is attained for a narrow range of 60 – 70 mol-% Cu for the constant pH samples. The most stable sample is C70/30 ‘wet’ as it shows only small variation in conversion and selectivity.

The *in situ* XRD measurements of Cu/ZnO systems during time on stream indicated that the deactivation with time is correlated to an increase in the apparent Cu crystallite size (Figure 5.7). Hence, the loss of activity is connected to sintering processes and/ or morphological changes of the copper crystallites. ZnO successfully suppresses the sintering of the Cu crystallites and thus the deactivation (sample D60/40). Stabilization of a specific copper crystallite size is crucial to the long-term stability of Cu systems in methanol steam reforming. The fast deactivation has been shown for the pure copper sample D100/0 in Figure 5.3 (b) which lost 70% of its initial activity after 7 h. This confirms previous investigations concerning the function of ZnO to keep the Cu crystallites in a dispersed state and thus maintaining a high surface area as previously described by Chinchén *et al.* and Spencer [Chinchén88], [Spencer99].

It is clear from Figure 5.5 that there is no straightforward correlation of the production rate with the Cu surface area over the entire compositional range of the samples. In addition, it can be seen that although in most cases the ‘wet’ reduction mode results in a higher copper surface area an enhanced production rate is not observed for those samples (*e.g.* samples D40/60, D50/50 and C70/30). In addition, in all cases the D-series samples exhibit a higher activity for a given copper surface area than the C-series samples.

In order to relate differences in performance of the catalyst to effects originating from

preparation parameters, the composition, and the reduction conditions, the production rate is normalized to the Cu metal surface area estimated from the copper XRD crystallite size. The initial TOF for H₂ is a function of the ZnO-content (see Figure 5.6). The TOF values for catalysts with ZnO-contents higher than 40 mol-% Zn do not show the linear increase in TOF. For concentration > 40 mol-% Zn the TOF is independent on the Cu surface area and the values do not differ much as a function of preparation and reduction mode. Furthermore, catalysts prepared at decreasing pH displayed a higher overall TOF than samples prepared at constant pH. This indicates that the precipitation pH affects the activity of the copper in the final catalyst. The influence of the pH during preparation is only seemingly in contrast to the behavior of the selectivity, which showed no dependence on the pH during preparation, because for the determination of the TOF for H₂ all reactions affording hydrogen were taken into account. In addition, ‘wet’ reduction leads to higher TOF-values for the decreasing pH sample batch whereas ‘dry’ reduced constant pH samples exhibit a slightly higher intrinsic activity. The significant deviations from a constant TOF as a function of the composition implies that the copper surface area alone cannot adequately account for the differences in intrinsic activity. The catalyst D60/40 is exceptional as the activity of a copper surface atom can be twice as high for a given elemental composition than that for the sample C60/40 indicating the influence of preparation parameters on the catalytic activity as a function of the pH during preparation (*i.e.* increased TOF) (Figure 5.6).

The absence of a linear relationship between the copper surface area and the methanol-steam reforming activity provides additional evidence that the methanol steam reforming reaction is “structure sensitive”. This behavior is in contrast to the reports of Chinchén *et al.* who described methanol synthesis as a “structure-insensitive” reaction [Chinchén91]. The different behavior in turn suggests that additional parameters beside the Cu metal surface affect the activity. A “structure-sensitivity” was reported by Hadden *et al.* [Hadden95] for the water-gas shift reaction. They have shown that the specific activity is not directly correlated to the Cu metal surface area and concluded that preparation parameters determine to a large extent the activity for a given Cu surface area. In a recent publication by Peppley *et al.* a kinetic model for methanol-steam reforming is presented [Peppley99]. It was found that the methanol steam reforming reaction and the methanol decomposition to CO and hydrogen proceed on different active sites, although the rate-determining step (dehydrogenation of absorbed methoxy groups) is the same in both cases. Furthermore, it was shown that the active site responsible for the methanol steam reforming reaction is similar to the one responsible for the water-gas shift reaction. This type of sites is thought to be formed *in situ* and incorporates the presence of Cu²⁺ aggregates stabilized by hydroxyl and carbonate groups [Andreev95].

The present work indicates that an additional microstructural parameter different from the Cu surface area is operative. This becomes more apparent in the catalytic experiments after oxidation/re-reduction cycles. *In situ* XRD afforded an increase in crystallite size after oxygen addition cycle accompanied by an increase in conversion of methanol and selectivity to CO₂ (Table 5.3). The increase in crystallite size can reach up to ~ 90 % (from 70 Å to 120 Å for the sample C70/30). The origin of this pronounced increase in Cu crystallite size after each oxidation cycle can be related to a structural rearrangement during oxidation and re-reduction (Figure 5.9). Although the increase in Cu particle size results in a loss of Cu surface area (see Figure 5.8), higher conversions and selectivities are observed (Figure 5.10) after oxidation cycles. Combining the activity data for the oxidation cycles shown in Figure 5.10 (sample C60/40) with the Cu crystallite size determined by *in situ* XRD an increase of the TOF as a function of oxidation cycle can be calculated. After the first cycle the TOF increases from 1.1 to 1.5 and after the second cycle the TOF amounts to 1.6 s⁻¹. Again, these observations are in contrast to the simplified correlation of the catalytic activity with the Cu surface area, and, hence, the crystallite size [Peppley99]. A lattice parameter determination by *in situ* XRD yielded a continuous increase of the copper lattice parameter and the ZnO lattice parameter *a* and *c* under methanol steam reforming conditions and with each oxygen addition cycle (Figure 5.11). The evolution of the lattice parameters may originate from the influence of the Cu/ZnO interface which may increase after each oxygen addition cycle increasing the effect of the misfit of the two lattices (see below, XAS discussion). Furthermore, these findings corroborate the assumption that other bulk structural features contribute to the activity as well. In principle, the contribution of strain in the bulk structure should be detectable by analyzing the XRD profile. However, with the experimental set-up used (CuK α_1 - α_2 doublet) a detailed size and strain analysis of the broadened XRD profile using the Voigt function [Langford78] for a peak profile analysis is not easily achievable. However, for extremely broadened X-ray peaks these limitations might be less severe, hence, a qualitative analysis was attempted. Using the Voigt method it is found that in addition to size effects the broadening of the Cu (111) diffraction line is also caused by microstrain in the Cu bulk. For the sample D60/40 a Cu crystallite size of 90 Å was determined while the extent of strain amounted to 0.7 %. After oxidative treatments the growth of the copper crystallites (increased size of 102 Å) was not accompanied by an annealing of defects because a similar strain contributions (0.7 %) to the peak broadening was still present.

Apparently, both, the time on stream and the re-oxidation experiments in the XRD cell show that a high Cu surface area is a prerequisite for an active Cu/ZnO catalyst. However, additional microstructural parameters need to be considered to account for the activity and selectivity

observed. Further evidence for bulk structural changes under reaction conditions were gained from the *in-situ* XAFS experiments.

5.4.2 In situ XAFS

5.4.2.1 Activation of the CuO/ZnO catalyst-TPR

Time-resolved XANES experiments at the Cu K edge indicate that Cu(I) oxide is an intermediate of the reduction of the CuO/ZnO systems studied (Figure 5.12 (a)). In addition, these experiments afforded the evolution of the three phases CuO, Cu, and Cu(I) oxide during temperature-programmed reduction of CuO/ZnO (Figure 5.12 (b), Figure 5.13) not accessible by conventional TPR studies. Previously, features in the TPR spectra of CuO/ZnO system were attributed to different degrees of dispersion of the CuO without taking possible intermediates during the reduction processes into account [Fierro94]. Compared to *in situ* XRD results where the detection of copper metal requires a certain particle size and therefore during TPR appears to be shifted with respect to the evolution of water, XAS can afford complementary information on the early stage of reduction. Apparently, the reducibility of the CuO/ZnO systems (Cu nuclei formation during reduction) depends not only on the Cu/Zn ratio in the catalyst as has been reported before [Fierro94] but also on the preparation conditions of the hydroxycarbonate precursor. Using the Avrami-Erofeev equation the kinetic analysis of the reduction curves of the two sample sets revealed an increasing exponential factor n with increasing Zn-content indicating differences in nucleation rate (Figure 5.16). The increasing exponential factor n can result from a higher dimensionality of growth or an increased number of steps required for the nuclei formation. Taking the Cu crystallite size based on the XRD analysis into account (Figure 5.2), it seems that a slower reduction process results in larger crystallite sizes (e.g. 100 Å for C60/40 compared to 85 Å for C70/30 both after ‘dry’ reduction (Table 5.1)). The lower reducibility of the samples C60/40 and D60/40 compared to that of the samples C70/30 and D70/30 cannot directly be related to differences in crystallite sizes of CuO in the CuO/ZnO precursor as they show a decrease in size with increasing Zn content (see Tab. 2.1). Similar to the discontinuity in Cu crystallite size observed by XRD for the sample CuO/ZnO with 60 mol-% Cu, the XAS experiments indicate that the retarded reduction for these CuO/ZnO samples parallels changes in the phase composition of the hydroxycarbonate precursors (for Zn concentration large than 40 mol-%). This observation supports our interpretation that the influence of the hydroxycarbonate precursor structure is preserved throughout the calcination step and manifests itself in a different reducibility of the CuO/ZnO precursors.

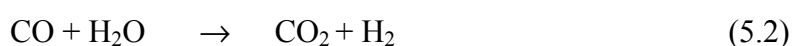
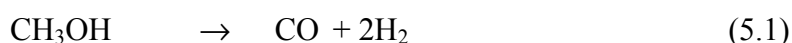
5.4.2.2 Steam Reforming of Methanol

Time-resolved *in situ* XAFS measurement were performed to correlate different copper phases with catalytic activity during oxygen addition cycles to the methanol steam reforming feed (Figure 5.16). The changes in Cu phase composition and the evolution of the gas phase for one oxygen addition cycle are shown in Figure 5.18. After the addition of oxygen, Cu(I) and Cu(II) oxide constitute the major copper bulk phases. In regime III copper metal is formed again which is accompanied by an increasing hydrogen production but no CO and methyl formate is formed in that period. This could imply that the methanol dehydrogenation reaction (eq. 2.18) is favored over Cu in a positive oxidation state (III in Figure 5.18). The formation of CO and methyl formate (ppm levels) originating from methanol steam reforming is observed only after the concentration of metallic copper in the bulk phase exceeds 80 w-% (regime III to I in Figure 5.18). The maximum concentration of CO and methyl formate (1000 ppm) coincides with the complete reduction of the copper phases to Cu metal. Our observation of both methyl formate (HCOOCH₃) and CO in regime I (Figure 5.18) supports the sequence of reaction steps involving dehydrogenation and methylformate formation. During subsequent methanol steam reforming, the CO level is continuously decreasing whereas the concentration of methyl formate remains constant. In this regime (I in Figure 5.18) methanol steam reforming appears to be the predominant reaction. It can be concluded that the changes of bulk phase and gaseous product composition observed during oxygen addition cycles permit to distinguish between different active states of copper operative in the Cu/ZnO system. The results support previous assumption based on kinetic analysis of surface reactions that parallel reaction might occur on different active copper phases during methanol-steam reforming [Peppley99a], [Peppley99b]. Interestingly, the oxidation and reduction curve of Cu metal in the upper graph in Figure 5.18 exhibits in both cases a similar sigmoidal shape for both solid state processes indicating identical rate determining steps and reaction rates.

5.4.3 Mechanistic considerations

Presently two different reaction sequences are discussed to explain the formation of CO during the steam reforming reaction.

Decomposition-shift mechanism:



Dehydrogenation - methylformate route:

According to the decomposition shift mechanism the methanol decomposition to CO and H₂ is followed by the water gas shift reaction which affords CO₂ and hydrogen (see eq. (5.2) and (5.4)) [Amphlett88]. On the other hand Jiang *et al.* and Takahashi *et al.* developed a kinetic model for methanol steam reforming involving several reaction steps. First methylformate is formed by the condensation of methanol (eq. 5.3) which can undergo two different decomposition pathways depending on the nature of active sites on the surface. The hydrolysis to formic acid and methanol is assumed to be assisted by surface hydroxyl groups (eq. 5.4). The formaldehyde then decomposes to CO₂ and hydrogen. Whereas the decarbonylation of methylformate to formic occurs preferentially on metal sites thus affording CO and methanol [Jian93], [Takahashi82], [Peppley99a].

The CO concentration measured during the *in situ* XAFS experiments was found to be lower than 1000 ppm. Based on a methanol decomposition and water-gas-shift mechanism a CO concentration of ~ 4 % is calculated under thermodynamical equilibrium conditions at 523 K with H₂O and methanol concentrations similar to those used in our catalytic experiment [Purnama]. Hence, a simple methanol decomposition mechanism followed by a water gas shift reaction is unlikely to account for the low CO-levels. However, no precise conclusion about the equilibrium attained in the reactor can be made. Our observation of both methyl formate (HCOOCH₃) and CO in regime I (Figure 5.18) supports the assumed sequence of reaction steps involving dehydrogenation and methylformate formation. Considering the different reaction products during the oxygen addition experiments (methanol dehydrogenation and methanol-steam reforming) it remains unclear whether changes in bulk phase composition (Cu oxidation state) directly lead to various reaction paths or reactions occurring in parallel and are of different significance. A further clarification is intended for future investigations.

5.4.4 Implication of microstructural changes of Cu and ZnO on the catalytic activity

The existence of copper suboxides in the bulk during the methanol steam reforming conditions can be excluded within the detection limits of XAFS (~ 1 w-%) in the XANES region. Furthermore, for the Cu EXAFS no additional Cu-O shells were distinguishable after applying the difference file technique in order to extract contributions of oxygen scatters. Nevertheless, the formation of mixed valence copper suboxides at the catalysts surface cannot be excluded. The existence of surface oxygen atoms on copper under methanol oxidation conditions different from well-defined copper oxides has recently been shown by Knop-Gericke *et al.* using surface sensitive *in situ* XAS [Knop00], [Knop00b].

In recent publications the dynamics of the Cu/ZnO system was ascribed to changes in the morphology of the Cu surface. Clausen *et al.* [Ovesen97] observed by EXAFS dynamical changes of the system upon changing the reduction potential in the gaseous environment and ascribed them to changes in the surface morphology (wetting/non-wetting phenomena). They showed that by taking changes in surface area and morphology (*i.e.* formation of Cu(110) and Cu(100) surfaces with higher activity) into account a “dynamic” microkinetic model for the methanol synthesis reaction under different gas atmospheres could be deduced. Sakakini *et al.* [Sakakini00] reported on surface morphology changes of a supported Cu/ZnO/Al₂O₃ catalyst using IR spectra of adsorbed CO. The copper surface termination and the activity in CO₂ decomposition showed a dependence on the reductive treatment after previous oxidation.

In the work presented here microstructural changes of Cu and ZnO upon oxygen addition cycles are correlated to methanol steam reforming activity. The EXAFS refinements to the experimental Cu and ZnO $\chi(k)$ gave ample evidence of the bulk structural interaction of both phases leading to the following structural changes (Figure 5.19, Figure 5.24). The unusual high Debye-Waller factor of the fifth copper shell indicates a medium range structural disorder of the Cu/ZnO at room temperature (Figure 5.20). This structural disorder may be caused by the Cu/ZnO interaction assuming an expansion of the Cu lattice at the interface. An epitaxial orientation of the Cu (111) surface to the ZnO (001) surface has been found to exist in the Cu/ZnO system [Herman80]. Upon increasing the temperature to 523 K the copper lattice will expand more than the ZnO lattice because of the difference in the linear thermal expansion coefficients, α , of Cu ($\alpha_{\text{Cu},500\text{ K}} = 17.4 \cdot 10^{-6} \text{ K}^{-1}$ [Uffelmann30] and ZnO (perpendicular to the c-axis: $\alpha_{\text{ZnO},500\text{ K}} = 71.5 \cdot 10^{-7} \text{ K}^{-1}$ [Ibach69]). At the elevated temperature the thermal expansion of Cu results in a partial release of the lattice mismatch at the interface and, thus, in a reduction of structural

disorder as it can be seen from the decreased or constant DW factors of the fifth Cu shell (Figure 5.21).

In situ EXAFS measurements during oxygen addition cycles under methanol steam reforming conditions gave further evidence of microstructural changes in the Cu/ZnO samples (Figure 5.21, Figure 5.23). The Cu Debye-Waller factors indicated that the medium range disorder for copper particles increased with each oxidation/re-reduction cycle (see Figure 5.22) while the crystallite grow progressively as detected by XRD after each oxygen addition cycle. Upon oxidation/reduction of the Cu particles the increase in the medium range disorder is accompanied by a continuous depletion of Zn incorporated in the Cu clusters (Figure 5.23 and Figure 5.24) (~ 4.3 mol-% for sample C70/30 to 1.3 mol-% for C/0/30 after two cycles). The observed lattice expansion of $< 0.02 \text{ \AA}$ (Figure 5.11) is below the limits for a reliable distance determination by EXAFS. The Zn atoms dissolved in Cu stem from the structural arrangement in the hydroxycarbonate precursor structure and maintain their position in the Cu-matrix under the mild calcination (600 K) and reduction conditions (5 vol-% H_2 at 523 K) used [Bems01]. Apparently, the amount of Zn dissolved in the copper clusters depends not only on the Cu/Zn ratio of the catalyst but also on the structure of the hydroxycarbonate precursor as indicated by the lower Zn-concentration for the more Zn-rich sample C60/40. Moreover, substantial dissolution of Cu into the ZnO matrix ($> 1 \%$) for Zn-rich catalysts as found by Klier *et al.* [Dominiquez83] can be excluded on the basis of the EXAFS results.

Taking these experimental evidence into account it seems reasonable to assume that the enhanced activity after oxidative treatment for methanol steam reforming is closely related to disorder and strain in Cu particles in an analogous manner as it was found for Cu/ZnO catalysts in methanol synthesis. Regarding the role of defects in copper we have recently reported on the implication of the Cu lattice strain of copper clusters in the crystallite size regime 50 – 200 \AA on the methanol synthesis activity [Günter01]. It is suggested that the microstrain modifies the Cu surface and thus contributes to an enhanced methanol synthesis activity. The structural defects of Cu were ascribed to the dissolution of Zn in Cu, incomplete reduction or epitaxial orientation of Cu and ZnO. This concept seems to be transferable to the active copper phase in the methanol steam reforming reaction. Modified Cu surfaces were found to have a promotional effect on the methanol synthesis activity and it appears from our data that for methanol steam reforming a similar structural disorder of the copper bulk also results in a higher activity and selectivity. This is clearly shown by the increase of the TOF after each oxidation cycle indicating a smaller but more active copper surface area. Our results concerning the implication of bulk structural defects in copper on the catalytic activity and their changes after oxidation/re-reduction steps provide a

new bulk structural aspect which adds to the understanding of the arrangement of the active metallic site in copper catalyst.

5.4.5 Model of microstructural changes of Cu and ZnO

The microstructural modifications detected by XAFS and XRD during oxygen addition cycles under working conditions can be summarized by a schematic model given in Figure 5.25. The model shows the structural rearrangement of Cu onto ZnO for a freshly reduced catalyst (a) and a more active catalyst (b) after oxidation and subsequent reduction. For the initially reduced catalyst the small copper particles are in interfacial contact with the supporting ZnO possibly exhibiting an epitaxial orientation. The Cu crystallite size is only slightly lower than that of ZnO and the copper particles exhibit some structural disorder which maybe caused by microstrain originating at the Cu/ZnO interface. Furthermore, a considerable amount of Zn atoms (up to 4.3 mol-%) are incorporated into the Cu clusters, occupying Cu lattice sites and, thus, forming a solid solution of Zn in Cu. Upon oxidation and re-reduction the crystallite sizes of Cu and ZnO increase resulting in a reduced surface area which may be accompanied by an increased interface area between Cu and ZnO.

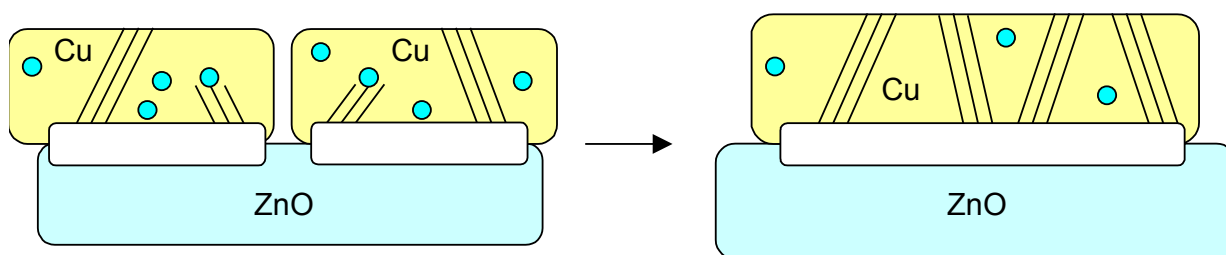


Figure 5.25: Proposed schematic model for copper particles on a ZnO support after initial reduction (a) and after repeated oxygen addition cycles under methanol steam reforming conditions (b). The microstructural modifications upon oxidative treatment result in an increasing crystallite size and a larger interface area between Cu and ZnO. Moreover, the Cu clusters are depleted of Zn accompanied with larger domains of structural disorder (e. g. strain) in Cu (parallel lines).

However, the crystallite growth observed for Cu and ZnO upon re-reduction, is accompanied by an increase of structural disorder in the Cu particles as indicated by the increasing Cu Debye-Waller factors for higher Cu-Cu shells. The re-reduction process leads to a depletion of Zn atoms in the Cu cluster. It seems that the partial segregation of Zn atoms out of the Cu matrix is beneficial for the formation of an improved interface interaction of Cu onto ZnO. It is speculated that the Zn atoms incorporated in the Cu particles annihilate the effect of the Cu/ZnO interface on

the copper cluster and, therefore, the microstrain cannot build up over the entire copper matrix, and, more importantly, does not modify the copper surface. Hence, after oxidation and re-reduction larger domains of distorted and strained copper particles are formed on the ZnO support. ZnO appears to be a crucial component in creating active copper sites (*e.g.* interface interaction, Zn dissolution in Cu particles) and, hence, is much more than an inert support.

Furthermore, we can conclude from the data presented here that the conditions of the reduction process play an important role possibly by adjusting a certain degree of microstrain in Cu during nucleation and growth. In that respect it can be imagined that the amount of Zn-doped into the copper clusters is dependent on the reduction potential and thus directly modifies the extent of strain in the copper matrix. In this study it has been shown that hydrogen reduction with water vapor leads to a more selective catalyst than ‘dry’ reduction. Furthermore, the copper crystallite growth kinetics might also affect the Cu crystallite morphology. Furthermore, with respect to model systems for nanosized Cu/ZnO catalysts, in light of our findings a suitable model system needs to account for the strong support influence of ZnO on Cu and for Zn incorporated in the copper bulk.

5.5 Conclusion

Evolution of bulk phases of Cu/ZnO catalysts under reduction conditions was monitored by *in situ* XRD and XAFS revealing the following:

It was shown that under the temperature programmed reduction conditions employed, CuO of the mixed CuO/ZnO is completely reduced to Cu on ZnO (lower detection limit $\sim 1\%$). From time-resolved *in situ* XAFS experiments at the Cu K edge, Cu(I) oxide was found to be an intermediate of the reduction of CuO/ZnO according to a two step reduction process ($\text{CuO} \rightarrow \text{Cu(I) oxide} \rightarrow \text{Cu}$). The reduction proceeds via a nucleation-grain growth mechanism.

CuO/ZnO precursors which were less easily reduced (high reduction onset temperature) afforded Cu crystallites that are more selective in steam reforming of methanol. This is corroborated by the fact that the ‘wet’ reduction conditions, resulting in a shift of the onset of reduction to higher temperatures, lead to catalysts exhibiting a higher selectivity.

The structure and phase composition of copper-zinc hydroxycarbonate precursor affect the reducibility of the CuO/ZnO precursors and determine the activity of Cu/ZnO catalysts (*e.g.* Zn incorporation in Cu). Therefore preparation parameters of the hydroxycarbonate precursor (*e.g.* pH during precipitation) open up the opportunity to modify the catalyst’s activity.

Structural and catalytic properties were monitored during methanol steam reforming reaction by *in situ* XRD and XAFS and the following conclusions were drawn:

Completely reduced Cu clusters on ZnO constitute the active bulk phase for methanol steam reforming with no further oxidized Cu species detectable ($< 1\%$).

With respect to the composition of the Cu/ZnO samples studied it was observed that with increasing ZnO-content the methanol steam reforming activity increases and a maximum conversion is attained for a narrow compositional range of 60-70 mol-% Cu.

For the EXAFS analysis of Cu clusters on ZnO not only the amplitude reduction due to the cluster size needs to be taken into account but also the presence of defects (Zn) or imperfection (strain) in the Cu bulk.

Upon repeated oxygen addition cycles, the catalyst exhibited an enhanced activity (*i.e.* increased TOF) and selectivity. It was shown by XRD and EXAFS that repeated oxygen addition cycles lead to a crystallite growth of the copper and zinc oxide crystallites accompanied by a segregation of Zn out of the Cu bulk. However, the Debye-Waller factors for higher Cu-Cu shells suggest an increasing structural disorder (*e.g.* strain). The strain is thought to be induced at the Cu/ZnO interface.

ZnO is not just a support but integral part of the active Cu/ZnO catalyst. The bulk structure and, hence, the catalytically active surface is determined by the intimate Cu/ZnO interface.

The microstructural changes of copper and zinc exhibit a positive correlation with methanol steam reforming activity and selectivity. This indicates that a high Cu surface area is a prerequisite for catalytic activity but cannot account for the observed changes in activity and selectivity alone without taking bulk structural changes into account. We conclude that similar to methanol synthesis the enhanced activity in Cu/ZnO catalysts after oxidative treatment for methanol steam reforming is closely related to an increased disorder and microstrain in Cu particles.

In this study it was shown for “real” Cu/ZnO catalysts that solid state transformation and interaction of the Cu and ZnO phases have an pronounced influence on the catalytic activity. Therefore, “ideal” Cu clusters fail to describe the structural imperfection observed and, hence, cannot be expected to be suitable model systems. Apparently, a suitable model system needs to account for both strong Cu/ZnO interface interactions and Zn incorporated in the copper bulk.

6 Summary and Perspectives

This thesis reports on bulk structure – activity correlation of binary Cu/ZnO catalyst in methanol synthesis and methanol steam reforming. X-ray diffraction and X-ray absorption spectroscopy were employed to characterize the microstructural modifications of the catalytic binary copper/zinc oxide catalyst system. The implication of microstructural properties of copper and zinc oxide were accordingly determined on the long-range order as well as the short range order for a large sample set prepared at constant and decreasing pH during coprecipitation. Taking full advantage of the combined XRD and XAS approach as applied throughout this thesis for all intermediate stages of the catalyst formation it has been convincingly demonstrated that only a combination of both methods yield a complete description of the solid state chemical processes occurring during calcination, reduction and under working conditions. In particular, the *in situ* approach using XRD and XAS techniques has been accomplished to elucidate the role of the real structure of the active phase of the Cu/ZnO catalyst system under practical working conditions for methanol steam reforming. This thesis represents a new approach in providing the working principles of a operating catalyst system utilizing *in situ* experiments and thus affording guiding rules for the optimization of existing Cu/ZnO catalyst systems.

The main results of the thesis are summarized in the following:

In chapter 3 the bulk structure of calcined and reduced copper/zinc oxide catalyst was investigated by ex-situ methods. The concept of the single line profile analysis based on the Voigt function for determining microstructural properties of crystalline catalyst materials has been presented. This analysis procedure was successfully applied to the Cu/ZnO catalyst system to extract microstructural parameters (*i.e.* size and strain) for a large number of samples prepared at neutral and decreasing pH with different Cu/Zn ratios. CuO/ZnO precursors with varying molar ratios (100/0 through 0/100) obtained from calcination of hydroxycarbonates prepared under controlled condition of $\text{pH} = 7$ and under decreasing pH conditions were reduced with hydrogen at 523 K and 673 K prior to the XRD investigation. For both phases, Cu and ZnO, a separation of size and strain broadening effects could be performed. The results indicate a mutual structural interaction of both components (copper and zinc oxide) in the sense that strained copper particles are stabilized by the unstrained state of the zinc oxide micro crystallites. The observed structural deformation of Cu in samples with higher ZnO loading can originate, for instance, from epitaxial bonding of the oxide lattice to the copper metal, insufficient reduction or residual carbonate due to incomplete thermal decomposition during reduction.

Both, the crystallite size and the microstrain in Cu and ZnO are dependent on the composition

and thermal treatment. Hydrogen reduction at 673 K leads to a pronounced sintering of the ZnO and afforded a strain release in the ZnO matrix whereas for copper crystallites only small differences in microstrain are detectable. Furthermore, a dimensional anisotropy of the ZnO crystallite shape was observed with the grain growth occurring preferentially along the [001] direction. The Cu crystallites showed only a minor sintering tendency especially at higher ZnO concentrations. Compositional inhomogeneities due to the formation of solid solutions of Zn in Cu and the Cu/ZnO were considered to be the main reason for the observed microstrain

Furthermore, changes in the microstructure of both copper and ZnO (*i.e.* size, strain, and lattice parameter) were found to coincide with changes in phase composition of the hydroxycarbonate precursors (structure of zincian malachite and the transition from the aurichalcite-rich to a Cu containing hydrozincite phase composition). Additional EXAFS measurements at the Cu K and the Zn K edge show that about 5 % ZnO are dissolved in the CuO matrix of the calcined precursors. The formation of ZnO-CuO solid solutions (~ 5 % ZnO in CuO) was detected which may lead after reduction to the formation of Cu-Zn alloy.

The results provide evidence that the microstructural role of ZnO exerted on the reduced copper phase can merely be ascribed to a structural promotion alone. A chemical promotion (*i.e.* dissolution of ZnO in CuO) can be imagined to account for the reported enhanced reducibility and activity for diluted Cu/Zn compositions. However, the origin of this promotion can emerge from the defect bulk structure of both Cu and ZnO and the way these defects, terminating at the surface, may influence the catalytic reaction.

In chapter 4, binary Cu/ZnO catalysts prepared at constant pH with varying molar ratios (90/10 through 10/90) were studied under methanol synthesis conditions at 493 K and at atmospheric pressure. The methanol synthesis activity of the catalysts was correlated to their specific Cu surface area (N_2O reactive frontal chromatography, N_2O RFC) after reduction in 2 vol-% H_2 at 513 K. Activity data were supplemented with a detailed analysis of the microstructure (*i.e.* crystallite size and strain) of the reduced Cu and the ZnO phases after reduction using X-ray diffraction line profile analysis. The estimated copper surface area based on a spherical shape of the copper crystallites is in good agreement with data determined by N_2O RFC. It was found that the production rate of methanol is not a linear function of the specific Cu surface area over the entire Cu/ZnO composition range. A positive correlation of the turn-over frequency for methanol production with the observed microstrain of copper in the Cu/ZnO system. For a compositional range of more than 60 mol-% Zn the strained Cu crystallites expose a Cu surface which is more active than that of a 30 mol-% Zn catalyst. Hence, it is concluded that the phase composition of

the hydroxycarbonate precursor directly influences the active phase of the Cu/ZnO catalyst.

In chapter 5, the bulk structure of copper in various binary Cu/ZnO catalysts for steam reforming of methanol under activation and working conditions is studied by *in situ* X-ray diffraction (XRD) and X-ray absorption spectroscopy (XAS). The evolution of bulk phases from CuO/ZnO precursors during activation with hydrogen was studied using temperature programmed reduction (TPR) (448 – 523 K, 2 vol-% H₂ with and without water vapor). With decreasing copper content the onset of reduction is shifted from 473 K (pure CuO) to 443 K (40 mol-% Cu) accompanied by a decrease in Cu crystallite sizes (from 210 Å to 40 Å). Using time-resolved *in situ* XANES measurements at the Cu K edge during TPR experiments the degree of reduction was monitored. It is shown that Cu₂O forms prior to Cu. The extent of reduction to Cu exhibited a typical nucleation and growth behavior with an enhanced reaction rate for samples with a lower copper content. Adding oxygen to the feed gas leads to the formation of a mixture of Cu(II) and Cu(I) phases accompanied by a complete loss of activity. After switching back to steam reforming conditions a higher activity is attained while the catalyst shows an increased Cu crystallite size (up to 40%). EXAFS measurements at the Cu K and the Zn K edge indicate a structural disorder of the Cu particles (*e.g.* increased Debye-Waller factors) in the medium range order and the dissolution of Zn atoms (up to ~ 4 mol-%) in the copper matrix. Upon oxidation/reduction cycles the disorder in the copper particles increases while Zn segregates out of the copper bulk. A structural model is proposed which ascribes the enhanced activity to structurally disordered (strained) copper particles due to an improved interface interaction with ZnO.

Although the Cu/ZnO catalyst system has been extensively explored in the past this thesis contributes an additional microstructural property, *i.e.* the microstrain, for a better understanding of the implication of bulk structural features on the catalytic activity. Former investigations by the Topsøe group attributed the differences in methanol synthesis activity of ZnO-containing Cu catalysts to changes in the surface termination of copper particles described by a “geometrical factor”. This parameter takes into account an altered copper particle morphology resulting in different exposed facets [Ovesen97]. However, the significance of the defective microstructure of binary Cu/ZnO catalysts for their catalytic activity in methanol synthesis and methanol steam reforming was hitherto not experimentally proven for Cu/ZnO catalysts. The degree of microstructural disorder of copper crystallites exhibits a positive correlation with the turnover frequency for methanol synthesis. A similar correlation also holds for an enhanced activity in Cu/ZnO catalysts for methanol steam reforming after oxidative treatment for methanol steam reforming which is followed by an increased disorder and microstrain in Cu particles. The results concerning the implication of bulk structural defects in copper on the catalytic activity and their

changes after oxidation/re-reduction steps provide a new bulk structural property which adds to the understanding of the nature of the active metallic site in Cu/ZnO catalyst. Both experimental techniques employed, XRD and XAS, identified a strained and disordered copper microstructure that is beneficial for a higher intrinsic activity in methanol synthesis and methanol steam reforming.

The observed increase in activity for strained and defective copper particles are considered to be a consequence of a modification of the surface properties and the structure sensitivity of the reactions investigated. The results have convincingly shown that solid state reactions and in particular the strong Cu/ZnO interface interaction are responsible for the formation of the defect structure and have to be taken into consideration. Thus, for the first time experimental evidence was provided, that beside the copper surface area also bulk structural properties can influence the reactivity of a Cu/ZnO catalyst. The origin of the ‘synergistic’ effects in the Cu/ZnO system could be related to the microstructural properties originating from solid-state interaction in the Cu/ZnO system. Moreover, the role of ZnO has been found to be much more than an inert support, Zn appears to be a crucial component in modifying the microstructure (*e.g.* interface interaction, Zn incorporation in Cu particles), and thus the activity of the copper. In that respect, the binary Cu/ZnO system proved to be a realistic model system which incorporated all bulk structural characteristics (*i.e.* solid state transformation and interaction of the Cu and ZnO phases) that contribute to the observed changes in bulk-structure-activity. This could be regarded as an approach in bridging the gap between the technical catalysts and ideal model systems using a suitable model system with a reduced structural complexity.

A new target structure of an active Cu/ZnO catalyst has been identified which is in close relationship with the hydroxycarbonate precursor phase composition. Hence, this result opens up the opportunity to optimize the microstructure of the copper particles by an appropriate choice of the preparation parameters for the hydroxycarbonate in such a way that a more active copper surface area results. Therefore, much emphasis is put on the wet-chemical preparation process of the catalyst which appears to be a key component for a rational strategy for developing more efficient heterogeneous catalysts. Based on these results it seems feasible to transfer the given working principle of the binary Cu/ZnO catalyst to the industrially important ternary Cu/ZnO/Al₂O₃-system. Further investigation will include the application of alternative supporting materials (*e.g.* mesoporous ZrO₂) which can host the copper particles in order to validate the qualitative rules of strained and defective Cu particles.

In addition to the precursor chemistry, further research has to focus on the solid state processes

occurring during the calcination and reduction procedure of the precursor because it has been shown in this thesis that the solid state chemistry during thermal decomposition and the reduction process develops the microstructural arrangement of the Cu and ZnO crystallites by a variety of processes (*e.g.* nucleation and growth, reduction, diffusion, sintering, etc.), which is pre-determined by the wet chemical part of the preparation route (*e.g.* precipitation, ageing, washing and drying).

7 Literature

- [Als-Nielsen95] Als-Nielsen, J., Grübel, G., and Clausen, B.S., *Nucl. Instr. and Meth. in Phys. Res.*, **B97** (1995) 522.
- [Amphlett85] Amphlett, J.C., Evans, M.J., Weir, R.D., *Cand. J. Chem. Eng.*, **63** (1985) 605.
- [Amphlett88] Amphlett, J.C., Mann, R.F., and Weir, R.D., *Cand. J. Chem. Eng.*, **66** (1988) 950.
- [Amphlett94] Amphlett, J.C., Creber, K.A.M., Davies, J.M., Mann, R.F., Peppley, B.A., and Stokes, D.M., *Int. J. Hydrogen Energy*, **19** (1994) 131.
- [Anderson85] Anderson, J.R., and Pratt, K.C., *Introduction to characterization and testing of catalysts*, Academic Press (1985).
- [Andreev95] Andreev, A.A., Kalchev, M.G., Christov, G.D., and Andreeva, D.Ch., *Kinet. Katal.*, **36** (1995) 828.
- [Arnukavalli93] Arnukavalli, T., Kulkarni, G.U., and Rao, C.N.R., *Catal. Lett.*, **20** (1993) 259.
- [Audebrand98] Audebrand, N., Auffrédic, J.-P., and Louër, D., *Chem. Mater.*, **10** (1998) 2450.
- [Balzar96] Balzar, and Popovic, D., *J. Appl. Cryst.*, **29** (1996) 16.
- [Bao94] Bao, X., Muhler, M., Schedel-Niedrig, T., Schlögl, R., *Phys. Rev. B*, **54** (1994) 2249.
- [Bems01] Bems, B., *PhD Thesis*, Berlin, Technical University, (2001).
- [Boudart85] Boudart, M., *Chem. Rev.*, **5** (1995) 661.
- [Bragg13] Bragg, W.H., and Bragg, W.L., *Proc. Roy. Soc. London (A)*, **88** (1913) 428.
- [Breen99a] Breen, J.P., and Ross, J.R.H., *Cat. Today*, **51** (1999) 521.
- [Breen99] Breen, J.P., Meunier, F.C., and Ross, J.R., *Chem. Commun.*, (1999) 2247.
- [Bunker83] Bunker, G., *Nucl. Instrum. Methods*, **207** (1983) 437.
- [Burch90] Burch, R., Golunski, and Spencer, M.S., *J. Chem. Soc. Faraday Trans.*, **86** (1990) 2683.
- [Burch90b] Burch, R., Golunski, S.E., and Spencer, M.S., *Catal. Lett.*, **6** (1990) 155.
- [Chinchen91] Chinchen, G.C., and Spencer, M.S., *Catal. Today*, **10** (1991) 293.

- [Chinchen86] Chinchen, G.C., Waugh, K.C., *Appl. Cat.*, **25** (1986) 101.
- [Chinchen87] Chinchen, G.C., Hay, C.M., Vanderwell, H.D., and Waugh, K.C., *J. Catal.*, **103** (1987) 79.
- [Chinchen88] Chinchen, G.C., Denny, P.J., Jennings, J.R., Spencer, M.S., and Waugh, K.C., *Appl. Cat.*, **36** (1988) 1.
- [Christmann91] Christmann, K., *Introduction to Surface Physical Chemistry*, Darmstadt, Steinkopff, (1991).
- [Clausen91] Clausen, B.S., Steffensen, G., Fabius, B., Villadsen, J., Feidenshans'l, R., and Topsøe, H., *J. Catal.*, **132** (1991) 524.
- [Clausen94] Clausen, B.S., Schiøtz, J., Gråbæk, L., Ovesen, C.V., Jacobsen, K.W., Nørskov, J.K., and Topsøe, H., *Topic. Catal.*, **1** (1994) 367.
- [Clausen98] Clausen, B.S., *Cat. Today*, **39** (1998) 293.
- [Clausen98b] Clausen, B.S., Topsøe, H., and Frahm, R., *Adv. Catal.*, **42** (1998) 315.
- [Clausen00] Clausen, B.S., and Nørskov, J.K., *Topic Catal.*, **10** (2000) 221.
- [Couves91] Couves, J.W., Thomas, J.M., Waller, D., Jones, R.H., Dent, A.J., Derbyshire, G.E., and Greaves, G.N., *Nature*, **354** (1991) 465.
- [CRC99] D.R. Lide and H.P.R. Frederikse, *The CRC handbook of chemistry and physics*, 80 Boca Raton, CRC, (1999).
- [Delannay84] Delannay, F., ed.: Delannay, F.: *Characterization of Heterogeneous Catalyst*, New York, Marcel Dekker, (1984).
- [Delhez82] Delhez, R., de Keijser, Th.H., and Mittermeijer, E.J., *Fresenius Z. Anal. Chem.*, **312** (1982) 1.
- [Delhez92] Delhez, R., de Keijser, T.H., Mittermeijer, E.J., van Berkum, J.G.M., Sonneveld, E.J., and Vermeulen, A.C., ed.: Hank, V.: *Proceedings of the 3rd European Conference on Residual Stresses*, Frankfurt, (1992) 49.
- [Delorme58] Delorme, C., *Soc. Franc. Mineral.*, **81** (1958) 19.
- [Dominiquez83] Dominiquez, J.M., Simmons, G.W., and Klier, K., *J. Mol. Catal.*, **20** (1983) 369.
- [Ertl97] Ertl, G., Knözinger, H., Weitkamp, J (Eds.), *Handbook of Heterogeneous Catalysis*,

- Weinheim, Wiley-VCH, (1997).
- [Fernández98] Fernández-García, M., Rodríguez-Ramos, I., Ferreira-Aparicio, P., and Guerro-Ruiz, A., *J. Catal.*, **178** (1998) 253.
- [Fierro94] Fierro, G., Lo Jacono, M., Inversi, M., Porta, Lavechia, R., and Cioci, F., *J. Catal.*, **148** (1994) 709.
- [Fierro96] Fierro, G., Lo Jacono, Inversi, M., Porta, P., Cioci, F., and Lavecchia, R., *Appl. Catal. A.*, **137** (1996) 327.
- [Frost88] Frost, J.C., *Nature*, **334** (1988) 577.
- [Fujitani98] Fujitani, T. and Nakamara, J., *Catal. Lett.*, **56** (1998) 119.
- [Fujitani00] Fujitani, T., Nakamura, J., *Appl. Cat. A*, **191** (2000) 111.
- [Gillmann62] Gilman, J.J., *Mechanical behavior of materials at elevated temperature*, New York, McGraw-Hill, (1962).
- [Grunwaldt00] Grunwaldt, J.-D., Molenbroek, A. M., Topsøe, N.-Y., Topsøe, H., and Clausen, B.S., *J. Catal.*, **194** (2000) 452.
- [Günter01] Günter, M.M., Ressler, T., Bems, B., Büscher, C., Genger, T., Hinrichsen, O., Muhler, M., and Schlögl, R., *Cat. Lett.*, **71** (2001) 37.
- [Hadden95] Hadden, R.A., Lambert, P.J., and Ranson, C., *Appl. Catal.*, **122** (1995) L1.
- [Herman80] Herman, R.G., Simmons, G.W., and Klier, K., *Proc. of the 7th Cong. on Cat.*, (1980) 475.
- [Himelfarb83] Himelfarb, P.B., Wawner Jr., F. E., Bieser Jr., A., and Vines, S. N., *J. Catal.*, **83** (1983) 469.
- [Hinrichsen00] Hinrichsen, O., Genger, T., and Muhler, M., *Chem.-Ing.-Tech.*, **72** (2000) 94.
- [Ibach69] Ibach, H., *Phys. Status Solidi*, **33** (1969) 257.
- [Idem96] Idem, R.O., and Bakhshi, N.N., *Can. J. Chem. Eng.*, **74** (1996) 288.
- [Jenkins96] Jenkins, R., and Snyder, R.L., Introduction to X-ray Powder Diffractometry. ed.: Winefordner, J.D.: *Chemical Analysis*, volume 138. New York, John Wiley, (1996).
- [Jian93] Jiang, C.J., Trimm, D.L., and Wainwright, M.S., *Appl. Cat. A.*, **93** (1993) 245.
- [Jian99] Jiang, H.G., Rühle, M., Lavernia, E.J., *J. Mater. Res.*, **14** (1999) 549.

- [Joyner90] Joyner, R.W., *Catal. Lett.*, **6** (1990) 151.
- [Kampshoff94] Kampshoff, E., Hahn, E., and Kern, K., *Phys. Rev. Lett.*, **73** (1994) 704.
- [Kau89] Kau, L.-S., Hodgson, K.O., Solomon, E.I., *J. Am. Chem. Soc.*, **111** (1989) 7103.
- [Keijser82] de Keijser, Th.H., Langford, J.I., Mittermeijer, E.J., and Vogels, A.P.B., *J. Appl. Cryst.*, **15** (1982) 308.
- [Klier82] Klier, K., *Adv. Catal.*, **31** (1982) 243.
- [Klier84] Klier, K., *Appl. Surf. Sci.*, **19** (1984).
- [Knop00] Knop-Gericke, A., Hävecker, M., Schedel-Niedrig, T., and Schlögl, R., *Cat. Lett.*, **66** (2000) 215.
- [Knop00b] Knop-Gericke, A., Hävecker, M., Schedel-Niedrig, T., and Schlögl, R., *Top. Catal.*, **10** (2000) 187.
- [Koningsberger88] Koningsberger, D.C., and Prins, R., X-ray absorption spectroscopy. *Chemical Analysis*, volume 92. New York, Wiley, (1988).
- [Koningsberger00] Koningsberger, D.C., Mojet, B.L., van Dorssen, G.E., and Ramaker, D.E., *Top. Catal.*, **143** (2000) 10.
- [Kraus99] Kraus, W., and Nolze, G., PowderCell v2.2, Bundesanstalt für Materialprüfung Berlin, (1999).
- [Krill98] Krill, C.E., and Birringer, R., *Phil. Mag. A*, **77** (1998) 621.
- [Langford92] Langford, J.I., ed.: Prince, E.: *Accuracy in Powder Diffraction*, NBS, Spec. Pub., volume 846. Gaithersburg, MD, U.S. Department of Commerce, (1992) 110.
- [Langford78] Langford, J.I., *Appl. Cryst.*, **11** (1978) 10.
- [Langford88] Langford, J.I., Delhez, R., de Keijser, Th.H., and Mittermeijer, E.J., *Austr. J. Phys.*, **41** (1988) 173.
- [Laue13] Laue, M., *Physik Z.*, **14** (1913) 1075.
- [Li96] Li, J.L., and Inui, T., *Appl. Catal. A*, **137** (1996) 105.
- [Matyi87] Matyi, R.J., Schwartz, L.H., and Butt, J.B., *Catal. Rev.-Sci. Eng.*, **29** (1987) 41.
- [Mavrikakis98] Mavrikakis, M., Hammer, B., and Nørskov, J.K., *Phys. Rev. Lett.*, **81(13)** (1998) 2819.

- [Nakamura96] Nakamura, I., Nakamura, I., Uchijima, T., Wantanabe, T., and Fujitani, T., *Stud. Surf.*, **101** (1996) 1389.
- [Ovesen97] Ovesen, C.V., Clausen, B.S., Schiøtz, P., Topsøe, H., and Nørskov, J.K., *J. Catal.*, **168** (1997) 133.
- [Peppley99a] Peppley, B.A., Amphlett, J.C., Kearns, L.M., and Mann, R.F., *Appl. Catal. A*, **179** (1999) 31.
- [Peppley99b] Peppley, B.A., Amphlett, J.C., Kearns, L.M., and Mann, R.F., *Appl. Cat. A*, **179** 1999, 21.
- [Peters00] Peters, R., Dusterwald, H.G., and Hohlbein, B., *J. Power Sources*, **86** (2000) 507.
- [Plewa89] Plewa, J., and Skrzypek, J., *Chem. Eng. Sci.*, **44** (1989) 2817.
- [Porta89] Porta, P., Dragone, R., Lo Jacono, M., and Minelli, G., and Moretti, G., *Solid State Ionics*, **32/33** (1989) 1010.
- [Purnama] *personal communication*.
- [Rao63] Rao, S.S., and Anantharaman, T.R., *Cur. Sci.*, **32** (1963) 262.
- [Rasmussen87] B.S. Rasmussen, P.E.H. Nielsen, J. Villadsen, and Hansen, ed.: Delmon, B., Grange, P., Jacobs, P.A., and Poncelet, G.: *Preparation of Catalysts*, volume IV. Amsterdam, Elsevier, (1987) 785.
- [Rasmussen94] Rasmussen, P.B., Homblad, P.M., Askaard, T., Ovesen, C.V., Stoltze, P., Nørskov, J.K., and Chorkendorf, I., *J. Catal.*, **161** (1994) 373.
- [Rehr92] Rehr, J.J., Albers, R.C., and Zabinsky, *Phys. Rev. Lett.*, **69** (1992) 3397.
- [Rehr94] Rehr, J.J., Booth, C.H., Bridges, F., Zabinsky, S.I., *Phys. Rev. B*, **49** (1994) 12347.
- [Reitz01] Reitz, T.L., Lee, P.L., Czaplewski, K.F., Lang, J.C., Poop, K.E., and Kung, H.H., *J. Catal.*, **199** (2001) 193.
- [Ressler98] Ressler, T., *J. Sych. Rad.*, **5** (1998) 118.
- [Ressler99] Ressler, T., Brock, S.L., Wong, J., and Suib, S.L., *Phys. Chem. B*, **103** (1999) 6407.
- [Ressler00] Ressler, T., Wong, J., Roos, J., and Smith, I.L., *Environ. Sci. Technol.*, **34** (2000) 950.
- [Ressler01] Ressler, T., Wienold, J., Jentoft, R.E., and Günter, M.M., *Top. Catal.*, *submitted* (2001).

- [Roberts86] Roberts, A.C., *Powder Diffraction*, **1** (1986) 1.
- [Ruggeri82] Ruggeri, O., Trifirò, F., and Vaccari, A., *J. Solid State Chem.*, **42** (1982) 120.
- [Sakakiniakakini00] Sakakini, B.H., Tabatabaei, Watson, M.J., and Waugh, K.C., *J. Mol. Catal. A.*, **162** (2000) 297.
- [Sankar86] Sankar, G., Vasudevan, S., and Rao, C.N.R., *J. Chem. Phys.*, **85** (1986) 2291.
- [Sankar00] Sankar, G., Thomas, J.M., and Catlow, C.R.A., *Top. Catal.*, **10** (2000) 255.
- [Santra99] Santra, K., Chatterjee, P., and Sen Gupta, S.P., *Sol. Energy. Mater.*, **57** (1999) 345.
- [Sayers71] Sayers, D.E., Stern, E.A., and Lytle, F.W., *Phys. Rev. Lett.*, **27** (1971) 1204.
- [Schlögl93] Schlögl, R., *Angew. Chem.*, **105** (1993) 402.
- [Shen97] Shen, G.C., Fujita, S., Matsumoto, S., and Takezawa, N., *J. Mol. Cat. Al*, **124** (1997) 123.
- [Skrzypek94] Skrzypek, J., Sloczynski, J., and Ledakowicz, S., *Methanol synthesis*, Warsaw, Scientific Publishers, (1994).
- [Snyder93] Snyder, R.L., ed.: Young, R.A.: *The Rietveld Method*, Monographs on Crystallography 5. Oxford University Press, (1993).
- [Somorjai94] Somorjai, G.A., *Introduction to surface chemistry and catalysis*, New York, Wiley, (1994).
- [Spencer99] Spencer, M.S., *Top. Catal.*, **8** (1999) 259.
- [Stern70] Stern, E.A., Lytle, F.W., and Stern, E.A., *Adv. X-ray Anal.*, **13** 1970, 248.
- [Stirling] Stirling, D., Stone, F.S., and Spencer, M.S., *New Frontiers in Catalysis, Proceeding of the 10th International Congress on Catalysis*, volume 10. Budapest.
- [Stokes48] Stokes, A.R., *Phys. Soc. London*, **61** (1948) 382.
- [Swanson53] Swanson, H.E., and Tatge, E., *Natl. Bur. Stand. (U.S.)*, **539** (1953) 15.
- [Takahashi82] Takahashi, K., Takezawa, N., and Kobayashi, H., *Appl. Cat.*, **2** (1982) 363.
- [Topsøe99] Topsøe, N.-Y., and Topsøe, H., *Top. Catal.*, **8** (1999) 267.
- [Uffelmann30] Uffelmann, L., *Phil. Mag.*, **7** (930) 633.
- [Vaarkamp97] Vaarkamp, M., and Konigsberger, D.C., ed.: Ertl, G., Knözinger, H., Weitkamp, J.:

-
- Handbook of Heterogeneous Catalysis*, Weinheim, Wiley-VCH, 1997.
- [Vlaic85] Vlaic, G., Bart, J.C.J., Cavigiolo, W., Pinazola, B., and Mobilio, S., *J. Catal.*, **96** (1985) 314.
- [Vong90] Vong, M.S.W., Sermon, P.A., and Grant, K., *Cat. Lett.*, **4** (1990) 15.
- [Warren69] Warren, B.E., *X-ray diffraction*, Reading (Mass.), Addison-Wesley, 1969.
- [Warren50] Warren, B.E., and Averbach, B.L., *J. Appl. Phys.*, **21** (1950) 595.
- [Wild00] de Wild, P.J., and Verhaak, M.J.F.M., *Catal. Today*, **60** (2000) 3.
- [Williamson53] Williamson, G.K., and Hall, W.H., *Acta Metall*, **1** (1953) 22.
- [Wilson63] Wilson, A.J.C., *Mathematical theory of X-ray crystallography*, Eindhoven, Centrex, (1963).
- [Wimmer86] Wimmer, O.J., Arnoldy, P., and Moulijn, J.A., *J. Phy. Chem.*, **90** (1986) 1331.

8 Appendix

8.1 List of abbreviation and symbols

Abbreviations:

BET	Brunauer-Emmet-Teller
CN	Coordination number
DW	Debye-Waller-type Factor
EXAFS	Extended X-ray absorption fine structure
fcc	face centered cubic
FT	Fourier Transform
FTIR	Fourier transform IR
FWHM	Full width at half maximum
RT	Room temperature
STM	Scanning transmission electron microscopy
TEM	Transmission electron microscopy
TOF	Turn over frequency
TPR	Temperature programmed reduction
XANES	X-ray absorption near edge structure
XAS	X-ray absorption spectroscopy
XRD	X-ray diffraction

Symbols:

σ_j^2	relative mean square disorder between the absorber and an atom (Debye-Waller factor)
λ	mean free path of the photoelectron
$\chi(k)$	EXAFS-function
β_G	integral breadth of Gaussian function
hkl	<i>Miller</i> indices

$\phi_j(k)$	phase shift due to the atomic potentials
β_L	integral breadth of Lorentzian function
a	cubic lattice constant
d_{hkl}	spacing of hkl lattice plane
D_V	crystallite size based on Voigt deconvolution
e	microstrain based on Voigt deconvolution
E_0	threshold energy of the X-ray absorption process
$f_{2\theta}$	intrinsic XRD profile function
$F_j(k)$	the magnitude of the backscattering amplitude of the j th neighbor
$g_{2\theta}$	instrumental XRD profile function
$h_{2\theta}$	experimental XRD profile function
k	the photoelectron wavenumber
N_j	number of atoms in the j_{th} shell
R_j	mean distance between absorber and the j_{th} shell
S	surface area
S_0^2	amplitude reduction factor
ϕ	shape parameter of <i>Voigt</i> profile
σ	<i>Debye-Waller</i> factor

8.2 Publication Index

1. „Enzymatic Resolution Coupled with Substrate Racemization using a Thioester Substrate“, D.S. Tan, M.M. Günter, and D.G. Drueckhammer, J. Am. Chem. Soc. **1995**, 117, 9093.
2. „An X-Ray Diffraction Study on the Kinetics of the Cation Redistribution in the Spinel $NiAl_2O_4$ “, R. Röttger, H. Schmalzried, and M. Günter, Ber. Bunsenges. Phys. Chem. **1997**, 101(8), 1083.
3. „Microstructure and Bulk Reactivity of the Nonevaporable Getter $Zr_{57}V_{36}Fe_7$ “, M.M. Günter, D. Herein, R. Schumacher, G. Weinberg, and R. Schlögl, J. Vac. Sci. Technol. A, **1998**, 16(6), 352.
4. „In situ X-ray absorption and diffraction studies on the formation of molybdenum suboxides during reduction of MoO_3 “, T. Ressler, R.E. Jentoft, J. Wienold, M.M. Günter, and O. Timpe, Journal of Physical Chemistry, **2000**, 104, 6360.
5. „Implication of the microstructure of binary Cu/ZnO catalysts for their catalytic activity in methanol synthesis“, M.M. Günter, T. Ressler, B. Bems, C. Büscher, T. Genger, O. Hinrichsen, M. Muhler, and R. Schlögl, Cat. Lett., **2001**, 71, 37.
6. „In situ studies on the structure of copper oxide/zinc oxide catalysts“, M.M. Günter, T. Ressler, B. Bems, R. Schlögl, and T. Ressler, J. Synchrotron Rad. **2001**, 8, 619.
7. „Redox behavior of CuO/ZnO catalysts in the steam reforming of methanol studied by X-ray diffraction and absorption“, M.M. Günter, T. Ressler, R.E. Jentoft, and B. Bems, J. Catal., *accepted*.
8. „Kinetics of solid-state reaction in heterogeneous catalysis from time-resolved X-ray absorption spectroscopy“, T. Ressler, J. Wienold, J. R.E. Jentoft, and M.M. Günter, Top. in Catalysis, *accepted*.

8.3 Curriculum Vitae

Name: Marco Maria Günter

Date of birth: 8th December 1969

Place of birth: Hildesheim

Nationality: German

Education:

1976 – 80 Grundschule Sarstedt

1980 – 82 St. Augustinus-Schule, Hildesheim

1982 – 89 Gymnasium Josephinum, Hildesheim

05/89 Abitur

Military Service:

06/89 – 08/90 Panzergrenadierbrigade, Hildesheim

University:

10/90 – 08/96 Study at the Universität Hannover

09/92 Intermediate exam

09/93 – 05/94 Study as a scholarship holder of the DAAD at the Stanford University, California, USA; group of Prof. D. Drueckhammer

02/96 – 08/96 Diploma thesis at Institut für Physikalische Chemie und Elektrochemie der Universität Hannover, Prof. Dr. H. Schmalzried; Title:
„Röntgenographische Untersuchungen zur Kationenumlagerung in $NiAl_2O_4$ “.

Graduate School:

since 04/97 PhD thesis in ‘Abteilung Anorganische Chemie des Fritz-Haber-Instituts der Max-Planck-Gesellschaft’, Prof. Dr. R. Schlögl, with the topic
„Structure and Activity of Copper/Zinc Oxide Catalysts studied using X-ray diffraction and Absorption spectroscopy”.